Spatial adiabatic passage:
light, sound and matter waves

Ricard Menchon Enrich

Doctorat en Física

Directors:
Dr. Jordi Mompart Penina
Dra. Verònica Ahufinger Breto

Universitat Autònoma de Barcelona

Departament de Física
Universitat Autònoma de Barcelona
Bellaterra, 2013

Contents

Introduction

At the beginning of the twentieth century several previously experimentally reported phenomena, such as the black body radiation [1], the photoelectric effect [2, 3] or the spectral lines of atomic gases [4, 5, 6], were successfully accounted for by considering that the energy radiated from atomic systems was in the form of discrete elements or *quanta* [7, 8] and by the study of the internal structure of the atom which led to the assumption of the Bohr s model [9, 10, 11, 12, 13, 14, 15]. These facts constituted the birth of Quantum Mechanics. Although some phenomenological theories were initially proposed, known as Old Quantum Mechanics [11, 12, 13, 14, 16, 17], it was not until the mid-1920s that the standard formulation of Quantum Mechanics was developed and finally established around the 1930s, with the unification [18] of several formulations such as matrix mechanics [19, 20] and wave mechanics [21], and the inclusion of the uncertainty principle [22]. Since then, Quantum Mechanics has allowed for a better understanding of fundamental aspects related to the wave-particle duality [17, 23] and the interaction between radiation and matter. Furthermore, Quantum Mechanics has been the origin of other disciplines such as Quantum Chemistry [24], Quantum Optics [25] or Quantum Information science [26]. The development of the latter two was closely related to the invention of the laser [27, 28, 29], since it provided a more accurate way to study the light-matter interaction and allowed for what is known as *Quantum engineering*. Thus, laser light can be used, for example, for spectroscopy [30], generation of nonlinear phenomena [31], for trapping and cooling of particles [32] and for the measurement and manipulation of individual particle states [33].

Many of the processes in Quantum Mechanics and, in particular in *Quantum engineering*, are purely oscillatory, i.e., are based on the wave-like behavior of the atomic probability amplitude and its associated phase. For this reason, quantum oscillatory processes can be extended to other non- quantum physical systems which also support oscillating quantities. This is the case of the so-called adiabatic passage processes, which in Quantum Mechanics allow for a robust and efficient control of the atomic

population transfer between two states of the system [34, 35]. Adiabatic passage processes are a particular case of adiabatic following, a concept arising from the adiabatic theorem [36]. As for any adiabatic following, one of the main characteristics of the adiabatic passage processes is their robustness, i.e., if the process is performed adiabatically the transfer will be efficient regardless which are the selected specific parameter used to drive the system and their fluctuations. This constitutes the main advantage of this kind of process with respect to other transfer processes, in which the transfer may depend on a specific combination of parameter values of the system, specially when high fidelities are required. For example, in quantum computation, it is believed that error thresholds between 10^{-4} and 10^{-2} in the fidelity of the implementation of the quantum logic gates are required for fault-tolerant computation [37]. Thus, adiabatic passage processes to control the internal and external degrees of freedom of single cold atoms have been suggested for the implementation of quantum logic gates due to their high robustness and fidelity [37, 38, 39, 40, 41, 42].

In this thesis, adiabatic passage processes are addressed in different oscillatory physical systems, both quantum and classical. As a common feature, all the approaches present robustness and high fidelity in the transfer of the oscillating quantity, which is exploited in order to either provide new applications or to improve the existing ones in the corresponding field of physics. In particular, we apply adiabatic passage processes to control (i) light propagation in a system of three coupled optical waveguides, (ii) sound propagation along a system of two coupled linear defects in a sonic crystal, (iii) propagation of single cold atoms in systems of three coupled atomic waveguides and (iv) transfer of single cold atoms in two-dimensional harmonic triple-well potential systems.

Since the central topic of this thesis is the spatial adiabatic passage process, Chapter 1 is devoted to explain the basics of adiabatic following of an eigenstate or supermode. In order to link all the different implementations of the adiabatic passage discussed along the thesis, we will pay special attention in highlighting the key elements that a physical system must have to perform it.

In Chapter 2 we present the spatial adiabatic passage of light in a system of three evanescent-coupled silicon oxide total internal reflection waveguide system, which consists in a complete transfer of light intensity between the outermost waveguides of the system. The advantage of spatial the adiabatic passage of light compared to the traditional directional couplers is that the transfer is robust in front of technological variations and does not depend on precisely selected parameter values. The spatial adiabatic passage of light was already presented as a proof of principle in [43, 44]. However, here we show the first experimental implementation of the passage in CMOS-compatible technology, which represents an important technological improvement since it allows for a massive and low-cost fabrication of these devices and their incorporation to realistic photonic integrated circuits. Additionally, using the same technology, we experimentally demonstrate the use of the system as a high- and low-pass spectral filter based on the spatial adiabatic passage in a triple-waveguide system. Due to its robustness against technological variations and its low cost this spatial adiabatic passage spectral

filter represents an alternative to interference-based and absorbance-based filters.

In Chapter 3, spatial adiabatic passage processes are applied to sound waves for the first time to the best of our knowledge. An interesting candidate for guiding sound waves are linear defects in sonic crystals [45, 46], which allow for measurements inside the crystal. In addition, sonic crystals offer a straightforward analogy with photonic crystals [47, 48, 49]. By modifying the geometry of the linear defects along the propagation distance and studying the projected band diagrams obtained using the plain wave expansion method, spatial adiabatic passage processes for sound waves are proposed leading to the implementation of a coherent multifrequency adiabatic splitter, a phase difference analyzer and a coherent multifrequency adiabatic coupler.

Chapter 4 proposes to use spatial adiabatic passage processes to inject into, extract from and velocity filter neutral atoms in a dipolar ring trap by using two additional waveguides. The described mechanisms are based on the adiabatic following of a transversal dark state and resemble the spatial adiabatic passage of matter waves in potential wells [50, 51, 52, 53, 54, 55]. A semi-analytical condition for the threshold longitudinal velocity allowing for an efficient spatial adiabatic passage is obtained which perfectly matches the results of the numerical integration of the full two-dimensional Schrodinger equation. Furthermore, it has been numerically checked that the proposal can be realized using state-of-the-art parameter values for ultracold atoms in optical dipole traps.

In the next two chapters, 5 and 6, we study the spatial adiabatic passage of a single cold atom in two-dimensional triple-well potentials, going beyond the well understood effectively one-dimensional systems [50, 51, 52, 53, 54, 55] and studying the possibilities arising from the additional degrees of freedom. On the one hand, in Chapter 5, a system of three coupled identical harmonic potentials with the traps lying in a triangular configuration is used for interferometry taking profit of a level crossing appearing in the energy spectrum. On the other hand, in Chapter 6, angular momentum is successfully generated by breaking the symmetry of a spatial adiabatic passage sequence in a system of three harmonic traps of different trapping frequencies by simultaneously following two eigenstates of the system.

Finally, Chapter 7 presents the conclusions of this thesis and a discussion on future perspectives.

1

Adiabatic passage processes

Adiabatic passage processes have been successfully applied in different fields of physics, such as Quantum Optics, Atomic Physics or waveguide Optics, to coherently control, for example, the evolution of atomic population and the propagation of light, sound or matter waves, and are at the basis of the research work presented in this thesis. Thus the main aim of this first chapter is to introduce the concept of adiabatic passage. We will start with the most general meaning of adiabatic following of an eigenvector and we will continue with a brief review of spatial adiabatic passage and its implementation in different physical systems, specially focusing on the key elements necessary to perform the passage with high efficiency and robustness.

1.1 Adiabatic following of an eigenvector

As early as 1928, Max Born and Vladimir Fock stated the adiabatic theorem [56], which introduced the concept of adiabatic following:

A physical system remains in its instantaneous eigenstate if a given perturbation is acting on it slowly enough and if there is a gap between the eigenvalue and the rest of the Hamiltonian's spectrum.

Let us illustrate the adiabatic theorem with a simple example. Consider a single atom initially resting in the ground vibrational state of a one-dimensional harmonic potential trap of frequency , as shown in the left panel of Fig. 1.1. In the harmonic trap, the atom can only occupy states with discrete energy values given by $E_n =$ $(n+1\ \ 2)$, with $n = 0\ \ 1\ \ 2\ \ 3$ Our goal is to move the atom from its initial position, x_i, to a final position, x_f. With this aim we will move the trap between these two positions. If we move the trap very fast, the wavefunction cannot adapt to the change and will remain in its initial position x_i while the trap has been displaced some distance, see Fig. 1.1(a). In this case, the wavefunction does not longer correspond to the ground state of the trap, but to a combination of several of the states of the harmonic potential

and will start oscillating inside the trap. However, if the trap is slowly moved, the wavefunction can continuously readjust its shape and phase to the moving harmonic potential, i.e., it will follow the instantaneous ground eigenstate of the harmonic trap during the process and, therefore, any other higher n vibrational eigenstate will be excited, see Fig. 1.1(b). This second case is an example of adiabatic following.

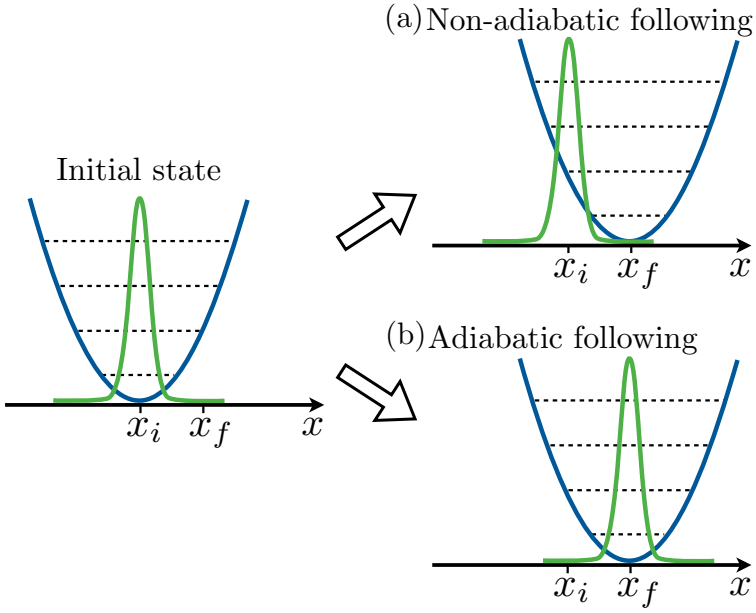

Figure 1.1: Schematic representation of an example of the final state of a non-adiabatic following process (a) and an adiabatic one (b). At the left side, the initial state of both processes, corresponding to an atom in the ground vibrational state of a one-dimensional harmonic trap, is depicted.

The adiabatic following of an eigenvector is not an exclusive process of Quantum Mechanics. For example, it can also be applied to light propagation in waveguides. Propagating light can adiabatically follow a mode (eigenvector) of a waveguide if the modification of the mode profile is smooth along the propagation direction. In general, to perform an adiabatic following it is necessary to have a physical system which allows for discrete eigenvalues and eigenvectors that can be modified along its temporal or spatial evolution. If we call s the variable along which the eigenvector is modified, the eigenvalues and eigenvectors must be continuous functions of s. Additionally, the eigenvalues cannot cross each other along s and the first and second derivates of the eigenvectors have to be well defined with respect to s [36]. Any physical system fulfilling these characteristics is a good candidate to perform an adiabatic following of one of its eigenvectors. However, it is still necessary a smooth variation of the eigenvector in s in order for the system to follow it adiabatically. How smooth the modification

of this eigenvector has to be can be obtained from the probability to excite any other eigenvector of the system during the process. If the eigenvector that we want to follow is $\Psi_i(s)$, the probability $p_{i\ \ j}$ to excite any other state $\Psi_j(s)$ during the process fulfills [36]:

$$p_{i\ \ j} \lesssim \max \left| \left(\Psi_j(s) \frac{d\,\Psi_i(s)}{ds} \right) \ \ _{ij}(s) \right|^2 \tag{1.1}$$

where $_{ij}(s) = \ _j(s) - \ _i(s)$, with $_i(s)$ ($_j(s)$) being the oscillation frequency of the $\Psi_i(s)$ ($\Psi_j(s)$) eigenvector, which gives the corresponding eigenvalue. Thus, for a certain modification in the physical system with respect to s, if we want to follow adiabatically the $\Psi_i(s)$ eigenvector not exciting any other eigenvector $\Psi_j(s)$, the value of $p_{i\ \ j}$ has to be as small as possible for any $j = i$.

1.2 Adiabatic passage processes

Adiabatic passage processes are a particular example of adiabatic following which imply a transfer of an oscillating quantity, as for example, the quantum probability amplitude or an electromagnetic field, among different individual elements of a physical system that can support the oscillations, such as atomic states or modes of waveguides.

There are three basic conditions required to perform an adiabatic passage process. The first one is the existence of these different individual elements supporting the oscillating quantity. Each of these elements supports its own oscillation, and we will call them asymptotic eigenvectors. The second item is a coupling mechanism between the asymptotic eigenvectors. And finally, the third one is the possibility to control the strength of the couplings and/or the oscillation frequency of the asymptotic eigenvectors along the process. In a physical system where these three conditions are fulfilled, it is possible to perform an adiabatic passage process by following an eigenvector of the full system, which will consist of a superposition of the coupled asymptotic eigenvectors.

The evolution in s of the oscillating quantity, considering s as the variable that measures the evolution of the process, can be studied by means of coupled linear equations. In a system of N asymptotic eigenvectors $_k$ with $k = 1\ 2\ \cdots\ N$, where each asymptotic eigenvector is equal to

$$_k = \begin{pmatrix} 0 \\ \vdots \\ 0 \\ 1 \\ 0 \\ \vdots \\ 0 \end{pmatrix} \begin{matrix} 1 \\ \vdots \\ k-1 \\ k \\ k+1 \\ \vdots \\ N \end{matrix} \tag{1.2}$$

the coupled equations for the evolution of the process can be written in a matrix form

in the asymptotic eigenvectors basis as

$$i\frac{d}{ds}\begin{pmatrix} a_1 \\ a_2 \\ \vdots \\ a_N \end{pmatrix} = \frac{1}{2}\begin{pmatrix} 2\ _1 & -\Omega_{2,1} & -\Omega_{3,1} & \cdots & -\Omega_{N,1} \\ -\Omega_{1,2} & 2\ _2 & -\Omega_{3,2} & \cdots & -\Omega_{N,2} \\ -\Omega_{1,3} & -\Omega_{2,3} & 2\ _3 & \cdots & -\Omega_{N,3} \\ \vdots & \vdots & \vdots & \ddots & \vdots \\ -\Omega_{1,N} & -\Omega_{2,N} & -\Omega_{3,N} & \cdots & 2\ _N \end{pmatrix}\begin{pmatrix} a_1 \\ a_2 \\ \vdots \\ a_N \end{pmatrix} \tag{1.3}$$

Here, a_k and $\ _k$ are the complex amplitude and the oscillation frequency of the k-th asymptotic eigenvector $\ k\ $, respectively, and $\Omega_{k,l}$ with $k = l$ is the coupling rate from the k-th to the l-th asymptotic eigenvector.

The available eigenvectors of the full system $\ \Psi_i(s)\ $ and the corresponding oscillation frequencies associated to the eigenvalues $\ _i$, with $i = 1\ 2\ \cdots\ N$, can be obtained by diagonalizing the matrix in Eq. (1.3). The obtained eigenvectors of the full system consist in a superposition of the different asymptotic eigenvectors. For example, the i-th eigenvector could be represented as

$$\Psi_i(s)\ = \begin{pmatrix} a_{i,1} \\ a_{i,2} \\ \vdots \\ a_{i,N} \end{pmatrix} \tag{1.4}$$

where $a_{i,k}$ are the amplitudes of the asymptotic eigenvectors $\ k\ $. In most of the works related with adiabatic passage processes, the matrix in Eq. (1.3) is written with $2\ _1$ subtracted in the diagonal, i.e.,

$$i\frac{d}{ds}\begin{pmatrix} a_1 \\ a_2 \\ \vdots \\ a_N \end{pmatrix} = \frac{1}{2}\begin{pmatrix} 0 & -\Omega_{2,1} & -\Omega_{3,1} & \cdots & -\Omega_{N,1} \\ -\Omega_{1,2} & 2\Delta_2 & -\Omega_{3,2} & \cdots & -\Omega_{N,2} \\ -\Omega_{1,3} & -\Omega_{2,3} & 2\Delta_3 & \cdots & -\Omega_{N,3} \\ \vdots & \vdots & \vdots & \ddots & \vdots \\ -\Omega_{1,N} & -\Omega_{2,N} & -\Omega_{3,N} & \cdots & 2\Delta_N \end{pmatrix}\begin{pmatrix} a_1 \\ a_2 \\ \vdots \\ a_N \end{pmatrix} \tag{1.5}$$

where $\Delta_k = \ _k - \ _1$. This usually allows for an easier diagonalization of the matrix, obtaining the same eigenvectors as with Eq. (1.3) with only a constant common shift in all the eigenvalues. Also, in most of the works, the matrices in Eq. (1.3) and (1.5) are symmetric, i.e., $\Omega_{k,l} = \Omega_{l,k}$, which significantly simplifies the diagonalization problem.

By controlling both the strength of the couplings and the oscillation frequency of the asymptotic eigenvectors, it is possible to modify the values of the amplitudes $a_{i,k}$ of a certain eigenvector $\ \Psi_i(s)\ $. In this way, it is possible to initially excite an eigenvector $\ \Psi_i(s = 0)\ $ involving only certain individual elements of the physical system with asymptotic amplitudes $a_{i,k}$ and, by adiabatically following the eigenvector $\ \Psi_i(s)\ $, which is modified along with the evolution of s, end up with a final eigenvector $\ \Psi_i(s = S)\ $ involving other individual elements with different asymptotic eigenvector

amplitudes. This adiabatic change of the asymptotic eigenvectors amplitudes constitutes an adiabatic passage process. The adiabaticity condition in Eq. (1.1) is also valid for the adiabatic passage. Additionally, once the eigenvalues of the process are calculated, Eq. (1.1) gives information on the limitations for the variation of the couplings and the oscillation frequencies to perform an efficient adiabatic passage process. It is important to remember that there cannot be any crossing of the eigenvalues of the full system during the process in order to perform the adiabatic following.

The advantage of adiabatic passage processes with respect to other transfer techniques relays on their robustness: as long as the process is performed adiabatically and the desired eigenvector is followed, the transfer between the asymptotic eigenvectors will be almost 100% efficient no matter the particular parameter values chosen for the variation of the couplings, the variation of the oscillation frequency of the asymptotic eigenvectors or the total time of the process or length of the system.

1.3 Examples of adiabatic passage processes

In this section we will briefly review some of the implementations of the adiabatic passage processes. In particular, we will focus on the processes that have been used to control the population transfer in systems of internal atomic levels and the population transport in atomic traps. At the end of the section we will also introduce the propagation dependent adiabatic processes that will be fully described in the next chapters of this thesis, such as the control of (i) light propagation in coupled optical waveguide systems in Chapter 2, (ii) sound propagation in systems of coupled linear defects in sonic crystals in Chapter 3 and (iii) atomic propagation in systems of coupled dipolar waveguides in Chapter 4. Another interesting example of adiabatic passage process is shown in [57], where it has been applied to classical mechanical systems in order to control the oscillation of coupled springs or pendulums. Furthermore, although adiabatic passage processes have been mainly used to control the transfer of atomic population or light intensity, they have also been proposed for other applications, as for example for spectral filtering, as we will shown in Chapter 2, for splitting and phase analysis of sound waves, as we will present in Chapter 3, or for interferometry or angular momentum generation with single atoms, as it will be shown in Chapters 5 and 6.

1.3.1 Time-dependent adiabatic passage with atomic internal degrees of freedom

Two techniques can be highlighted in order to control the population transfer in systems of internal atomic levels, the so-called stimulated Raman adiabatic passage (STIRAP) [34, 58, 59] and the rapid adiabatic passage (RAP)[59, 35] techniques.

The STIRAP technique is performed in Λ-type three-level atomic systems interacting with two laser pulses in order to completely transfer the population between the two ground states of the system. On the other hand, the RAP technique is im-

plemented in two-level atomic systems interacting with a chirped laser pulse in order to completely transfer the population between the two states. In the last decades, these two techniques have been used for several applications [59], being the STIRAP technique specially successful. For example, experimentally implemented applications based on STIRAP processes have been developed as a way to control chemical reactions [60], for coherent transfer of momentum [61], for laser cooling [62], or to create coherent superpositions of photon-number states by strongly coupling an atom to a cavity field [63]. Moreover, spatial dependent STIRAP has been proposed to achieve sub-wavelegth localization via adiabatic passage, which, in turn, has been applied for nanolithography and patterning of Bose-Einstein condensates [64], single-site addressing in optical lattices [65], or nanoscale resolution in fluorescence microscopy [66]. Some proposals based on the RAP technique have been also reported, as for example its use for doppler-free adiabatic self induced transparency [67].

In atomic systems with two or three internal atomic states, the evolution variable corresponds to the time, t, the oscillating quantity is the quantum probability amplitude, the asymptotic eigenvectors are the states of the atomic levels, and the coupling between them is given by the interaction with the light pulses. The way to control the strength of the couplings is through the intensity of the laser pulses while the control of the oscillation frequency of the asymptotic states is through the detuning of the laser pulses, i.e., the difference between the laser light frequency and the transition frequency between two atomic states.

Stimulated Raman adiabatic passage (STIRAP)

For the usual implementation of STIRAP [34], the Schrodinger equation describing the coupling of the three states forming the Λ-type system with the two laser pulses, in the interaction picture and within the rotating wave approximation (RWA) [68], can be written similarly to Eq. (1.5). Considering the Λ-type system, see Fig. 1.2, with two ground states 1 and 3 and an intermediate excited state 2, a pump pulse with frequency $_P$ that couples states 1 and 2, and a Stokes pulse with frequency $_S$ that couples states 2 and 3, the Schrodinger equation reads:

$$i \frac{d}{dt} \begin{pmatrix} a_1 \\ a_2 \\ a_3 \end{pmatrix} = \frac{}{2} \begin{pmatrix} 0 & -\Omega_P(t) & 0 \\ -\Omega_P(t) & 2\Delta_p & -\Omega_S(t) \\ 0 & -\Omega_S(t) & 2(\Delta_P - \Delta_S) \end{pmatrix} \begin{pmatrix} a_1 \\ a_2 \\ a_3 \end{pmatrix} \tag{1.6}$$

Here, a_k are the amplitudes corresponding to states k, with $k = 1\ 2\ 3$, $\Omega_P(t)$ and $\Omega_S(t)$ are the Rabi frequencies of the atom-laser interaction for the pump and the Stokes fields, respectively ($\Omega = \boldsymbol{\mu} \cdot \mathbf{E}$ where $\boldsymbol{\mu}$ is the electric dipole moment and $\mathbf{E}$ is the electric field). Without loss of generality we will assume that Ω_P and Ω_S are real-valued and positive [59]. The diagonal elements of the Hamiltonian matrix in Eq. (1.6) are the three RWA energies: the zero element is the energy of state 1 lifted (dressed) by the photon energy $_P$ and used as the reference energy level, $\Delta_P = (E_2 - E_1) - _P$

and $\Delta_S = (E_2 - E_3) \quad - \quad _S$ are the frequency offsets (detunings) of states 2 and 3 , respectively, where E_k is the energy of state k (with $k = 1\ 2\ 3$) in the absence of coupling with the fields. Although both Δ_P and Δ_S can be different from zero, the two-photon resonance condition $\Delta_P = \Delta_S$ is essential to perform the STIRAP process, as it will be seen below.

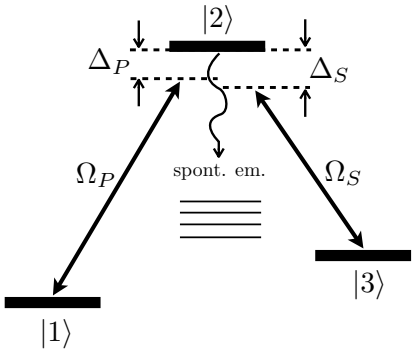

Figure 1.2: Λ-type system consisting of two ground states 1 and 3 coupled via an excited state 2 through the interaction with two laser pulses, the Stokes and the pump, with Rabi frequencies Ω_S and Ω_P, respectively. The detuning of the Stokes and pump laser frequencies from the transition frequency to the excited state 2 are Δ_S and Δ_P, respectively. The excited state 2 may decay by spontaneous emission to other states.

Diagonalizing the Hamiltonian in Eq. (1.6) under the two photon resonance condition, it is possible to find the energy eigenvalues and the eigenstates of the dressed Λ-type system in interaction with the laser pulses. The oscillation frequencies of the dressed-eigenstates, which are 1 times the energy eigenvalues, read:

$$_1 = \frac{1}{2}\left(\Delta_P - \sqrt{\Delta_P^2 + \Omega_P^2 + \Omega_S^2}\right) \tag{1.7}$$

$$_{\text{dark}} = 0 \tag{1.8}$$

$$_3 = \frac{1}{2}\left(\Delta_P + \sqrt{\Delta_P^2 + \Omega_P^2 + \Omega_S^2}\right) \tag{1.9}$$

while the corresponding dressed-eigenstates can be expressed as:

$$\Psi_1 \ = \sin\theta \sin\theta \ 1 \ + \cos\theta \ 2 \ + \cos\theta \sin\theta \ 3 \tag{1.10}$$

$$\Psi_{\text{dark}} \ = \cos\theta \ 1 \ - \sin\theta \ 3 \tag{1.11}$$

$$\Psi_3 \ = \sin\theta \cos\theta \ 1 \ - \sin\theta \ 2 \ + \cos\theta \cos\theta \ 3 \tag{1.12}$$

where the mixing angles θ and θ are defined as:

$$\tan\theta = \frac{\Omega_P}{\Omega_S} \tag{1.13}$$

$$\tan\theta = \frac{\sqrt{\Omega_P^2 + \Omega_S^2}}{\sqrt{\Omega_P^2 + \Omega_S^2 + \Delta_P^2} + \Delta_P} \tag{1.14}$$

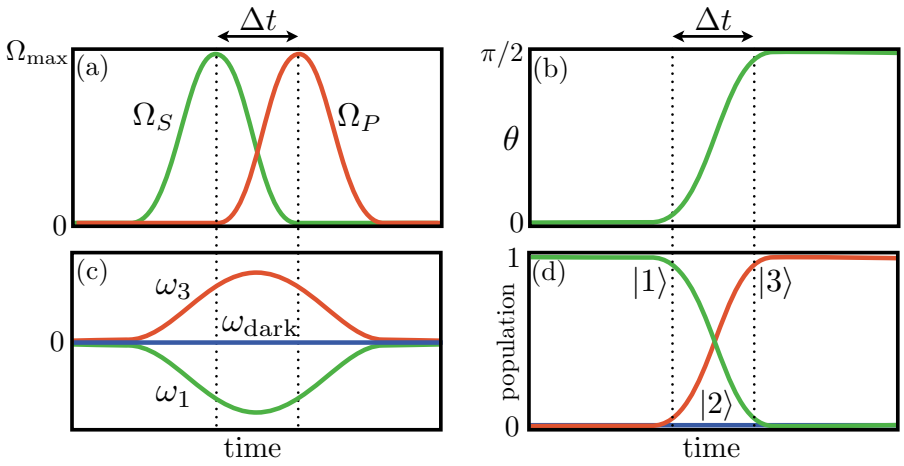

Figure 1.3: An example of the time evolution of (a) the Rabi frequencies of the pump and Stokes laser pulses, (b) the mixing angle θ, (c) the dressed-state eigenvalues, and (d) the population in states 1 (starting at unity), 3 (reaching unity) and 2 remaining equal to zero during the whole process, for a STIRAP process with $\Delta_P = \Delta_S = 0$.

The STIRAP process consists in the adiabatic following of the eigenstate Ψ_{dark}, the so-called dark state, which does not involve state 2. From Eq. (1.11) it is straightforward to see that Ψ_{dark} can be modified by changing the mixing angle θ, which in turn, depends on the coupling strengths. The goal of the STIRAP process is to transfer the atom between the ground states, for example from state 1 to state 3. Intuitively, one would think that the best way to do this is by coupling first state 1 to state 2 and then couple state 2 to state 3. However, in the STIRAP technique, states 2 and 3 are coupled first, and then, with a certain temporal delay, state 1 and state 2 are coupled. Thus, this temporal coupling sequence is usually called counterintuitive coupling sequence. Considering initially the atom in state 1, the coupling Ω_S is set strong by increasing the intensity of the Stokes pulse while the pump is off, i.e., $\Omega_P = 0$. In this way, $\theta = 0$ and the eigenstate $\Psi_{\text{dark}}(t = 0) = 1$. Then, if the intensity of the pump pulse increases and the one of the Stokes pulse starts decreasing, we reach the opposite situation where Ω_P is strong while $\Omega_S = 0$. In this case, $\theta = \omega$ 2 and

the eigenstate $\Psi_{\rm dark}(t=T) = -3$, where T is the total time of the process. If the eigenstate $\Psi_{\rm dark}$ is followed adiabatically by smoothly applying the pulse sequence previously described, the atom will be efficiently transferred from state 1 to 3. This corresponds to the STIRAP process. Note that during the process the excited state 2, which could introduce losses due to spontaneous emission is not populated at any time. In Fig. 1.3 it is shown an example of the evolution in time of the couplings, the θ mixing angle, the energy eigenvalues and the population in the atomic states for $\Delta_P = \Delta_S = 0$. In the figure we can see that the there is no crossing of the energy eigenvalues during the process.

In [34], a specific condition for the adiabaticity of the process has been derived from the more general one shown in Eq. (1.1) together with numerical studies. In particular, considering that (i) $\Delta_P = \Delta_S = 0$, (ii) the strength of the couplings follows a Gaussian profile along the process, and (iii) the maxima of these Gaussians, $\Omega_{P,\max}$ and $\Omega_{S,\max}$, are separated in time $\Delta t = \bar{2}\nu$, where ν is the the standard deviation of the Gaussian temporal profiles of the laser pulses, the adiabaticity condition is given by

$$\Delta t\sqrt{\Omega_{P,\max}^2 + \Omega_{S,\max}^2} > 10 \tag{1.15}$$

Rapid adiabatic passage (RAP)

Regarding the RAP technique, the Schrodinger equation that describes the time evolution of the probability amplitude in the system of two atomic states coupled through a chirped laser pulse is also of the form of Eq. (1.5). Considering the two states as 1, the ground state, and 2, the excited state, interacting with a laser pulse that couples them and has a frequency $_L(t)$ that can be varied in time (see Fig. 1.4), in the interaction picture and within the RWA [68], the Schrodinger equation can be written as

$$i\ \frac{d}{dt}\begin{pmatrix} a_1 \\ a_2 \end{pmatrix} = \frac{}{2}\begin{pmatrix} 0 & -\Omega(t) \\ -\Omega(t) & 2\Delta(t) \end{pmatrix}\begin{pmatrix} a_1 \\ a_2 \end{pmatrix} \tag{1.16}$$

Here, a_k are the amplitudes corresponding to states k, with $k = 1\ 2$, $\Omega(t)$ is the Rabi frequency of the atom-laser interaction. As in the case of STIRAP, we will assume that Ω is real-valued and positive [59]. The diagonal elements of the Hamiltonian matrix are the RWA energies, with the zero element being the energy of state 1 dressed by the photon of energy $_L$ and used as the reference energy level, while $\Delta(t) = (E_2 - E_1) - {}_L(t)$ is the detuning with respect to state 2, where E_1 and E_2 are the energies of the states 1 and 2 in absence of the laser interaction, respectively.

If the Hamiltonian in Eq. (1.16) is diagonalized, the energy eigenvalues and eigenstates are obtained. The oscillation frequencies of the eigenstates read:

$$_{\pm} = \frac{1}{2}\left(\Delta \mp \sqrt{\Omega^2 + \Delta^2}\right) \tag{1.17}$$

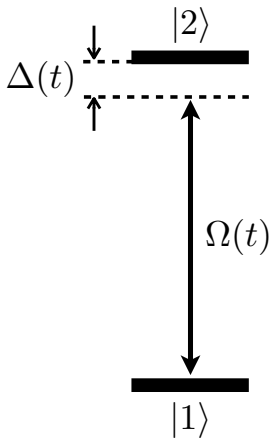

Figure 1.4: System consisting of two internal atomic states 1 and 2 interacting with a laser pulse with temporal variation of its frequency and intensity.

The corresponding energy eigenstates of the system are given by:

$$\Psi_+ = \cos\theta\ 1 + \sin\theta\ 2 \tag{1.18}$$

$$\Psi_- = \sin\theta\ 1 - \cos\theta\ 2 \tag{1.19}$$

and the corresponding mixing angle θ is defined as:

$$\tan 2\theta = \frac{\Omega}{\Delta} \tag{1.20}$$

The RAP process consists of adiabatically following either Ψ_+ or Ψ_- to achieve a complete transfer of the atomic population from the ground state 1 to the excited 2 state. From Eqs. (1.18) and (1.19) it is clear that both eigenstates can be modified by changing the mixing angle θ, which depends on the ratio Ω Δ (see Eq. (1.20)):

- if $\Omega \ll \Delta$ and $\Delta > 0$, the mixing angle is $\theta = 0$ and the eigenstates are $\Psi_+ = 1$ and $\Psi_- = -2$
- if $\Omega \ll \Delta$ and $\Delta < 0$, the mixing angle is $\theta = \omega\ 2$ and the eigenstates are $\Psi_+ = 2$ and $\Psi_- = 1$.
- if $\Omega \langle \Delta$, the mixing angle value is $\theta = \omega\ 4$ and the eigenstates are $\Psi_+ = (1 + 2)\ \overline{2}$ and $\Psi_- = (1 - 2)\ \overline{2}$.

In this way, since the objective is to transfer the atom from 1 to 2 , we can modify θ either from 0 to ω 2 and follow Ψ_+ , or from ω 2 to 0 and follow Ψ_- . This implies that the process has to start with the laser far from resonance but with low enough

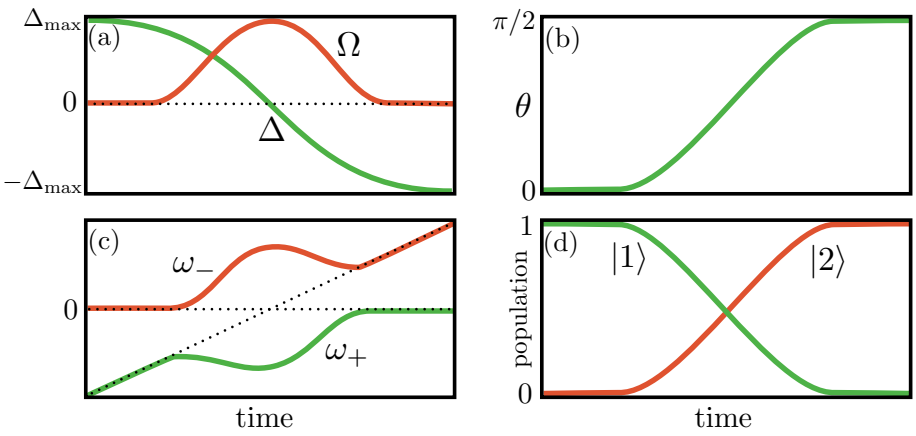

Figure 1.5: Example of the time evolution of (a) the Rabi frequency Ω and the detuning Δ, (b) the mixing angle θ, (c) the dressed-state eigenvalues, and (d) the population in states 1 (starting at unity) and 2 (reaching unity) for a RAP process.

intensity to fulfill $\Omega \ll \Delta$, with $\Delta > 0$ if we want to follow Ψ_+ or with $\Delta < 0$ if we want to follow Ψ_-. Then, the absolute value of the detuning has to smoothly decrease while the laser intensity (and thus, the coupling) increases, reaching eventually $\Omega \langle \Delta$ and $\theta = \omega 4$. At this point, the sign of the detuning has to change and increase its absolute value while the coupling strength decreases until $\Omega \ll \Delta$ is fulfilled again but with the opposite sign of Δ compared to that at the beginning of the process. If the modification of the followed eigenstate, Ψ_+ or Ψ_-, has been smooth enough during the process, the atom will be able to follow it adiabatically and it will be transferred from 1 to 2, which constitutes the RAP process. An example of a RAP process is shown in Fig. 1.5, where the eigenstate Ψ_+ is adiabatically followed. Additionally, Fig. 1.5 shows that there is no crossing of the energy eigenvalues during the process, which allows for the adiabatic following of one of the eigenstates of the system (Ψ_+ in the figure).

A specific condition can be found from Eq. (1.1) on how to modify the coupling and the detuning in order that the atom can follow the selected eigenstate [59, 35]. The condition reads

$$\frac{1}{2}\left|\Omega\dot{\Delta} - \dot{\Omega}\Delta\right| \ll \left(\Omega^2 + \Delta^2\right)^{3/2} \tag{1.21}$$

where the dot denotes time derivative.

Note also that if the θ angle is modified from either 0 or $\omega 2$ to $\omega 4$, the final state would correspond to a splitting of the atom between the 1 and 2 states, i.e., a superposition $\Psi_+ = (1 + 2) \overline{2}$ or $\Psi_- = (1 - 2) \overline{2}$ depending on the followed eigenstate of the system.

1.3.2 Time-dependent adiabatic passage with external degrees of freedom

After the successful implementation of adiabatic passage techniques for systems of internal atomic levels, adiabatic passage processes were extended to external degrees of freedom in the field of Ultracold Atoms. The first work appeared in 2004 [50], where adiabatic passage processes were proposed to coherently control the transport of a single cold atom between the most distant wells of a system of three tunneling-coupled potential wells. Subsequently, other works also proposed adiabatic passage processes for transport of single cold atoms [52, 54, 69] as well as for other kind of particles, such as electrons [70], vortices [71] or holes [55], and also Bose Einstein condensates (BECs) [72, 73, 74, 75, 53, 76]. All these adiabatic passage processes implying transport in space have been named spatial adiabatic passage processes. These systems of single particles or BECs also present the required elements to perform adiabatic passage processes that we have discussed in Section 1.2. Specifically, the evolution variable s is the time t, the oscillating quantity corresponds to the quantum probability amplitude, the asymptotic eigenvectors are the asymptotic energy vibrational eigenstates of the individual potential wells, and the coupling between the asymptotic states is given by the tunneling effect which can be modified with the separation between traps. For the case of single particles, the control of the oscillation frequency of the asymptotic eigenstates is obtained by modifying the characteristics of the potential trap in order to shift the energy of the asymptotic states, which is proportional to the oscillation frequency. For BECs, apart from the energy of the asymptotic states given by the trap, it has to be taken into account that the nonlinear interaction also changes the oscillation frequency of the asymptotic eigenstate that is populated.

In these systems, only the three asymptotic eigenstates of similar energy, one per potential well, play a role in the adiabatic population evolution. We will call these asymptotic states as L for the left trap, C for the central trap and R for the right trap. Other asymptotic eigenstates of the wells are assumed to have significant different values of energy and therefore uncoupled from the three considered ones. In this case, the equation describing the evolution of the probability amplitudes of being in states L, C or R can be written similarly to Eq. (1.3), with tunneling coupling rates J_{LC} between states L and C, and J_{RC} between states R and C, while no direct coupling is considered between the outermost traps:

$$i\ \frac{d}{dt}\begin{pmatrix} a_R \\ a_C \\ a_L \end{pmatrix} = \frac{}{2}\begin{pmatrix} 2(\ _R + g\ a_R\ ^2) & -J_{RC}(t) & 0 \\ -J_{RC}(t) & 2(\ _C + g\ a_C\ ^2) & -J_{LC}(t) \\ 0 & -J_{LC}(t) & 2(\ _L + g\ a_L\ ^2) \end{pmatrix}\begin{pmatrix} a_R \\ a_C \\ a_L \end{pmatrix} \qquad (1.22)$$

Here, a_k are the amplitudes corresponding to the states k, with $k = R\ C\ L$, and the diagonal elements of the matrix are twice the oscillation frequencies of the asymptotic eigenstates. $_k$ is equal to E_k with E_k being the energy of the asymptotic vibrational eigenstate k disregarding the nonlinear interaction between particles. The term g

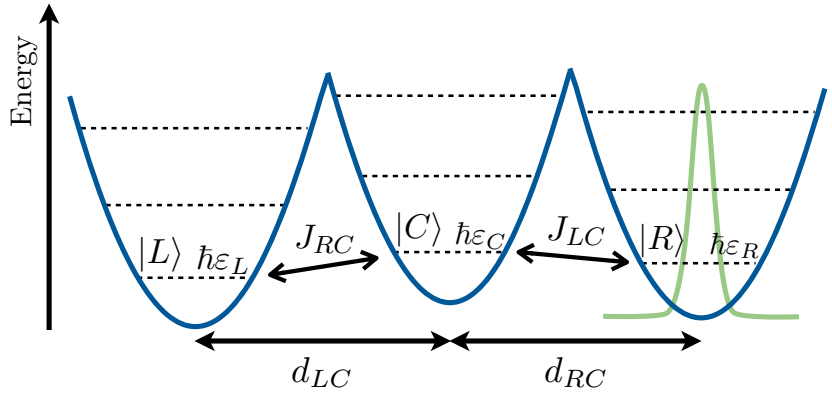

Figure 1.6: Schematic representation of a triple-well potential. The considered asymptotic eigenstates are the ground vibrational states of the traps, which are denoted as $|L\rangle$ for the left trap, $|C\rangle$ for the central trap and $|R\rangle$ for the right trap. The other asymptotic states are assumed to be far enough in energy not to be coupled with the three ground ones. The energy of the ground states is given by $\hbar\varepsilon_k$ with $k = L, C, R$ and the coupling rates between the states, J_{LC} and J_{RC}, depend on the separation distances d_{LC} and d_{RC} between the traps. A single particle or BEC wavefunction is represented in the ground state of the right trap, $|R\rangle$, which corresponds to the initial state of the system.

represents the nonlinear interaction. For a single particle g is equal to 0 and Eq. (1.22) is the time dependent Schrödinger equation. For BECs g accounts for the s-wave particle-particle interaction and Eq. (1.22) corresponds to the time dependent nonlinear Schrödinger equation or Gross-Pitaevskii equation [77].

For the single particle case, as for the STIRAP technique, if the oscillation frequencies of the asymptotic eigenstates $|L\rangle$ and $|R\rangle$ are set to be equal, $\varepsilon_R = \varepsilon_L$, a counterintuitive coupling sequence can be applied to transfer the single particle between the outermost traps by means of a spatial adiabatic passage process. In fact, Eq. (1.22) for the single particle case with the condition $\varepsilon_R = \varepsilon_L$ is completely analogous to Eq. (1.6), giving exactly the same eigenvalues and eigenvectors of the whole system. The dark state here is written as

$$|\Psi_{\text{dark}}\rangle = \cos\theta|R\rangle - \sin\theta|L\rangle, \tag{1.23}$$

where the mixing θ angle is also analogous to the STIRAP case

$$\tan\theta = \frac{J_{RC}}{J_{LC}}. \tag{1.24}$$

The main difference for the spatial adiabatic passage of a single particle compared to the STIRAP technique is the way to perform the counterintuitive coupling sequence.

Since the tunneling coupling rates depend on the separation between the traps, by changing the distance between the traps it is possible to change the coupling rates. Thus, for example, if the atom is initially in the right trap, first left and middle traps are approached and then separated and, with a certain temporal delay, right and central trap are approached and separated. This trap movement, which corresponds to a counterintuitive coupling sequence, allows for a modification of the dark state from $\Psi_{\rm dark}(t=0) = R$ to $\Psi_{\rm dark}(t=T) = -L$, where T represents the total time of the process. Therefore, if the eigenstate $\Psi_{\rm dark}$ is adiabatically followed during the process, a transfer of the atom from the right to the left trap is achieved, which represents an example of a spatial adiabatic passage process. Note that during the process the eigenvalues of the whole system do not cross each other, which allows for the adiabatic following. In particular, the adiabaticity condition for the transport is equivalent to the one in Eq. (1.15). The robustness of the transport has been numerically proved by adding oscillations to the movement of the traps and also considering a tilted potential [50]. Furthermore, an application of the spatial adiabatic passage in triple-potential wells is described in [78], where filtering of vibrational states is proposed based on the fact that coupling rates present higher values for higher vibrational states.

The scenario is not so simple to analyze when the spatial adiabatic passage transport is intended with BECs [72, 73, 74, 75, 53, 76]. Since the nonlinear terms depending on the population appear in the diagonal, it is not simple to fulfill the resonance condition between the asymptotic vibrational eigenstates of the right and left trap, i.e., to keep $_R + g\, a_R\,^2$ equal to $_L + g\, a_L\,^2$. The nonlinearity can lead to crossings in the energy eigenvalues that forbid the adiabatic following of the dark state. However, externally changing the trap parameters it is possible to modify $_R$ and $_L$ during the process in order to improve the results of the transfer. For example, in [72] it is shown that, imposing $\Delta = {}_C - {}_R = {}_C - {}_L$ (which implies that $_R = {}_L$), a complete population transfer between the external traps can be achieved by applying a counterintuitive coupling sequence if the following condition is fulfilled:

$$g\Delta \geq 0 \quad \text{and} \quad g < g_c = \Delta \tag{1.25}$$

The spatial adiabatic passage process described above, for both single particles and BECs, does not involve population in the central trap at any time during the process. However, this should not lead to the inappropriate idea that there is transport without transit [73, 74]. In [79], by using Bohmian mechanics (which provides an alternative description of Quantum Mechanics and, in particular associates trajectories to the wavefunction) it is clearly demonstrated the transit of both single particles and BECs through the central trap. Also by means of Bohmian mechanics, the same authors describe in [79] a counterintuitive effect of the spatial adiabatic passage processes in triple-well potentials: the slower is the trap movement is performed (implying a better adiabatic following of the dark state), the faster are the Bohmian velocities associated to the trajectories for the transport of the single particles or the BECs.

Spatial adiabatic passage processes have been also implemented to control the trans-

port of a BEC between the two coupled asymptotic vibrational ground states of a double-well potential [75]. In this case, if we call these asymptotic eigenstates of the individual traps as R for the right trap, and L for the left trap, the Gross-Pitaevskii equation describing the evolution of the BEC in the double-well potential is of the form of Eq. (1.3) and gives:

$$i \frac{d}{dt} \begin{pmatrix} a_R \\ a_L \end{pmatrix} = \frac{}{2} \begin{pmatrix} 2(_R + g\, a_R{}^2) & -J_{RL}(t) \\ -J_{RL}(t) & 2(_L + g\, a_L{}^2) \end{pmatrix} \begin{pmatrix} a_R \\ a_L \end{pmatrix} \tag{1.26}$$

where a_k are the amplitudes corresponding to states k , with $k = R\ L$, $J_{RL}(t)$ is the tunneling-coupling between the right and left trap, while the diagonal elements of the matrix are twice the oscillation frequencies of the asymptotic eigenstates. The term g represents the nonlinear interaction. As for the triple-well potential, other eigenstates are assumed to have energies very far from the ones of R and L and then unable to couple to them and participate in the evolution.

Because of the nonlinear term, the eigenvalues and eigenstates of the system are not necessarily similar to the ones for the RAP technique in Section 1.3.1. In reference [75], after a detailed analysis of the evolution of the energy eigenvalues and the bifurcations, the authors show that, by appropriately modifying the coupling and the energy difference between the asymptotic eigenstates in time, it is possible to (i) equally split the BEC between the right and left traps and (ii) to transfer completely the BEC between the two traps, within certain ranges of parameter values.

In the case that $g = 0$, as for example for a single particle in the double well potential, the eigenvalues and eigenstates of the system are much easier to calculate and are completely analogous to the ones shown for the RAP technique in Subsection 1.3.1. In particular, since the mixing angle would correspond to $\tan\theta = J_{RL}\ \Delta$, with $\Delta = \ _R - \ _L$, by changing the ratio $J_{RL}\ \Delta$ similarly as for the RAP technique, it would be possible to modify the two eigenstates of the system and, by following them, transfer the single particle between the two potential wells.

1.3.3 Propagation-dependent adiabatic passage

Spatial adiabatic passage processes have not only been implemented as time-dependent processes but also as propagation-dependent processes. This is the case of different systems of coupled waveguides, which can be used to control the propagation of light [43, 44], sound waves or cold atoms [51, 80]. Although the detailed explanation of the spatial adiabatic passage processes in these three systems will be described in the chapters 3, 4 and 5, respectively, below we present the basic common elements in all these systems.

Cold atoms propagating in systems of dipolar waveguides are an intermediate example, where both time and propagation are directly related through the propagation velocity of the atoms in the waveguides. Thus, these systems of dipolar waveguides can be seen as triple-potential wells, where the distance between the traps changes with

the position along the propagation direction z of the atom in the system of waveguides. Considering a triple-waveguide system, if we assume only the coupling of one transversal vibrational state per each waveguide (R , C and L for the right, central and left waveguides, respectively), with oscillation frequencies $_k$ with $k = R\ C\ L$, and couplings J_{LC} between the left and central waveguides and J_{RC} between the right and central waveguides, then the Schrodinger equation in (1.22) with $g = 0$ can be used to describe the evolution of the probability amplitude, with analogous results as for single particles in potential wells. In this case, since the atomic velocity relates t with z, the evolution of the probability amplitudes and the couplings can be represented as a function of z. The spatial adiabatic passage process for cold atoms propagating in a system of three coupled identical waveguides will be described in detail in Chapter 4. In there, the fact that the waveguides are taken identical will imply that $_R = _C = _L$ since the transversal vibrational eigenstates will be of the same energy.

Regarding light or sound propagation in systems of waveguides we will work with continuos wave beams. Thus, the variable accounting for the evolution cannot involve time but only the propagation direction z. In these systems, the oscillation quantity is a wave (electromagnetic field or sound pressure and velocity), the asymptotic eigenvectors of the system are the modes of the individual waveguides, the coupling coefficients are usually due to the evanescent fields and depend on the separation between the waveguides, and the oscillation frequency of a mode of an individual waveguides corresponds to the propagation constant in that waveguide. In this way, for example, for a system of three coupled waveguides and considering only one mode per waveguide (either because the waveguides are single mode or because the propagation velocity of other modes is very different from the three considered ones), the coupled-mode equations [81] describing the wave propagation in the most general way are of the form of Eq. (1.3) and read

$$i\ \frac{d}{dz}\begin{pmatrix} a_R \\ a_C \\ a_L \end{pmatrix} = \frac{1}{2}\begin{pmatrix} 2k_R & -\Omega_{CR}(z) & 0 \\ -\Omega_{RC}(z) & 2k_C & -\Omega_{LC}(z) \\ 0 & -\Omega_{CL}(z) & 2k_L \end{pmatrix}\begin{pmatrix} a_R \\ a_C \\ a_L \end{pmatrix} \tag{1.27}$$

where a_k are the amplitudes corresponding to the individual modes of the waveguides with $k = R\ C\ L$, Ω_{kl} is the coupling coefficient from the k to the l mode, and k_k is the propagation constant of the k mode. It is assumed that the right and the left waveguides are not directly coupled. Thus, diagonalizing the matrix in Eq. (1.27) it is possible to find the eigenvectors of the system of waveguides, the supermodes, as well as the eigenvalues, which are the propagation constants of these supermodes. In most of the cases the coupling coefficients between two waveguides can be considered equal, i.e., $\Omega_{kl} = \Omega_{lk}$, which greatly simplifies the diagonalization problem.

Further details about the implementation of the spatial adiabatic passage for light propagation will be given in Chapter 2. As well, spatial adiabatic passage processes for sound propagation will be studied in Chapter 3.

2

Spatial adiabatic passage of light

This chapter is structured into two main parts based on the two recently published papers [82] and [83], where we discuss theoretically and experimentally the basic applications of the spatial adiabatic passage of light. In the first part, we present a fully complementary metal-oxide-semiconductor (CMOS)-compatible spatial adiabatic passage of light working in the visible range. We experimentally show that a system of three total internal reflection (TIR) waveguides, which has been defined by using non-stoichiometric silicon oxide, with variable separation along their propagation direction allows for a highly efficient transfer of light between the outermost waveguides by adiabatically following one supermode of the system. This transfer of light is the so-called spatial adiabatic passage of light. We also demonstrate that such transfer is very robust against small variations of the system parameters. In the second part of the chapter, we present the first experimental realization of a light spectral filter based on the spatial adiabatic passage of light. We show that a triple-waveguide structure (of fully integrable CMOS-compatible identical TIR silicon oxide waveguides) can be used simultaneously as a low- and high-pass spectral filter within the visible range of wavelengths. If a light beam is injected into the right waveguide, after propagating along the system, long wavelengths are transferred into the left output, whereas short wavelengths propagate to the right and central outputs. The stopband of the filter reaches values up to $-11\,\mathrm{dB}$ for the left output and approximately $-20\,\mathrm{dB}$ for the right plus central outputs. The passband values are close to $0\,\mathrm{dB}$ for both cases. We also demonstrate that the filtering characteristics of the filter can be controlled by modifying the parameter values, which define the geometry of the triple-waveguide system. However, the general filtering behavior of the system does not critically depend on technological variations. Thus, our proposal of spatial adiabatic passage filtering constitutes an alternative to other integrated filtering devices, such as interference or absorbance-based filters.

2.1 Introduction

Photonic integrated circuits (PICs) have the potential to revolutionize computing platforms due to the high speed and quality of light-based communications. PICs could enhance the performance of the more traditional electronic components, whose progress might be shrunk due to the limited capability of the electronic connections data bandwidth. Using light as a carrier of information allows much higher data rates and avoids problems related to electromagnetic interferences. Furthermore, miniaturization of electronic components is reaching the limits of classical physics and a possible solution to push further the limits of classical computing could be to use integrated waveguide circuits for optical computing [84]. Additionally, photonic integration has been recently pushed forward by taking advantage of complementary metal-oxide-semiconductor (CMOS)-compatible technology, which allows high quality PICs to be obtained with high-index contrasts [85, 86]. Due to this contrast, sharp bends can be implemented, leading to significant miniaturization of the optical components. Furthermore, CMOS-compatibility allows the usage of already developed mass-production fabrication techniques for electronic components on the one hand and the monolithic integration of PICs with additional electronic circuits on the other hand. In this context, several research groups have successfully characterized silicon-based PICs, such as couplers, power splitters, optical modulators, wavelength demultiplexers (WDMs) and filters [87, 88, 89, 90]. However, huge efforts are still required in order to implement real PICs able to replace and improve the traditional electronic integrated circuits. Therefore, new techniques offering full control of light propagation in silicon based optical devices are fully desirable.

In particular, integrated wavelength filtering structures have attracted significant interest mainly due to their potential to be applied not only in telecommunication applications, but also in other fields, such as spectroscopy [91] or sensing [92]. Different strategies and geometries toward implementing all-optical integrated PICs for filtering have been previously presented. Several types of interference-based integrable spectral filters have been proposed. First, structures that are commonly called single channels, with the most representative being ring resonators [92] and Mach Zehnder interferometers [93]. Second, a more advanced configuration uses multiple channels or WDMs, in which the current trends are arrayed waveguide gratings [94] and planar concave gratings (also known as echelle gratings) [95]. With respect to ring resonators, high Q values are obtained due to the strong field enhancement caused by recursive light propagation inside the structure. This feedback, however, also causes nonlinearities, which distort the device response. Regarding Mach Zehnder interferometers, the main open issue is related to the precise coupling ratio required between the stages, which basically depends on the critical technological steps, as well as the matching between the delay lengths. In the case of WDMs, planar concave gratings have the advantage of a minor footprint; however, in arrayed waveguide gratings, it is possible to selectively tune each delay line and, in general, there is significantly larger

design freedom. Nevertheless, in both cases, the required technology is critical, and the robustness against technological variations is very low. The shallow etch configuration [96] partially solves this issue, but at the expenses of requiring an additional and highly accurate photolithographic step, and still demands highly precise etching steps. In this context, spectral filtering structures based on both single and multiple channels require an extremely robust technology that uses both critical alignment and etching steps. Nevertheless, they are undoubtedly the workhorse of telecommunication applications. It is also true that such strict technological steps clearly hamper their applications where instead of narrow and sharp peaks, robustness and technological simplicity are key issues. Absorbance-based integrated filters offer an alternative [97]. Typically, their stopband and passband extend to a broad region instead of presenting single/multiple peaks, and absorbance-based integrated filters are easy to implement and characterize. However, the difference between the passband and stopband is not as high when compared to that of interference filters, and the spectral filtering cannot be tuned because it depends either on the particular organic compound [98] or on the bandgap material in the filter [99].

Recently, it has been shown that in a system of three identical coupled waveguides it is possible to transfer a light beam between the outermost waveguides in a very efficient way by means of adiabatically following a supermode of the system that only involves the two outermost waveguides, the so-called spatial adiabatic passage of light [82, 43, 44]. This new technique offers full control of light propagation. As a proof of principle [43], such adiabatic passage technique was implemented in waveguides fabricated by the Ag-Na ion exchange technique applying a titanium mask onto an Er:Yb-doped glass substrate. Although effective, this technology has a relative impact since it is not CMOS-compatible and therefore it cannot be monolithically implemented with other electronic circuits. In addition, the geometries suitable to be obtained with ion-exchange are quite limited, hampering the applicability of the adiabatic passage of light. In [44], although they use standard photolithographic techniques, the fabricated waveguides in [44] are intended for the study of nonlinear effects on the spatial adiabatic passage of light. In this chapter, we present the first implementation of the spatial adiabatic passage technique for visible light with a fully CMOS-compatible technology. Concretely, three total internal reflection (TIR) [100] non-stoichiometric silicon oxide rib waveguides have been used to define the spatial adiabatic passage geometry, representing an important technological improvement since it allows a massive and low-cost fabrication of these devices and their incorporation to realistic PICs.

Additionally, we introduce a completely new method of light spectral filtering, based on the spatial adiabatic passage of light technique [82, 43, 44]. We experimentally demonstrate that a system of three identical TIR silicon oxide coupled waveguides can act simultaneously as a high- and low-pass spectral filter for the visible range, separating the long and short wavelengths among the different waveguides [83]. We will refer to this type of filter as a spatial adiabatic passage (SAP) filter. The proposed configuration shows a different filtering behavior compared to interference filters [96], because there

is an absence of periodic peaks but a wide transmission band, while maintaining a moderate difference between the passband and stopband values. Moreover, in contrast to absorbance-based filters [97], the filtering characteristics of the SAP filter can be modified by varying the geometric parameters of the structure. However, variations in a given geometric parameter value do not imply a severe change in the spectral response. Therefore, in contrast to the interference filters, the SAP filters proposed here have high technological robustness. Furthermore, the SAP filter triple-waveguide system is also fully CMOS-compatible and technologically simple to fabricate, requiring only one, non-critical photolithographic step. As such, SAP filters can be monolithically implemented with other electronic elements into PICs with a low-cost and mass-production.

2.2 Spatial adiabatic passage of light in CMOS-compatible silicon oxide waveguides

2.2.1 Spatial adiabatic passage mechanism

The spatial adiabatic passage of light in systems of three identical single-mode evanescent coupled optical waveguides [82, 43, 44] (as the one schematically depicted in Fig. 2.1(a)) resembles the well known stimulated Raman adiabatic passage (STIRAP) technique [34] used in Quantum Optics to efficiently transfer atomic or molecular population between two internal states of a Λ-type three level system. Propagation of light is described by the evolution of the mode amplitudes a_i along the propagation direction z, with $i = R\ C\ L$ accounting for the right, central and left waveguides, respectively. Such evolution is given by the coupled-mode equations [81, 100]:

$$i\frac{d}{dz}\begin{pmatrix} a_R \\ a_C \\ a_L \end{pmatrix} = \frac{1}{2}\begin{pmatrix} 0 & \Omega_{RC}(z\ \lambda) & 0 \\ \Omega_{RC}(z\ \lambda) & 0 & \Omega_{LC}(z\ \lambda) \\ 0 & \Omega_{LC}(z\ \lambda) & 0 \end{pmatrix}\begin{pmatrix} a_R \\ a_C \\ a_L \end{pmatrix} \tag{2.1}$$

where Ω_{LC} (Ω_{RC}) is the coupling coefficient between the left (right) and the central waveguides and λ is the wavelength. Since weak coupling is assumed, we consider that the right and left waveguides are not directly coupled.

Diagonalizing Eq. (2.1), it can be seen that one of the eigenvectors of the system (supermode) only involves light in the right and left waveguides:

$$D(\theta) = \begin{pmatrix} \cos\theta \\ 0 \\ -\sin\theta \end{pmatrix} \tag{2.2}$$

with $\tan\theta \equiv \Omega_{RC}\ \Omega_{LC}$. Since the couplings are due to the evanescent fields, they can be easily modified by engineering the transverse waveguide separation along the z propagation direction. In particular, we consider the right waveguide of the triple-waveguide system to be excited by the input light source, and the spatial configuration

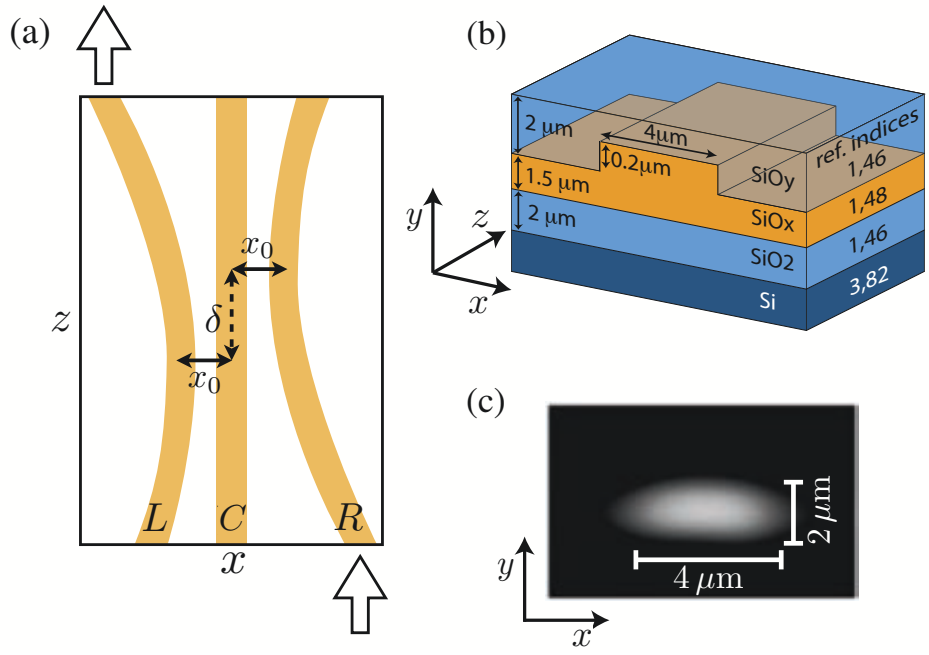

Figure 2.1: (a) Schematic top view of the geometry of the system of waveguides consisting of two circularly bent outermost waveguides, left (L) and right (R), and one straight central waveguide (C). The minimum distance between waveguides is given by x_0, and the z distance between the centers of the curved waveguides is defined by δ. (b) Schematic representation of the geometry, specifying the materials and refractive indices of one of the three TIR waveguides that integrate the system. (c) Experimental profile of the intensity of the fundamental mode of one of the waveguides. Light is mostly confined and propagates in the z direction inside the SiO_x layer with index 1 48. In particular, ribs, which define the waveguides, are used to confine light in the x horizontal direction, whereas the difference of refractive indices between layers confines light in the vertical direction y.

of the waveguides forces the couplings to follow a counterintuitive sequence along z. Initially, the left waveguide approaches the central waveguide. Later, and with a certain overlap, the right waveguide approaches the central waveguide, whereas the left waveguide separates from the central waveguide, as shown in Fig. 2.1(a). With this spatial configuration, the mixing angle, θ, evolves from 0 to ω 2. If the modification of θ is adiabatically performed, the supermode (2.2) is followed, avoiding the excitation of the other two supermodes of the system, and light will be efficiently transferred between the outermost waveguides (from right to left in our case) without the propagation of light intensity into the central waveguide. We can understand this process by showing the evolution along z of the supermode (2.2) of the structure [101, 102]. In

Fig. 2.2, we plot the intensity profile of the supermode (2.2) from numerical simulations at three different positions along z (input, middle and output). The input light into the right waveguide corresponds to the initial spatial distribution of the supermode (2.2) of the complete structure. Since the geometry of the system is being transformed adiabatically, all of the power remains in the supermode (2.2), being finally transferred to the left waveguide. As expected from supermode (2.2), the central waveguide is not involved in the process.

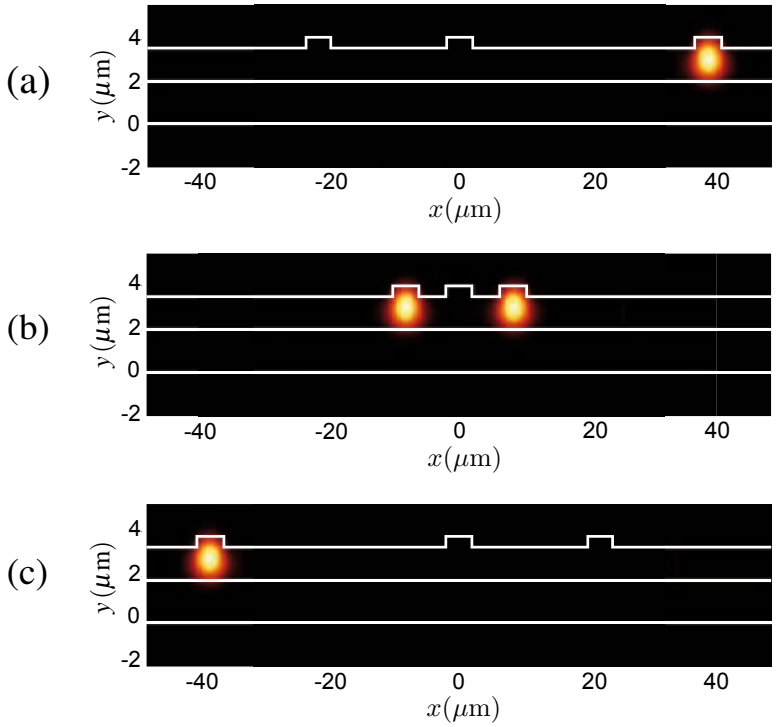

Figure 2.2: Numerical simulations of the supermode (2.2) of the triple-waveguide system at three different positions along z: (a) input, (b) middle, (c) output. Simulations are calculated with $\lambda = 800\,\text{nm}$ and geometrical parameter values $x_0 = 7\,\mu\text{m}$ and $\delta = 4700\,\mu\text{m}$.

This light transfer is the so-called spatial adiabatic passage of light [82, 43, 44]. As we will demonstrate in next sections, the spatial adiabatic passage of light is a robust process, i.e., the light transfer is efficient for a broad range of parameter values of the waveguides as long as the transfer is perfomed adiabatically. This also implies that the process is almost insensitive to relatively large fluctuations in these parameter values, an important feature that directional couplers do not exhibit [87]. Notice also that in a similar fashion, the spatial adiabatic passage technique has been proposed for the

robust and efficient transfer of neutral atoms in triple-well traps and waveguides and for the filtering of vibrational matter wave states [50, 51, 78].

2.2.2 Design, fabrication and experimental setup

The optimization of the geometry of the system of three coupled waveguides has been carried out by numerical simulations using the software Fimmprop and Fimmwave (Photon Design). We have numerically checked that the adiabatic transfer of light is independent of the polarization of the incident light. The parameter values obtained in the simulations have been used to design the masks for the fabrication process. Nevertheless, several devices with slightly different parameter values have been considered in such designs taking into account possible small variations between simulations and experiment, and to test the robustness of the adiabatic passage.

The fabrication process of the silicon based integrated optical waveguides can be summarized as follows. First, a layer of $2\,\mu$m of silica SiO_2 is thermally grown on a (100) silicon wafer. Then, a layer of non-stoichiometric silicon oxide SiO_x with a height of 1 $7\,\mu$m and a refractive index of 1 48 is deposited over the silica layer by plasma enhanced chemical vapor deposition (PECVD). At this point, waveguides are obtained by defining ribs with a thickness of 0 $2\,\mu$m and width of $4\,\mu$m in the SiO_x layer by using the appropriate mask and dry etching. Finally, another layer of non-stoichiometric silicon oxide SiO_y of $2\,\mu$m with index 1 46, acting as a passivation layer, is deposited on the top of the device using PECVD. Fig. 2.1(b) represents the transverse profile of one of the waveguides of the system including the sizes of the different layers and the values of the refractive indices, which were checked by ellipsometry [103]. Fig. 2.1(c) shows the experimental profile of light intensity of the fundamental mode at the output of one of the waveguides.

The experimental setup consists of a diode laser (Thorlabs S1FC635, Newton, New Jersey, USA) emitting at 635 nm connected to one end of a single-mode optical fiber. The other end of this fiber is placed over a piezoelectric 3D positioning system (piezosystem jena NV40/3, Jena, Germany), which allows accurate fiber optics-waveguide alignment. Light propagating inside waveguides is collected by an infrared single-mode optical fiber located on another piezoelectric positioning system (piezosystem jena d-Drive) and transferred to a power meter (Newport 1930F-SL, Irvine, USA).

2.2.3 Experimental results and discussion

Insertion and attenuation losses were determined by measuring identical waveguides of different lengths, obtaining values of $3\,6 \pm 0\,3$ dB and $0\,36 \pm 0\,01$ dB mm, respectively. In order to characterize the coupling coefficients $\Omega_{RC,LC}$, we have manufactured systems of two parallel waveguides with different separation distances d between their centers: $7\,\mu$m, $7\,5\,\mu$m, $8\,\mu$m, $8\,5\,\mu$m, $9\,\mu$m and $10\,\mu$m. Coupling coefficients for the different distances are obtained by measuring the spatial period of the intensity oscillations between pairs of waveguides. The experimental results may be fitted by the decaying

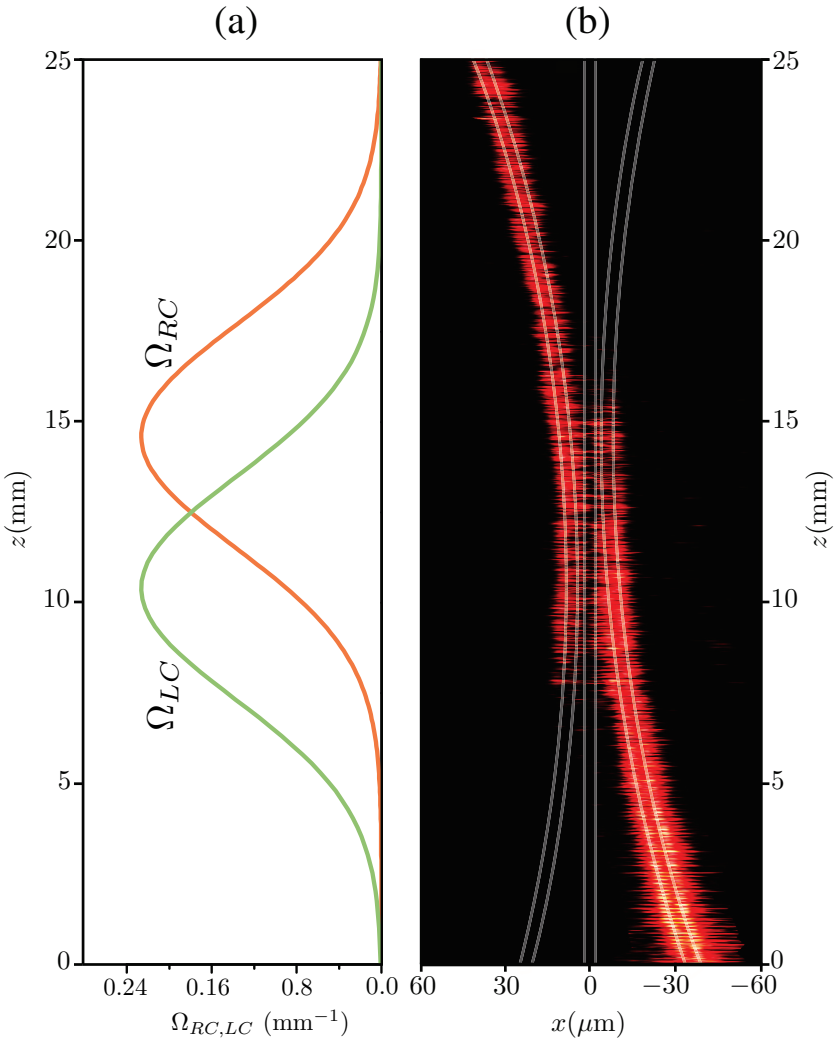

Figure 2.3: (a) Counterintuitive sequence of the experimentally measured coupling coefficients $\Omega_{RC,LC}$ along the propagation direction z. (b) Top view image of one of the fabricated devices in which light losses allow us to observe the adiabatic transfer of light between the outermost waveguides with almost no intensity in the central waveguide. Schematic representation of the waveguides is depicted on the experimental image.

exponential curve $\Omega(d) = \Omega_0 \exp^{-d/l}$ with $\Omega_0 = 29\ 8 \pm 3\,\mathrm{mm}^{-1}$ and $l = 2\ 72 \pm 0\ 09\,\mu$m. This dependence allows us to check that the coupling coefficients $\Omega_{RC,LC}$ along the z propagation direction in the fabricated systems of three waveguides fulfill the adiabaticity required to follow only the supermode (2.2) and avoid the excitation of the other supermodes [43].

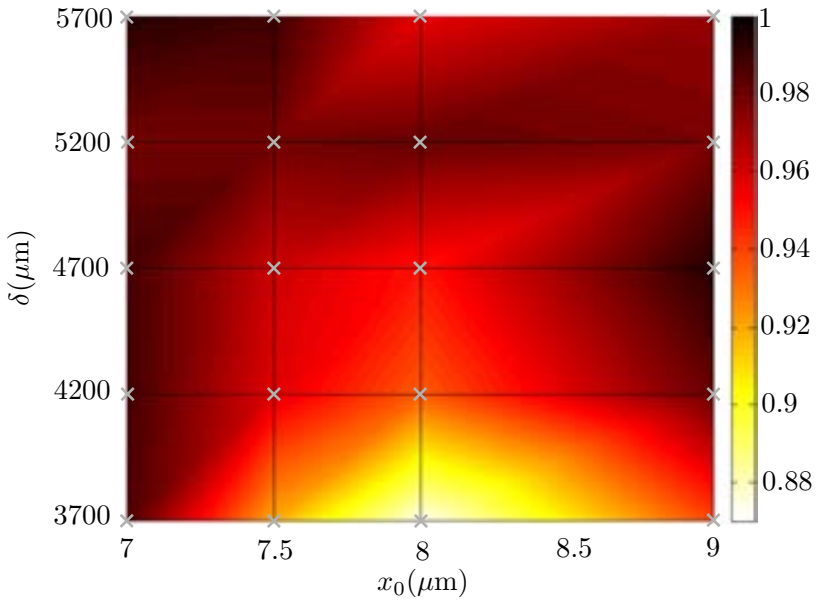

Figure 2.4: Relative fraction of light intensity at the output of the left waveguide of the system, I_L $(I_L + I_C + I_R)$, as a function of δ and x_0. Crosses indicate the experimental measurements.

Fig. 2.3(a) shows the experimentally determined counterintuitive sequence of coupling coefficients $\Omega_{RC,LC}$ along z for one of the fabricated systems of three waveguides with the following parameters: radius of curvature of the outermost waveguides 3 5 m, spatial delay $\delta = 4200\,\mu$m and minimum separation between waveguides $x_0 = 7\,\mu$m. A complete top view image of the path followed by the light beam across the same system of waveguides has been obtained by taking several pictures with a charge-coupled device camera connected to an optical microscope, see Fig. 2.3(b). The image confirms the adiabatic transfer of light from the right to the left waveguide, with almost no intensity in the central waveguide.

We have also checked the robustness of the spatial adiabatic passage in the fabricated systems of three coupled waveguides by measuring the intensity of light at the outputs of the three waveguides (I_L, I_C and I_R) for different devices. Fig. 2.4 shows the relative fraction of light intensity at the left output, I_L $(I_L + I_C + I_R)$, for different devices with δ and x_0 parameters varying from 3700 μm to 5700 μm and from 7 μm to 9 μm, respectively. The radius of the external waveguides is kept equal to 3 5 m for all the measured devices. The highest measured relative fraction values of light ending up into the left waveguide are above 0 99 whereas the lowest measured relative fraction is higher than 0 87, demonstrating the low sensitivity of the adiabatic passage to small variations of the parameters.

2.3 Light spectral filtering based on spatial adiabatic passage

In this section we present the first experimental realization of a light spectral filter based on the spatial adiabatic passage technique [83]. We use a very similar triple waveguide system compared to the one presented in the previous section (composed of fully integrable CMOS-compatible identical TIR silicon oxide waveguides) and we show that it can simultaneously work as a low- and high-pass spectral filter within the visible range of wavelengths. The precise parameter values of the waveguides as well as a schematic depiction of the triple waveguide system are shown in Fig. 2.5.

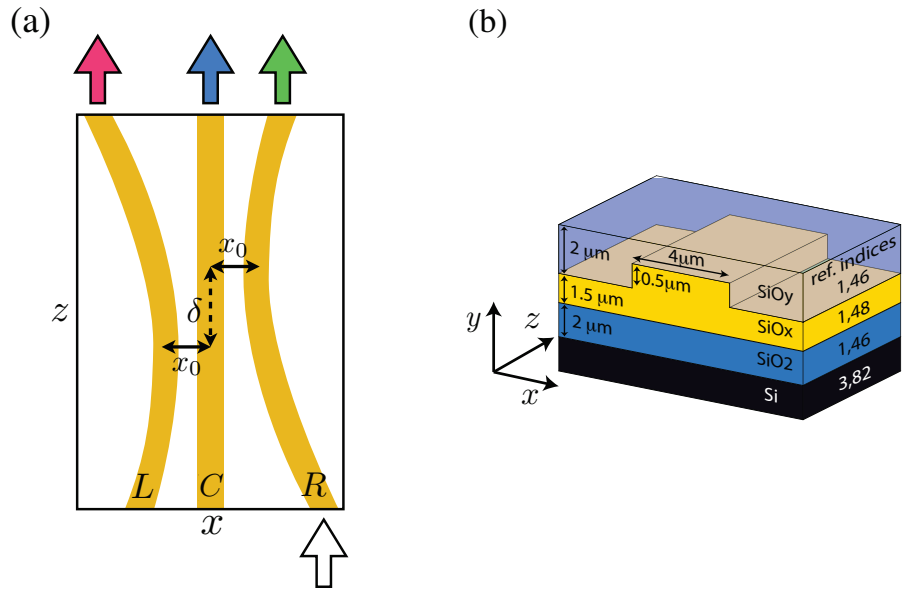

Figure 2.5: (a) A schematic depiction of the SAP filter geometry, viewed from above, consisting of one straight central waveguide (C) and two circularly bent external waveguides, right (R) and left (L). The z separation between the centers of the bent waveguides is given by δ, and the minimum separation between waveguides is defined by x_0. The devices total length in the z direction is $D = 2\,5\,\text{cm}$ and the external waveguides radius of curvature is $r = 3\,5\,\text{m}$. (b) A schematic representation of the different layers of one of the rib waveguides, specifying the refractive indices and materials.

2.3.1 Spatial adiabatic passage filtering mechanism

As it was previously discussed in Section 2.2.1, the propagation of light into a system of three identical single-mode evanescent coupled waveguides can be described through coupled mode equations Eq. (2.1). However, in this section we also take into account

that in the evanescent couplings depend on the wavelength of the propagating light, λ. Generally, this dependence is approximately linear with λ [81]. Thus, considering two identical straight TIR waveguides separated by a distance d, the evanescent coupling can be expressed as:

$$\Omega(\lambda\ d) = \Omega_0(\lambda)\exp(-d\ l(\lambda)) \tag{2.3}$$

Numerical simulations using Fimmprop and Fimmwave (Photon Desing) of light propagating in a system of two straight waveguides with the parameters indicated in Fig. 2.5(b) for several separation distances d confirm that, for a fixed distance d, $\Omega(\lambda\ d)$ increases linearly with λ for the range of wavelengths of interest in this work (from 400 to 950 nm), as shown in Fig. 2.6(a). Additionally, from these simulations, we have obtained the dependence of the decay constant, $l(\lambda)$, on λ, which also grows linearly for the range of working wavelengths.

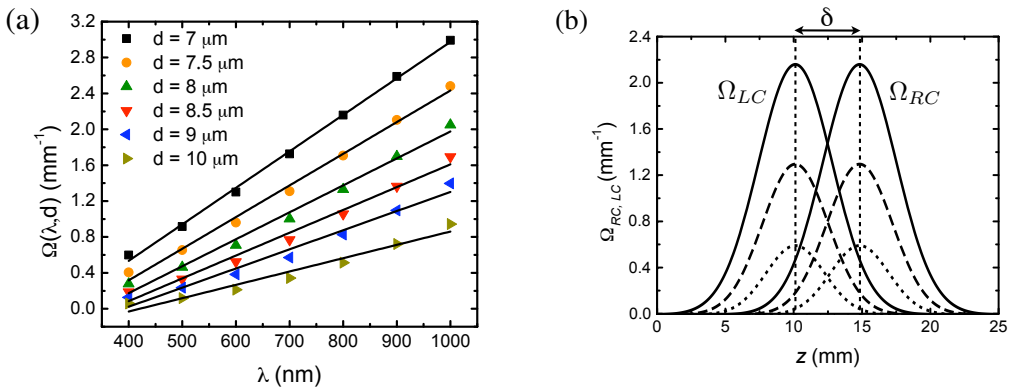

Figure 2.6: Numerical simulations used for the characterization of the couplings. (a) Dependence of the coupling coefficient between two straight TIR waveguides (with the characteristics specified in Fig. 2.5(b)), $\Omega(\lambda\ d)$, on λ for fixed distances d. The simulation points are fitted by straight lines. (b) Typical counterintuitive sequence of couplings coefficients along z in a system of three coupled waveguides obtained from numerical simulations with $x_0 = 7\,\mu$m and $\delta = 4700\,\mu$m for different wavelengths: 400 nm (dotted), 600 nm (dashed) and 800 nm (solid). The increase in strength and width of the couplings along the z direction can be observed as the wavelength λ increases.

Using expression (2.3) for the coupling between each set of two pairs of waveguides in the triple-waveguide system (Fig. 2.5(a)) and considering the dependence of the separation between waveguides along z, we obtain the variation of the couplings along z, which follows a Gaussian function:

$$\Omega_{RC,LC}(z\ \lambda) \approx \Omega(\lambda\ x_0)\exp\left[\frac{(-z - D\ 2 \pm \delta\ 2)^2}{2rl(\lambda)}\right] \tag{2.4}$$

where δ is the spatial delay between the outermost waveguides, x_0 is the minimum separation between waveguides, D is the total length of the system and r is the value of the radius of the external waveguides (see Fig. 2.5(a)). The first factor at the right-hand-side of Eq. (2.4),

$$\Omega(\lambda\ x_0) \equiv \Omega_0(\lambda) \exp\left(-x_0\ l(\lambda)\right) \tag{2.5}$$

gives the maximum value of the couplings along z. It is analogous to expression (2.3), and therefore, it has the same linear dependence on λ for fixed values of x_0. Moreover, the term $2rl(\lambda)$ in Eq. (2.4) indicates the width of the Gaussian along z. Since $l(\lambda)$ grows linearly with λ, the width of the coupling variation along z increases as λ increases. In Fig. 2.6(b), using the numerically obtained couplings, we represent the spatial dependence of the couplings in the triple-waveguide system for different values of the wavelength. We can observe that the strength and the width of the couplings increase as the wavelength, λ, increases. Note that we have numerically verified that the waveguides used in this work (Fig. 2.5(b)) are effectively single-mode within the working wavelength range ($400 - 950\,\text{nm}$) and that the coupling rates are polarization independent.

In the SAP filter system composed of three coupled waveguides, light is transferred between the outermost waveguides if the adiabaticity condition is fulfilled, i.e., if the couplings Ω_{RC} and Ω_{LC} are strong enough, and the overlap between them along the propagation direction z (Fig. 2.6(b)) is long enough [82, 43, 44, 34]. Thus, for specific values of x_0 and δ of the geometry of the SAP filter, it may be that the couplings are only strong and wide enough along z to fulfill the adiabaticity requirements for long enough wavelengths. In this case, if light is injected in the right waveguide, longer wavelengths are transferred to the left waveguide. However, for short enough wavelengths, because the couplings are too weak, light is unable to reach the left waveguide, remaining in either the right waveguide or the central waveguide or in a combination of both. Therefore, if we take as the outputs of the SAP filter the left waveguide and the sum of the right and central waveguides, the SAP device simultaneously works as a high-pass and low-pass spectral filter based on the spatial adiabatic passage of light.

We can show more specifically the spectral filtering mechanism in the SAP triple-waveguide system by taking the adjusted parameters of $\Omega(\lambda\ x_0)$ and $l(\lambda)$ from the numerical simulations and introducing them into Eq. (2.4) and, finally, integrating Eq. (2.1). The results of the numerical integration for $x_0 = 7\,\mu\text{m}$ and $\delta = 4700\,\mu\text{m}$ are depicted in Fig. 2.7. Fig. 2.7(a) shows the transmittance at the output of the left, central and right waveguides relative to the total intensity as a function of the wavelength. Although the left waveguide output signal varies smoothly, power oscillations in the right and central waveguide outputs can be observed. Nevertheless, the right and central waveguides could be joined after the device, yielding the result shown in Fig. 2.7(b). In this case, the sum of the right and central outputs presents a significantly more robust behavior, and we can observe the predicted behavior of the SAP filter which works simultaneously as a high-pass and low-pass spectral filter. In par-

ticular, within the range of studied wavelengths, for the left waveguide (high-pass), we find a stopband that reaches a value of $-17\,\mathrm{dB}$ and a passband of $0\,\mathrm{dB}$. For the sum of the right and central waveguide intensities (low-pass), we find a stopband that reaches $-22\,\mathrm{dB}$ and a passband of $0\,\mathrm{dB}$. Taking into account that the device can work as a high- and low-pass spectral filter simultaneously, we define the cutoff wavelength, λ_c , as the wavelength for which half of the intensity is at the output of the left waveguide and half at the output of the other two waveguides. Thus, λ_c corresponds to a decrease in intensity of approximately $3\,\mathrm{dB}$ and to the point at which the two curves in Fig. 2.7 (b) cross each other. For the presented figure, the cutoff wavelength is $610\,\mathrm{nm}$.

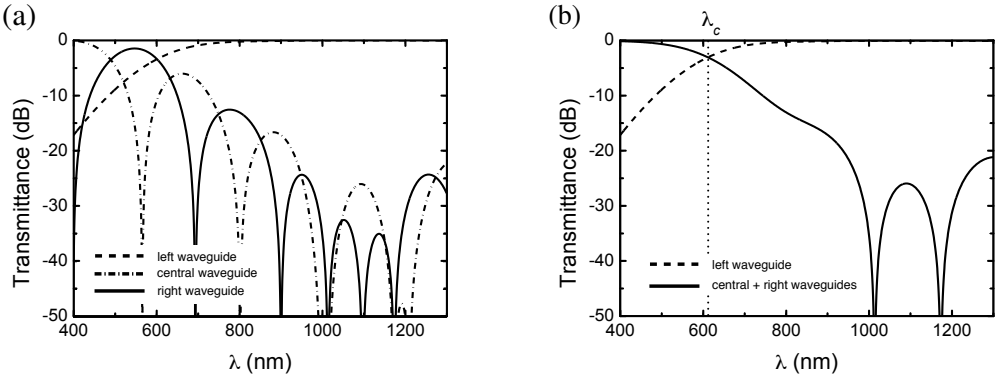

Figure 2.7: Results of numerical integration of Eq. (2.1) with parameter values $x_0 = 7\,\mu\mathrm{m}$ and $\delta = 4700\,\mu\mathrm{m}$. (a) Transmittance at the output of the left (dashed line), central (dashed-dotted line) and right (solid line) waveguides represented relative to the total output intensity as a function of the wavelength. In (b), the high- and low-pass filtering behavior for a SAP filter can be observed, represented as the transmittance at the output of the left (dashed line) and the sum of the central and the right (solid line) waveguides relative to the total output intensity with respect to the wavelength. No losses are considered when integrating Eq. (2.1).

Since SAP filtering is based on the robust technique of the spatial adiabatic passage of light as we discussed in Section 2.2, we expect a similar filtering behaviour, even though the geometric parameter values of the system are significantly modified. Nevertheless, studying the effect of varying the x_0 and δ parameters, we can observe that the specific filtering characteristics of the device (the cutoff wavelength, as well as the stop and passband regions) can be tuned by wavelength. On the one hand, if the spatial delay value δ is increased, the overlap between the couplings becomes smaller. Thus, only strong and wide enough couplings along z will fulfill the adiabaticity condition. On the other hand, if the minimum separation between the waveguides x_0 is increased, the strength of the couplings will be reduced, because the coupling values decay exponentially as the distance between the waveguides increases. Then, stronger and wider couplings (corresponding to long wavelengths) will also be required to main-

tain the adiabaticity of the process. In conclusion, the filtering characteristics, such as the cutoff wavelength, are moved to longer wavelengths as the values of x_0 and δ increase. The numerical simulations integrating Eq. (2.1) with the adjusted parameters $\Omega(\lambda\ x_0)$ and $l(\lambda)$ support this reasoning, as it can be observed in Fig. 2.8.

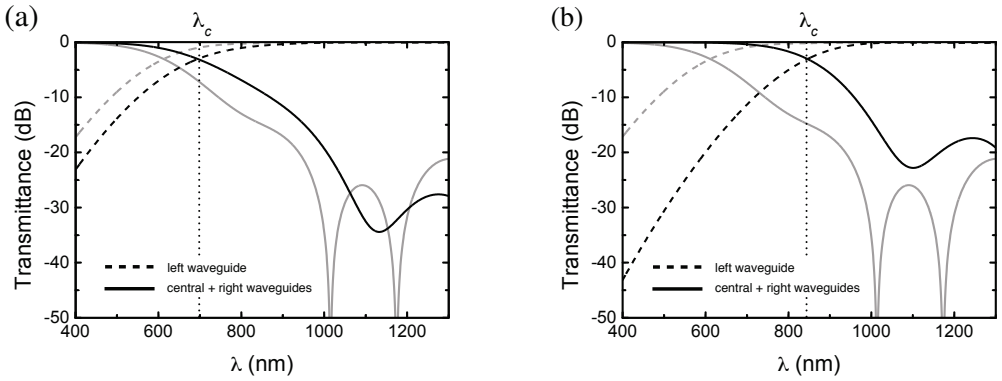

Figure 2.8: Numerical simulations of the high- and low-pass spectral filtering behaviour for a SAP filter with (a) $x_0 = 7\,\mu$m and $\delta = 5700\,\mu$m and (b) $x_0 = 9\,\mu$m and $\delta = 4700\,\mu$m. In comparison with the curves in Fig. 2.7 with $x_0 = 7\,\mu$m and $\delta = 4700\,\mu$m (light grey in these figures), we observe that when increasing the value of δ in (a) and x_0 in (b), the cutoff wavelength of the device is moved to longer wavelengths. In all the cases, the output of the left (central and right) waveguides corresponds to the dashed (solid) line.

2.3.2 Design, fabrication and experimental setup

Numerical simulations using Fimmwave and Fimmprop (Photon Design) were performed to optimize the geometry of the triple-waveguide SAP filter for different wavelengths and the obtained parameter values were used to define the required technological steps. The SAP filters were fabricated with a total length of 2 5 cm, and external waveguides were given a radius of curvature of 3 5 m. To obtain devices with different filtering characteristics, for every system of waveguides, slightly different parameter values of the spatial delay δ and minimum separation between waveguides x_0 were also fabricated.

The fabrication process for the triple-waveguide systems is analogue to the one explained in the Section 2.2.2, being the only difference the thickness of the rib. The filtering devices were fabricated with a 2-μm-thick layer of SiO_2, a non-stoichiometric silicon oxide SiO_x layer of 2 μm of height with defined ribs of 4 μm width and a thickness of 0 5 μm, and finally a 2-μm-thick passivation layer of non-stoichiometric silicon oxide SiO_y. Fig. 2.5(b) shows the transverse profile of a waveguide belonging to the triple-waveguide system, specifying the sizes of the layers and the refractive index values,

which were measured by ellipsometry [103].

The experimental setup is composed of a halogen white light source (Ocean Optics HL-2000-HP-FHSA, Dunedin, Florida, USA) connected to a 4-μm core optical fiber (Thorlabs 600HP, Newton, New Jersey, USA). The position of the other end of the fiber is controlled by a piezoelectric three-dimensional positioning system (Piezosystem Jena NV40/3, Jena, Germany), which provides nanometer-scale precision alignment between the optical fiber and the waveguide. The light emerging from the system is collected by another 4-μm core optical fiber, placed on another piezoelectric positioning system (Piezosystem Jena d-Drive) and transmitted to a microspectrometer (Ocean Optics QE65000).

With respect to the losses of the SAP filter, since the final goal of our proposal is to place the device into a PIC, we are mainly interested in the losses produced by the SAP geometry of the system, i.e., those losses due to the couplings and the bending of the waveguides, but not in the insertion and propagation losses, which depend on the characteristics of the specific waveguides. Thus, we studied the losses due to the adiabatic passage geometry by comparing the sum of the output intensities of the three waveguides of the device with the output of a single straight waveguide with equal features and the same length as the system of three waveguides. The experimental and numerical tests show that the losses due to the adiabatic passage geometry are negligible. With respect to the range of wavelengths available in the presented experimental setup, 400 to 950 nm can be sampled. The range is mainly limited by the allowed wavelengths propagating inside the fibers in addition to the sensitivity of the microspectrometer.

2.3.3 Experimental results and discussion

The results shown in Fig. 2.9 experimentally demonstrate the spectral filtering, based on the spatial adiabatic passage of light technique for one of the fabricated SAP filters with a minimum separation between waveguides of $x_0 = 9\,\mu$m and spatial delay $\delta = 5200\,\mu$m. Fig. 2.9(a) shows the intensity at the output of the left, central and right waveguides as transmittance relative to the total output intensity (we previously verified that the losses due to the adiabatic passage geometry are negligible). As expected from the numerical simulations, some power oscillations can be observed between the right and central waveguides, depending on the wavelength. However, we could join the right and central waveguides in a single waveguide just after the described triple-waveguide system by appropriately designing the photomask used for fabrication. By doing this, we would obtain an output corresponding to the sum of the right and central waveguides, which presents a significantly smoother and more robust behavior, as obtained from the numerical simulations in Section 2.3.1. Thus, Fig. 2.9(b) represents the experimentally measured intensity at the output of the left waveguide and the sum of the outputs of the right and central waveguides as the transmittance relative to the total output intensity.

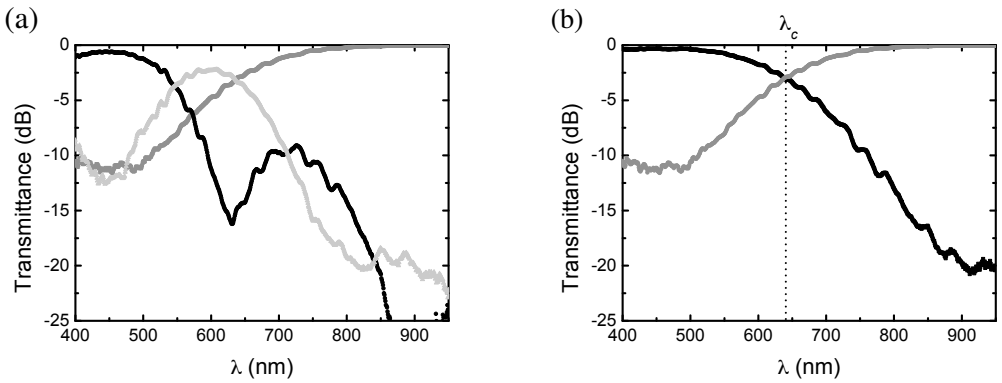

Figure 2.9: (a) Measured intensity, represented as transmittance at the left (grey), central (black) and right (light grey) outputs relative to the total output intensity as a function of the wavelength. (b) The measured intensity, represented as transmittance at the left (grey) and the sum of the central and the right (black) outputs relative to the total output intensity with respect to the wavelength. The parameter values for this specific device are $x_0 = 9\,\mu$m and $\delta = 5200\,\mu$m. The experimental cutoff wavelength in this case is $\lambda_c = 638\,$nm.

From this result, we experimentally conclude that the triple-waveguide SAP filter acts as a high-pass (output at the left waveguide) and low-pass (output at the central and right waveguides) spectral filter, representing a new and different filtering behavior in comparison to interference filters [96] and absorbance-based filters [97]. We have obtained a filtering efficiency between the efficiency of the interference and the absorbance-based filters. In particular, the measured values for the left waveguide output (high-pass) reach a value of approximately $-11\,$dB for the stopband, and the passband is close to $0\,$dB. For the sum of right and central (low-pass) waveguides, the stopband is approximately $-20\,$dB and the passband $-0\,5\,$dB. The measured cutoff wavelength is $638\,$nm.

As discussed in Subsection 2.3.1, SAP filters allow for a modification of the filtering characteristics (the cutoff wavelength, stopband and passband) by changing the parameter values δ and x_0. Fig. 2.10 shows the measured transmittance of various systems with different δ parameter values ($3700\,\mu$m, $4200\,\mu$m, $4700\,\mu$m, $5200\,\mu$m and $5700\,\mu$m) for different x_0 values ($7\,\mu$m, $7\,5\,\mu$m, $8\,\mu$m and $9\,\mu$m). Within the measurement range ($400-950\,$nm), similar slopes, values of the stop-band at approximately $-20\,$dB for the sum of the right and central waveguides and values up to $-12\,$dB for the left waveguide can be observed, which are expected to be lower for shorter wavelengths (not available with our setup). The values of the passband are very close to $0\,$dB for both cases whenever the value is within the measurement range. In Fig. 2.10, we also observe some oscillations of the transmittance for the sum of the central and right outputs, which supports the numerical analysis previously described in Subsection 2.3.1 and shown in

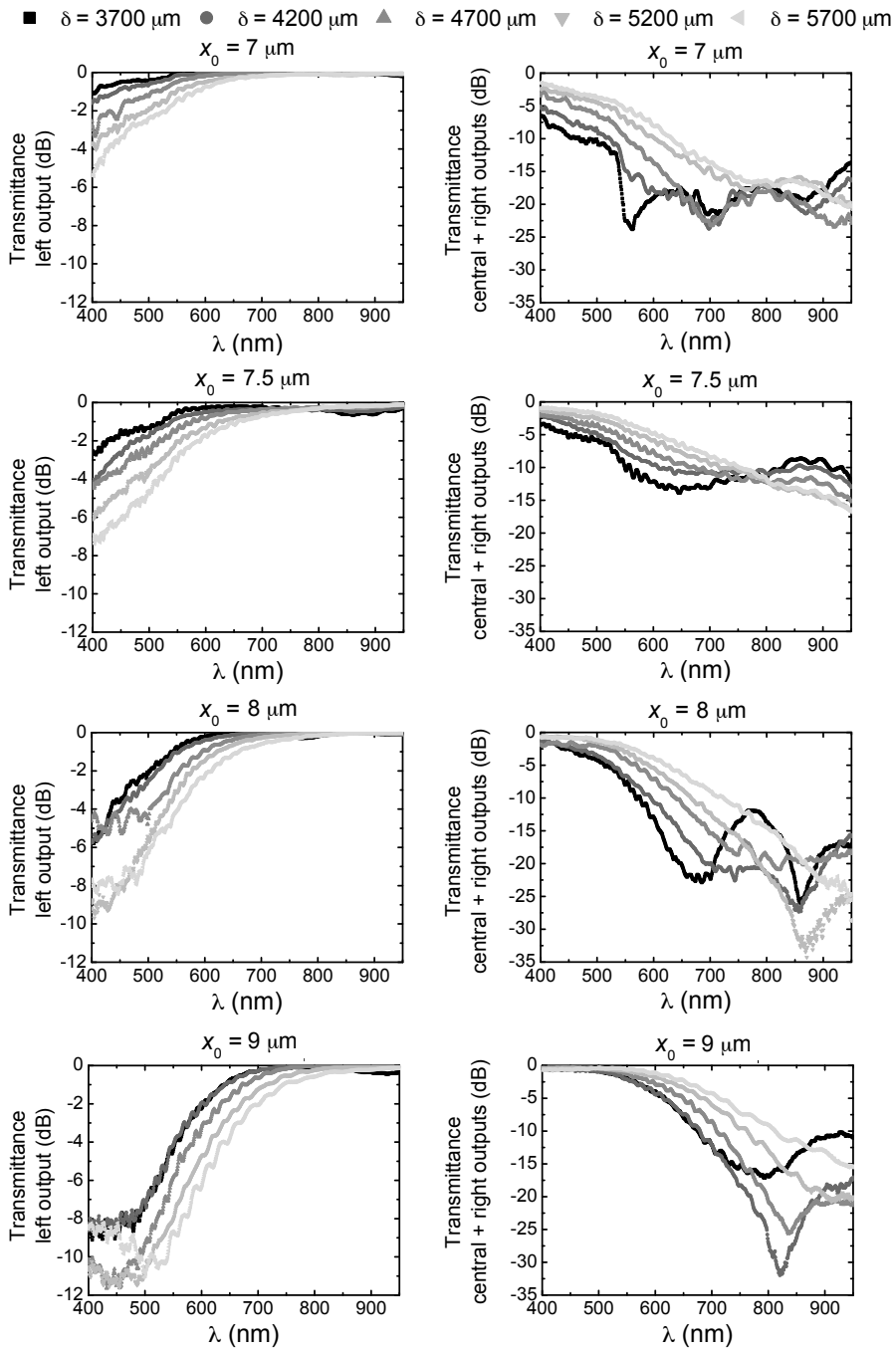

Figure 2.10: Experimental measurements of the left (upper row) and the sum of the central and right (lower row) output transmittance for different values of δ and x_0.

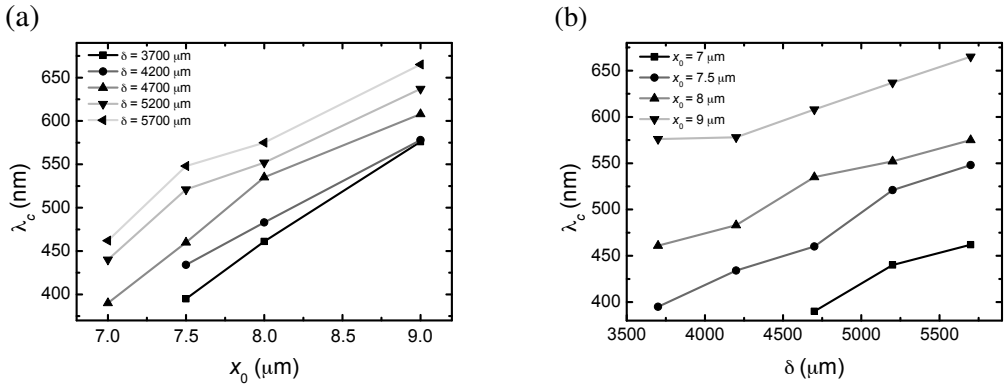

Figure 2.11: Variation of the cutoff wavelengths as a function of (a) x_0 for different values of δ and (b) δ for different values of x_0.

Fig. 2.7 and Fig. 2.8. These oscillations do not affect the high- and low-pass filtering behavior of the SAP filter. Furthermore, as already anticipated, for a fixed value of x_0, the transmittance curves are shifted to longer wavelengths for an increasing value of the δ parameter. Similarly, for a fixed value of δ, increasing the value of x_0 also shifts the transmittance curves to longer wavelengths. This change in the filtering characteristics represents an improvement in comparison to absorbance-based filters. Moreover, it can be observed that in contrast to interference filters, varying some of the geometric parameter values of the SAP filters does not imply that there is a drastic modification of the spectral response of the SAP filter.

Fig. 2.11 shows the evolution of the cutoff wavelength when varying the δ and x_0 parameter values. It can clearly be observed that the cutoff wavelength increases as δ and x_0 increase. Furthermore, Fig. 2.11 could be used to adjust the numerical simulations to the experimental results to obtain the value of the real couplings acting in the fabricated devices. If we compare the experimental figures (Fig. 2.9 and Fig. 2.10) with the numerical figures (Fig. 2.7 and Fig. 2.8), the qualitative filtering behavior is the same, although some differences arise. The first is that the stop-bands obtained through numerical simulations reach deeper values than the experimental stopbands. It can be observed that for some cases, the measured values of the intensity at extreme values of the considered range of wavelengths tend to stabilize; however, in the numerical simulations, the values continue evolving to lower transmittance values. This difference can be explained because at the limits of both short and long wavelengths, the efficiency of the microspectrometer used is very low. Therefore, the signal-to-noise ratio is very small. Additionally, the maximum dynamic range available with our setup is 35 dB, and consequently, the stopband values that can be measured are limited to this value. Nevertheless, such a value is sufficient to confirm the validity of the configuration proposed here. Second, it can be observed that for the experimental case, the filtering behavior is shifted to shorter wavelengths in comparison to the numerical

curves, which may be associated with a slight variation in the thicknesses and/or refractive indices of the layers in the fabrication process. However, this result does not affect the overall behavior of the proposed device. Additionally, the result confirms the devices robustness against technological variations and validates these SAP filters as efficient and cost-effective integrable devices.

2.4 Conclusions

Using CMOS-compatible technology, we have experimentally demonstrated that it is possible to achieve a highly efficient and robust transfer of light between the outermost waveguides of a system of three coupled identical waveguides by adiabatically following one supermode of the system. Thus, TIR silicon-based waveguides are very promising candidates for the control of the flow of light by means of the adiabatic passage technique in systems that can be monolithically implemented together with other integrated devices. Contrarily to directional couplers, where the transfer of light between waveguides depends on precise geometry parameter values, we have experimentally checked the robustness of the passage in systems of three waveguides against variations of the parameter values of the system. In particular, the measured relative fraction of intensity at the left waveguide output of several systems of waveguides ranges from 0 87 to values above 0 99, for variations of the geometry parameter values between 20% and 35%.

Aditionally, we have theoretically and experimentally demonstrated that it is possible to use a triple-waveguide system, with identical coupled TIR silicon oxide waveguides, as a simultaneous high- and low-pass spectral filter, based on the spatial adiabatic passage of light technique. Light is injected into the right waveguide of the system, and after propagating along the system, long wavelengths are transferred into the left output; in contrast, short wavelengths propagate to the central and right outputs. We refer to this device as the SAP filter, which constitutes the first experimental realization of an analogous of the STIRAP technique working as a filter. The SAP filter represents an alternative to other integrated filtering devices, such as interference filters or absorbance-based filters. Additionally, since the waveguides used in the fabricated SAP filters are fully CMOS-compatible, they could be monolithically integrated with other photonic and electronic elements into a PIC, allowing low cost and mass production. We have also demonstrated that upon varying the minimum distance between waveguides, x_0, and the spatial delay between the external waveguides, δ, the filtering characteristics of the system can be modified. In particular, we have shown that if the values of x_0 or δ are increased, the cutoff wavelength, which separates the low- and high-pass filtering regions, is shifted to longer wavelengths. In this way, by modifying the fabrication parameter values, it is possible to adapt the filtering characteristics of the device to fit specific requirements. However, these variations do not change the general filtering behavior of the SAP filter, which confirms its robustness with respect to technological variations.

3

Spatial adiabatic passage of sound waves

In this chapter, spatial adiabatic passage processes for sound waves propagation are investigated. Sound waves are guided through a system of two linear defects in a sonic crystal consisting of steel cylinders embedded in a water host medium. Different structures are designed leading the implementation of for instance a coherent multifrequency adiabatic splitter, a phase difference analyzer and a coherent multifrequency adiabatic coupler. Since the working principle of these devices is the spatial adiabatic passage, they are robust in front of fluctuations of the geometric parameter values.

3.1 Introduction

A unique feature of the adiabatic passage processes, which consist in the adiabatic following of an eigenvector of a system, is their working robustness against variations of the parameter values. Adiabatic passage processes have been successfully studied in several areas of physics, such as Quantum Optics, Ultracold Atoms, and light propagation in coupled waveguide systems. In Quantum Optics, two techniques have been extensively studied, the so-called stimulated Raman adiabatic passage [34] (STIRAP) and the rapid adiabatic passage [104, 105] (RAP). In both cases, an eigenstate of an atomic system interacting with a specific sequence of laser pulses is modified in time and adiabatically followed, achieving a complete and robust transfer of population between two internal atomic levels of the system. Adiabatic passage processes were later extended to external degrees of freedom in the Ultracold Atoms field [50], where it was proposed to transport single atoms between the most distant traps of a system of three tunneling-coupled potential wells, the so-called spatial adiabatic passage. Subsequently, spatial adiabatic passage processes have also been applied for transport of electrons [70], Bose Einstein condensates (BECs) [72, 73, 74, 75] and holes [55], for state [78] and velocity [106] filtering of neutral atoms and also for the generation of matter wave angular momentum [107]. Spatial adiabatic passage for light propagation

in a system of three total internal reflection (TIR) coupled optical waveguides [43, 82] has been experimentally reported. In this case, a supermode of a triple-waveguide system is adiabatically modified and followed along the propagation direction, achieving a complete light transfer between the outermost waveguides of the system. Furthermore, applications of the light spatial adiabatic passage have been successfully experimentally demonstrated, such as a polychromatic beam splitter [108] and a spectral filter [83].

Light guiding in waveguides has been extensively studied, being TIR waveguides the most technologically developed [81]. However, the introduction of photonic crystals (PhCs) [47, 48, 49] allowed for a new way of light guiding by means of linear defects, consisting in rows with unitary cells of different geometry along PhCs [109, 110, 111, 112], which could be integrated with much smaller sizes than the traditional TIR waveguides. Linear defects allow for light guiding due to the creation of propagation bands within the band gap frequencies. In analogy with the PhCs, phononic crystals (PCs) were introduced [113, 114, 115, 116, 117] in the field of sound waves propagation, leading to numerous new physical phenomena for sound waves such as negative refraction and focusing [118, 119], nondiffractive propagation [120], or angular bandgaps [121], to cite a few. As well, sound guiding in linear defects in PCs has been studied [122, 123, 124, 125, 126, 127, 128], including systems of coupled linear defects [129].

In this chapter, spatial adiabatic passage processes for sound waves are adressed for the first time to the best of our knowledge, leading to the implementation of for instance a coherent multifrequency adiabatic splitter, a phase difference analyzer and a coherent multifrequency adiabatic coupler. In particular, we investigate the sound propagation in systems of two linear defects in sonic crystals (SCs) [45, 46]. SCs are a particular case of PCs that consist of solid scatterers embedded in a fluid host medium. Without loss of generality SCs allow considering the propagation of only longitudinal waves, which constitutes an important simplification. Furthermore, SCs are experimentally relevant since, for example, they allow for measurements inside the crystal [121]. It is important to note that the devices to be discussed here, since they are based on spatial adiabatic passage processes, are robust and do not depend on precise parameter values of the physical system. Moreover, the Cobtained results could be easily extended to light propagation in two coupled PhC linear defects and also to light propagation in two coupled TIR waveguides.

In Section 3.2 we present the considered physical system consisting of two coupled linear defects in a SC, and we will calculate the allowed bands into the bandgap and their corresponding supermodes. We will also distinguish between two different frequency ranges inside the bandgap, one where both a symmetric and an antisymmetric supermodes coexist, and another range where only the antisymmetric supermode is present. Thus, in Section 3.3, for the range in which both supermodes exist, we will study spatial adiabatic passage processes through the couple-mode equations, leading to the implementation of a coherent multifrequency adiabatic splitter, in Subsection 3.3.1, and a phase difference analyzer, in Subsection 3.3.2. Finally, in Section 3.4, we will focus in the frequency range with only the antisymmetric supermode, where we

will design spatial adiabatic passage processes working as a coherent multifrequency adiabatic splitter and as a coupler.

3.2 Physical system

We consider a two-dimensional square lattice SC made of steel cylinders (filling medium) immersed in water (host medium) containing linear defects. The propagation of sonic waves in SCs consisting of two different materials can be described by the following linear equations [120]:

$$\beta \frac{\mathbf{v}}{t} = -\boldsymbol{\nabla} p \tag{3.1a}$$

$$\frac{p}{t} = -B \boldsymbol{\nabla} \cdot \mathbf{v} \tag{3.1b}$$

where $B(\mathbf{r})$ is the bulk modulus, $\beta(\mathbf{r})$ is the density, $p(\mathbf{r}\ t)$ is the pressure field and $\mathbf{v}(\mathbf{r}\ t)$ is the velocity vector field. Considering sound beams with harmonic temporal dependence and that $B(\mathbf{r})$ and $\beta(\mathbf{r})$ are periodic functions with the periodicity of the lattice, equations (3.1) can be solved by means of the plane wave expansion (PWE) method, which gives an eigenvalue problem equation [114, 115, 120]:

$$\sum_{\mathbf{G}'} [\ \ {}^2 b^{-1}_{\mathbf{G}-\mathbf{G}'} - \beta^{-1}_{\mathbf{G}-\mathbf{G}'} (\mathbf{k}+\mathbf{G}) \cdot (\mathbf{k}+\mathbf{G}\ )] p_{\mathbf{k},\mathbf{G}'} = 0 \tag{3.2}$$

where is the angular frequency of the plane waves divided by the sound velocity in the host medium, c_h, $\mathbf{k}$ is a two-dimensional Bloch vector belonging to the irreducible Brillouin zone, $\mathbf{G}$ and $\mathbf{G}$ are vectors of the reciprocal lattice, $p_{\mathbf{k},\mathbf{G}'}$ is the coefficient for the pressure field expanded following the Bloch-Floquet theorem

$$p(\mathbf{r}) = e^{(i\mathbf{k}\cdot\mathbf{r})} \sum_{\mathbf{G}'} p_{\mathbf{k},\mathbf{G}'} e^{(i\mathbf{G}'\cdot\mathbf{r})} \tag{3.3}$$

and $b^{-1}_{\mathbf{G}-\mathbf{G}'}$ and $\beta^{-1}_{\mathbf{G}-\mathbf{G}'}$ are the Fourier coefficients of the inverted relative values of the bulk modulus, $B(\mathbf{r})^{-1} = B_h\ \ B(\mathbf{r})$, and the density, $\beta(\mathbf{r})^{-1} = \beta_h\ \ \beta(\mathbf{r})$, respectively. Here, B_h and β_h are the bulk modulus and the density of the host medium, respectively.

In the case of a SC consisting of only two different materials, the values of the coefficients $b^{-1}_{\bar{\mathbf{G}}}$ and $\beta^{-1}_{\bar{\mathbf{G}}}$, with $\bar{\mathbf{G}} = \mathbf{G} - \mathbf{G}$, can be found by integrating over the filled area (corresponding to steel) inside the two-dimensional unit cell. For $\beta^{-1}_{\bar{\mathbf{G}}}$ one obtains [114, 115, 120]

$$\beta^{-1}_{\bar{\mathbf{G}}} = \begin{cases} \dfrac{1}{A} \displaystyle\int\int \frac{1}{\beta(\mathbf{r})} d\mathbf{r} = \frac{\beta_h}{\beta_c} f + (1-f) & \text{for } \bar{\mathbf{G}} = 0 \qquad (3.4) \\ \dfrac{1}{A} \displaystyle\int\int \frac{e^{(i\bar{\mathbf{G}}\cdot\mathbf{r})}}{\beta(\mathbf{r})} d\mathbf{r} & \text{for } \bar{\mathbf{G}} = 0 \qquad (3.5) \end{cases}$$

where A is the area of the unit cell, f is the filling factor and β_c is the density of the filling material. In the case of a square lattice and a SC formed by cylinders of radius r_0, Eq. (3.5) takes the following form:

$$\beta_{\bar{\mathbf{G}}}^{-1} = \left(\frac{\beta_h}{\beta_c} - 1\right) 2f \frac{J_1(\,\bar{\mathbf{G}}\, r_0)}{\bar{\mathbf{G}}\, r_0} \quad \text{for } \bar{\mathbf{G}} = 0 \tag{3.6}$$

where $J_1(x)$ is the Bessel function of the first kind. Expressions for $b_{\bar{\mathbf{G}}}^{-1}$ are analogous [120].

The eigenvalues of Eq. (3.2) can be numerically obtained and correspond to the frequencies of the allowed propagation bands in the SC. By plotting these frequencies as a function of the $\mathbf{k}$ values it is possible to construct the band diagrams. Once the frequencies are known, by using Eq. (3.3) it is also possible to calculate the the supermodes of the structure, i.e., the pressure field $p(\mathbf{r})$.

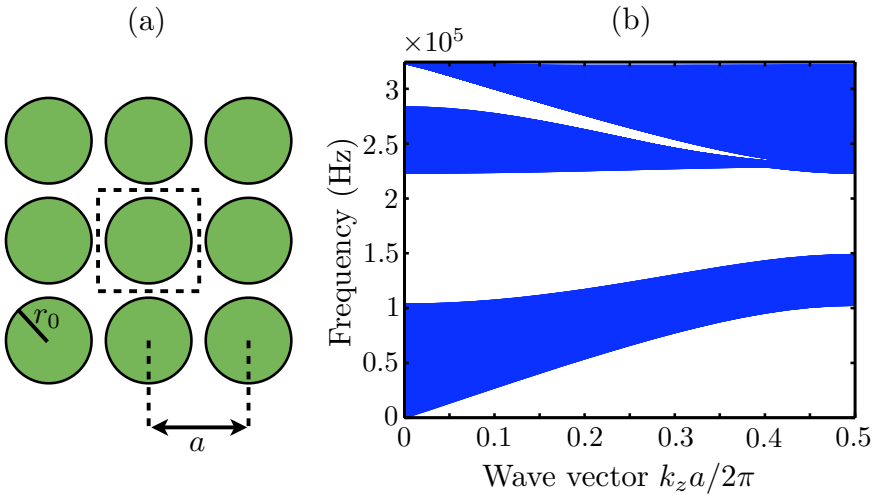

Figure 3.1: (a) Schematic representation of the unit cell. (b) Projected band diagram of the SC without any defect, where a sonic band gap can be observed. The SC considered in this work has a lattice constant of $a = 5\,\text{mm}$ and consists of steel cylinders of radius $r_0 = 2\ 25\,\text{mm}$ ($\beta_c = 7\ 8 \times 10^3\,\text{kg m}^{-3}$ and $B_c = 160 \times 10^9\,\text{N m}^{-2}$) immersed in water ($\beta_h = 10^3\,\text{kg m}^{-3}$, $B_h = 2\ 2 \times 10^9\,\text{N m}^{-2}$). 961 plane waves have been used in the PWE.

To study the control of sound propagation along linear defects (or waveguides) in the SC, it can be considered that sound travels mostly in the direction along the defect. In this situation it is convenient to project the band diagram [49], i.e., for every k_x in the irreducible Brillouin zone, all the solutions that bring the combination of the k_x and any k_y in the irreducible Brillouin zone into a band are represented, where y is perpendicular and x is parallel to the linear defect. The unit cell and the projected

sonic band diagram of the considered SC without linear defects are shown in Fig. 3.1. The existence of a complete band gap can be observed.

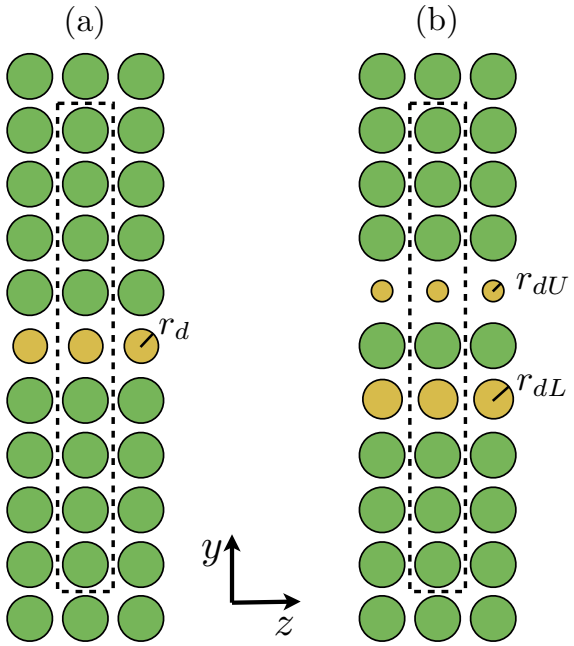

Figure 3.2: Schematic representation of a supercell with (a) one linear defect and (b) two linear defects separated by a single row.

A way to create linear defects in SCs is by adding rows of cylinders with different radii. If we introduce one linear defect composed of cylinders of radius r_d, bands corresponding to the modes of the individual waveguide are obtained into the band gap allowing for sound guiding inside the SC. Similarly, if we introduce two parallel linear defects with radii r_{dU} (for the upper one) and r_{dL} (for the lower one) separated, for example, by one normal row of cylinders, bands corresponding to different symmetric and antisymmetric supermodes of the system appear into the band gap. For the calculation of band diagrams containing linear defects it is necessary to change the unit cell to a supercell, which contains several of the previous unit cells in the y direction, as shown in Fig. 3.2. The PWE method can also be used in this case [128]. However, $b_{\bar{\mathbf{G}}}^{-1}$ and $\beta_{\bar{\mathbf{G}}}^{-1}$ have to be recalculated for the corresponding supercell with Eq. (3.5). For the case of one linear defect in a supercell containing nine cylinders (Fig. 3.2(a)) Eq. (3.5)

becomes:

$$\beta_{\bar{\mathbf{G}}}^{-1} = \left(\frac{\beta_h}{\beta_c} - 1\right) \frac{2\omega}{9a^2} \left[r_d \frac{J_1(\,\bar{\mathbf{G}}\, r_d)}{\bar{\mathbf{G}}} + 2r_0 \frac{J_1(\,\bar{\mathbf{G}}\, r_0)}{\bar{\mathbf{G}}} \sum_{j=1}^{4} \cos(j\bar{G}_y a) \right] \quad \text{for } \bar{\mathbf{G}} = 0 \tag{3.7}$$

On the other hand, for the case of two defects separated by a single row in a supercell containing nine cylinders (Fig. 3.2(b)) Eq. (3.5) reads:

$$\beta_{\bar{\mathbf{G}}}^{-1} = \left(\frac{\beta_h}{\beta_c} - 1\right) \frac{2\omega}{9a^2} \left[r_{dU} \frac{J_1(\,\bar{\mathbf{G}}\, r_{dU})}{\bar{\mathbf{G}}} e^{i\bar{G}_y a} + r_{dL} \frac{J_1(\,\bar{\mathbf{G}}\, r_{dL})}{\bar{\mathbf{G}}} e^{-i\bar{G}_y a} + 2r_0 \frac{J_1(\,\bar{\mathbf{G}}\, r_0)}{\bar{\mathbf{G}}} \left(1 \;\; 2 + \sum_{j=2}^{4} \cos(j\bar{G}_y a) \right) \right] \quad \text{for } \bar{\mathbf{G}} = 0 \tag{3.8}$$

Expressions for $b_{\bar{\mathbf{G}}}^{-1}$ are analogous.

Fig. 3.3 shows the band diagrams for two different supercells, each one with two defects, obtained using the PWE method. Fig. 3.3(a) corresponds to a SC with two equal defects corresponding to the absence of cylinders ($r_{dU} = r_{dL} = 0$), and Fig. 3.3(b) represents the band diagram of a SC with two defects of very different radius, one empty row ($r_{dU} = 0$) and $r_{dL} = 1\,2\,\text{mm}$. In Fig. 3.3 we also represent the supermodes of the system of two parallel linear defects, which have been calculated using Eq. (3.3). The supermodes allow us to distinguish between symmetric bands and antisymmetric bands. In this work we will focus in two of the bands, the symmetric one represented in green color, and the antisymmetric one represented in red color. It is worth to note that in Fig. 3.3(b) there is another band represented in orange color which significantly overlaps in frequencies with the antisymmetric band. This band corresponds to a higher antisymmetric supermode of the system. Because of its antisymmetric transverse profile within the space of one waveguide (see Fig. 3.3(b)), this supermode will not be excited by the sound source which has a symmetric transverse profile. Therefore, we consider that this higher supermode will not play any role in the sound propagation.

In Fig. 3.3 we can also see that when the two defects are equal, both supermodes (symmetric and antisymmetric) spread equally into the two defects. However, when the defects have significant different radii, the symmetric supermode is localized in the linear defect with smallest radius ($r_{dU} = 0$ in the figure) whereas the antisymmetric stays localized in the linear defect with bigger radius ($r_{dL} = 1\,2\,\text{mm}$ in the figure).

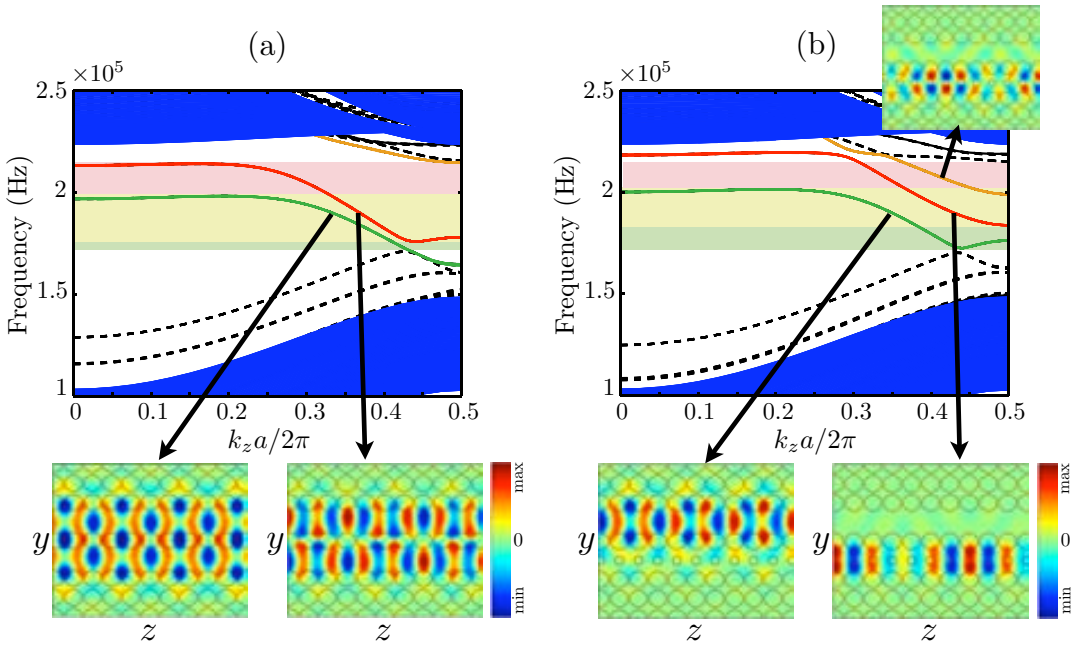

Figure 3.3: Band structures for two linear defects of radii (a) $r_{dU} = r_{dL} = 0$ and (b) $r_{dU} = 0$ and $r_{dL} = 1.2\,\text{mm}$ in a SC with the same parameter values as in Fig. 3.1. In both figures, we show the symmetric, in green, and the antisymmetric, in red, bands that are used for the control of sound propagation. The orange band corresponds to a higher antisymmetric supermode. The supermodes for the symmetric and antisymmetric bands are shown for a frequency $\nu = 1.9 \times 10^5\,\text{Hz}$ by plotting the pressure field. The higher antisymmetric supermode is also shown in (b) for a frequency $\nu = 2.05 \times 10^5\,\text{Hz}$. In (a) and (b) the regions where both the symmetric and antisymmetric supermodes coexist are marked in light yellow, and also where only one of the supermodes exist, in light green for the symmetric and in light red for the antisymmetric.

In general, the transverse amplitude profiles of the supermodes can be modified by changing the difference between the radii sizes: the more different are the radii of two defects the more localized are the supermodes in one of the defects. Thus, if one of the supermodes of the system is excited, either the symmetric or the antisymmetric, by smoothly changing the radii of the linear defects along the propagation direction it is possible to adiabatically follow the initially excited supermode of the system, which, due to the radii modification, will smoothly change its transversal amplitude profile along the propagation direction. This adiabatic following, which corresponds to the so-called spatial adiabatic passage process [50, 70, 72, 73, 74, 75, 55, 43, 82], allows for a control of the sound propagation along linear defects in SCs. If the radius modification is realized not adiabatically enough, sound waves will not be able to

follow the change of the transverse profile of the initially excited supermode along the propagation direction, exciting other supermodes of the system and we would lose the control of sound propagation. It is important to remark that, spatial adiabatic passage processes have the advantage that they are robust in front of variations of the parameter values. In our case, fluctuations in the size of the defects are not critical to perform a spatial adiabatic passage process, only a smooth enough variation of the radii size is needed in order to adiabatically follow the supermode.

In Fig. 3.3 we can also distinguish frequencies where the symmetric and antisymmetric supermodes coexist (light yellow shadow), whereas there are regions where either only the antisymmetric supermode (light red shadow) or only the symmetric (light green shadow) are present. In the following, different spatial adiabatic passage processes will be discussed in order to control the sound propagation for several applications. First, it will be studied the frequency range in which both the symmetric and antisymmetric supermodes coexist along the propagation. Later, it will be checked the case in which only one supermode is allowed.

3.3 Two-supermode case

The propagation of sound along two defects for frequencies where both symmetric and antisymmetric supermodes exist can be approximately described by the coupled-mode equations, as it can be done for TIR waveguides [81] or photonic crystal linear defects [130]. Coupled-mode equations give a straightforward and convenient insight to the study of waves propagation in waveguide systems. For the most general case of two coupled waveguides they can be written as:

$$i\frac{d}{dz}\begin{pmatrix} C_U(z) \\ C_L(z) \end{pmatrix} = \frac{1}{2}\begin{pmatrix} 2k_U(z) & -\Omega_{LU}(z) \\ -\Omega_{UL}(z) & 2k_L(z) \end{pmatrix}\begin{pmatrix} C_U(z) \\ C_L(z) \end{pmatrix} \tag{3.9}$$

where k_U (k_L) is the propagation constant of the individual upper (lower) waveguide, Ω_{UL} (Ω_{LU}) is the coupling coefficient from the upper to the lower (from the lower to the upper) waveguide, and C_U (C_L) represents the amplitude function of the field in the upper (lower) waveguide. For the case of sound, the total pressure field in a system of two coupled sonic waveguides can be expressed by

$$p(y\ z) = \sum_{k=U,L} C_k(z)P_k(y) \tag{3.10}$$

where P_U (P_L) is the mode of only the upper (lower) waveguide. The velocity field can be described similarly.

It is possible to diagonalize Eq. (3.9) in order to obtain the expressions for the symmetric, $P_+(z)$, and antisymmetric, $P_-(z)$, supermodes as a function of the parameters of the individual linear defects:

$$P_+(z) = \begin{pmatrix} \cos\theta & \sqrt{\frac{\Omega_{UL}}{\Omega_{LU}}\sin^2\theta + \cos^2\theta} \\ \sqrt{\frac{\Omega_{UL}}{\Omega_{LU}}}\sin\theta & \sqrt{\frac{\Omega_{UL}}{\Omega_{LU}}\sin^2\theta + \cos^2\theta} \end{pmatrix} \tag{3.11}$$

and

$$P_-(z) = \begin{pmatrix} \sin\theta & \sqrt{\sin^2\theta + \frac{\Omega_{UL}}{\Omega_{LU}}\cos^2\theta} \\ -\sqrt{\frac{\Omega_{UL}}{\Omega_{LU}}}\cos\theta & \sqrt{\sin^2\theta + \frac{\Omega_{UL}}{\Omega_{LU}}\cos^2\theta} \end{pmatrix} \tag{3.12}$$

where the mixing angle θ is defined by

$$\tan 2\theta = \frac{\overline{\Omega_{UL}\Omega_{LU}}}{\Delta k} \tag{3.13}$$

with $\Delta k = k_L - k_U$. The propagation constants of the $P_+(z)$ and $P_-(z)$ supermodes are

$$k_\pm = \frac{k_U + k_L \mp \sqrt{\Omega_{UL}\Omega_{LU} + \Delta k^2}}{2} \tag{3.14}$$

For example, the coupled-mode equations (3.9) properly describe the power oscillations between two equal waveguides characteristic of the directional couplers when incident sound waves are injected into one of the two waveguides [81]. For two equal waveguides we have that $k_U = k_L = k$ and $\Omega_{DU} = \Omega_{UD} = \Omega$, with k and Ω being constant along z. In this case, the symmetric and antisymmetric supermodes are equal to $P_+(z) = (1\ 1)^T \quad \overline{2}$ and $P_-(z) = (1\ -1)^T \quad \overline{2}$ with propagation constants $k_+ = k - \Omega\ 2$ and $k_- = k + \Omega\ 2$, which leads to the well-known coupling-length expression $L_C = \omega \quad k_+ - k_- \ = \omega\ \Omega$. These power oscillations between two waveguides are analogous to the Rabi oscillations between two internal atomic levels. In fact, the coupled-mode equations provide a useful analogy between propagation of waves along two coupled waveguide systems and the time evolution of the population in two-level atomic systems interacting with a laser beam. Additionally, the coupled-mode equations (3.9) allow us to easily confirm that, as we have discussed in Section 3.2, by smoothly changing the radii of the linear defects it is possible to modify and follow the symmetric and antisymmetric supermodes of the system and control the sound propagation. Thus, in order to modify along the propagation direction the P_+ and P_- supermodes obtained from the coupled-mode equations, it is necessary to change the couplings and thus, the mixing angle θ (see Eqs. (3.11) and (3.12)), which depends on the ratio $\overline{\Omega_{UL}\Omega_{LU}}\ \Delta k$, as shown in Eq. (3.13). This ratio, and therefore the supermode transverse profiles, can be changed by modifying the radii size of the defects. Calculating the band diagrams for a single defect with Eq. (3.2), Eq. (3.4) and Eq. (3.6) it is straightforward to check that the value of $\Delta k = k_L - k_U$ increases by making the defect radii progressively different between them. In particular, when the defects are equal, $r_{dU} = r_{dL}$, $\Delta k = 0$. The values of the couplings $\overline{\Omega_{UL}\Omega_{LU}}$ can be found by using Eq. (3.14), since $k_\pm$ can be obtained from the band diagrams with two defects in the SC. Thus, it can be checked that when the radii of the defects are

equal, $\Delta k \ll \overline{\Omega_{UL}\Omega_{LU}}$ and $\theta = \omega\ 4$. Whereas when $r_{dL} - r_{dU} \langle\ 0$, the condition $\Delta k \langle \overline{\Omega_{UL}\Omega_{LU}}$ is fulfilled and θ is equal to either 0 or $\omega\ 2$, depending on the sign of Δk. In this way, by changing the difference between the radii of the linear defects, it is possible to modify the mixing angle θ from either 0 or $\omega\ 2$, corresponding to the symmetric and antisymmetric supermodes localized in only one of the defects, to $\omega\ 4$, where the symmetric and antisymmetric supermodes are equally spread between the two linear defects. This is in agreement with the results shown in Fig. 3.3. Thus, a smooth modification of the difference of radii size will allow for the adiabatic following of either the symmetric or the antisymmetric supermodes of the system leading to a spatial adiabatic passage of sound waves.

This way of modifying and following the symmetric and antisymmetric supermodes presented here resembles the well-known rapid adiabatic passage (RAP) [104, 105] technique presented in Chapter 1, which allows for a coherent control of atomic population in a system of two internal atomic states interacting with a laser pulse of changing frequency.

3.3.1 Coherent multifrequency adiabatic splitter

In this section we will apply the previous ideas coming from the coupled-mode theory to the linear defects in SCs in order to obtain a robust 50% coherent superposition of sound waves at the output of the two linear defects.

To this aim, we need to modify the mixing angle θ from either 0 or $\omega\ 2$ to $\omega\ 4$. For example: if we consider that at the input of the system only the upper linear defect is excited ($C_U = 1$ and $C_L = 0$) and the radii are different so Δk is large compared to $\overline{\Omega_{UL}\Omega_{LU}}$, $\theta = 0$ and only the symmetric supermode $P_+(z_{\text{initial}})$ is excited. Then, if along the z propagation direction the defect radii become progressively more similar (reaching equal values at the output of the system), Δk decreases making $\overline{\Omega_{UL}\Omega_{LU}}$ large compared to Δk, and θ evolves adiabatically from 0 up to $\omega\ 4$. At the output of the system, where the linear defects are equal and $\theta = \omega\ 4$, the followed symmetric state $P_+(z_{final})$ in Eq. (3.12) corresponds to have 50% of the field in each of the two linear defects. Fig. 3.4 schematically represents the evolution of the mixing angle θ and the amplitude in each linear defect. As summarized in table 3.1, there are four possible ways to achieve the 50% power superposition at the output of the two coupled linear defects.

We have designed a structure following the example above described (corresponding to the first row of table 3.1) and we have performed numerical simulations by integrating Eq. (3.1) with the Finite Element method in order to confirm the predictions of the coupled-mode equations for the 50% splitting. Fig. 3.5 shows the results of the numerical simulations of sound waves of frequency $\nu = 1\ 9 \times 10^5$ Hz propagating through the designed structure. We can see how an initial input beam is equally split into the two linear defects at the output. The input linear defect consists of an empty row. The second linear defect consists of cylinders that change their radius from $r_{dL} = 2\ 25$ mm

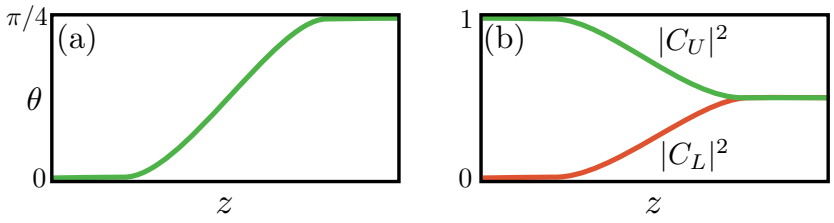

Figure 3.4: Schematic representation of the evolution of (a) the mixing angle θ and (b) the field intensity in the upper and lower defects.

Sign of $\Delta k = k_L - k_U$	**Injection**	**Mixing angle evolution**	**Followed supermode**
+	$C_U = 1$, $C_D = 0$	0 ω 4	$P_+(z)$
+	$C_U = 0$, $C_D = 1$	0 ω 4	$P_-(z)$
−	$C_U = 1$, $C_D = 0$	ω 2 ω 4	$P_-(z)$
−	$C_U = 0$, $C_D = 1$	ω 2 ω 4	$P_+(z)$

Table 3.1: Four possible situations in which at the end of the device the field injected in one of the linear defects ends up in a 50% superposition between the two parallel coupled linear defects.

(the size of the cylinders in the SC) to $r_{dL} = 0$. The two linear defects are separated by one row of the SC. different and we excite the upper one, which has the smallest radius and corresponds to $\theta = 0$ and the symmetric P_+ supermode. Along the propagation, the radius of the cylinders of the lower linear defect decreases smoothly until the linear defect is empty. By doing this, the angle θ and the P_+ supermode adiabatically evolve along the propagation direction until $\theta = \omega$ 4 and the symmetric supermode is equally spread into the two linear defects.

In Fig. 3.6 we plot the normalized power at the two outputs as a function of the frequency. We see that the adiabatic splitting works in a significantly broad range of frequencies from 1 71 $\times$ 10^5 Hz to 1 95 $\times$ 10^5 Hz, in agreement with the available frequencies for the symmetric supermode in the band diagrams for the different points along the propagation, see Fig. 3.3. Thus, this structure constitutes a coherent multi-frequency adiabatic splitter. The splitting works for different frequencies as long as it is possible to follow adiabatically the P_+ supermode. If the supermode is not adiabatically followed, for example because of a too sudden change of the radii of the defect, the symmetric supermode (or even some other higher supermodes) would be excited, limiting the efficiency of the splitting. spatial adiabatic passage it is necessary that the values of Δk and the couplings $\overline{\Omega_{UL}\Omega_{LU}}$ are strong enough with a large enough spatial overlap [43, 82].

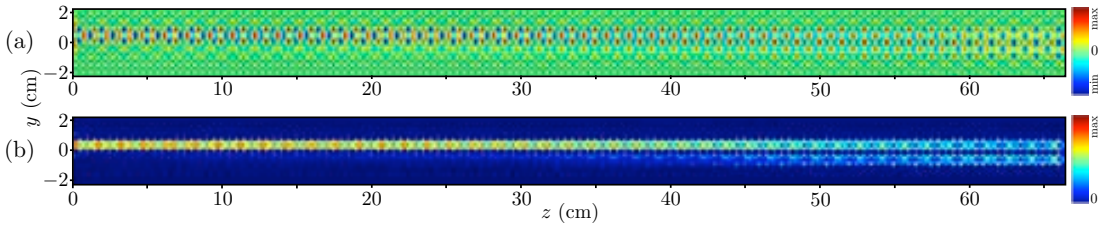

Figure 3.5: Numerical simulations of (a) the pressure field and (b) the total intensity field for sound propagation along the SC with two linear defects acting as a coherent beam splitter structure for a frequency $\nu = 1\ 9{\times}10^5$ Hz. The parameter values of the SC are the same as in Fig. 3.1. The upper linear defect consists of a row empty of cylinders whereas the lower linear defect smoothly changes its radius from $r_{dL} = 2\ 25$ mm to $r_{dL} = 0$.

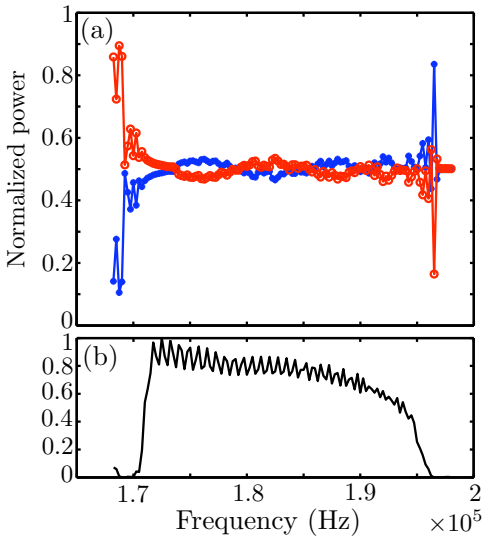

Figure 3.6: (a) Normalized power at the upper (red curve) and lower (blue curve) outputs as a function of the frequency respect to the total power at the output and integrated over the width of each defect (5 mm width for each defect). (b) Normalized total power reaching the outputs relative to the maximum power at the two outputs.

3.3.2 Phase difference analyzer

A structure similar to the one described in Section 3.3.1 can be implemented in order to measure the phase difference between two sound beams. In this case, at the input the two defects are empty of cylinders, being $\theta = \omega\ 4$ and both the symmetric and the antisymmetric supermodes spread equally into the two defects, see Fig. 3.3(a).

Along the propagation direction, the defect radius of the lower linear defect smoothly increases its size up to $r_{dL} = 1\,2\,\text{mm}$, while the upper defect remains without cylinders, $r_{dU} = 0$. Thus, at the output of the system, since the radii of the defects are significantly different, $\Delta k \langle \quad \overline{\Omega_{UL}\Omega_{LU}}$, $\theta = 0$, and the symmetric supermode is localized in the upper waveguide while the antisymmetric one is localized in the lower defect, as shown in Fig. 3.3(b). Now we consider that two sound beam sources are placed at input of the system, each one in front of each linear defect. If the sources are in phase, only the symmetric supermode will be excited, sound waves will follow adiabatically the supermode along the propagation and at the end of the device there will be only sound intensity in the upper output for which $r_{dU} = 0$. On the other hand, if the two sources are in opposite phase, only the antisymmetric supermode will be excited and sound waves will follow it adiabatically ending up into the lower output for which $r_{dL} = 1\,2\,\text{mm}$. In general, one can consider any phase difference between the input sources and the initial field for two sources of equal intensity can be expressed as:

$$_{in} = \frac{1}{\overline{2}} \begin{pmatrix} 1 \\ e^{i\varphi} \end{pmatrix} \tag{3.15}$$

The symmetric and antisymmetric supermodes given by the coupled-mode equations, Eq. (3.11) and Eq. (3.12), at the input where the two defects are equal read:

$$P_+(0) = \frac{1}{\overline{2}} \begin{pmatrix} 1 \\ 1 \end{pmatrix} \tag{3.16}$$

$$P_-(0) = \frac{1}{\overline{2}} \begin{pmatrix} 1 \\ -1 \end{pmatrix} \tag{3.17}$$

Projecting $_{in}$ into the symmetric and antisymmetric supermodes and taking the modulus square it is possible to find the sound intensity that approximately excites each supermode, I_+ and I_-:

$$I_+ = \ P_+(0)^* \quad _{in}\ ^2 = \frac{1}{2}(1 + \cos \quad) \tag{3.18}$$

$$I_- = \ P_-(0)^* \quad _{in}\ ^2 = \frac{1}{2}(1 - \cos \quad) \tag{3.19}$$

Since at the output of the system the symmetric supermode corresponds only to sound intensity in the upper linear defect ($I_+ = I_{U,out}$) and the antisymmetric supermode to sound intensity in the lower linear defect ($I_- = I_{L,out}$), it is possible to measure the initial phase difference between two sources of the same power by measuring the intensities at the two linear defect outputs:

$$= \arccos\left(\frac{I_{U,out} - I_{L,out}}{I_{U,out} + I_{L,out}}\right) \tag{3.20}$$

Thus, this structure of linear defects can be used as a phase difference analyzer.

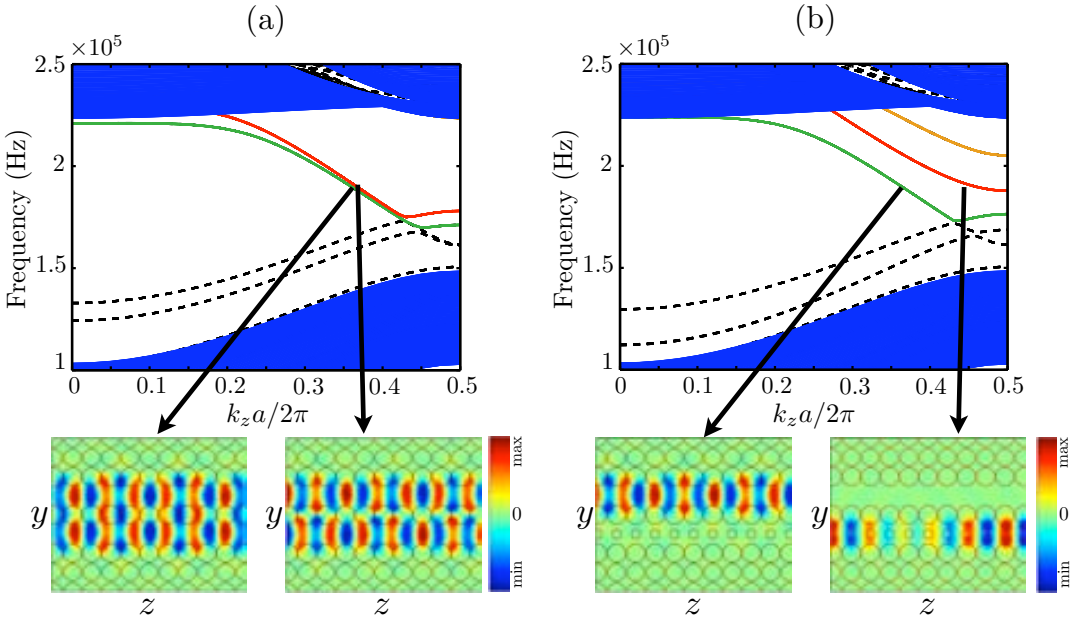

Figure 3.7: Band structures for two linear defects of radii (a) $r_{dU} = r_{dL} = 0$ and (b) $r_{dU} = 0$ and $r_{dL} = 1\,2\,\text{mm}$ including the surrounding raws of radius $r_{dS} = 2\,5\,\text{mm}$. In both figures we plot the symmetric (in green) and the antisymmetric (in red) bands that are used for the control of sound propagation. The supermodes for the symmetric and antisymmetric bands are shown for a frequency $\nu = 1\,9 \times 10^5\,\text{Hz}$. It is possible to see that the sound pressure of these supermodes is more concentrated into the linear defects than in Fig. 3.3.

In order to enhance the working efficiency of the phase difference analyzer, the radius of the cylinders surrounding the linear defects (the cylinders corresponding to the row above the upper linear defect, the row between the linear defects and the row below the lower linear defect) have values smoothly changing from $r_{dS} = 2\,5\,\text{mm}$ to $r_{dS} = 2\,25\,\text{mm}$ (the size of the cylinders in the SC) in the first 10 columns of the SC. In this way it is easier to correctly excite the symmetric and antisymmetric supermodes with the two sound sources, since at the input of the system the sound waves are more concentrated into the waveguides but not in the rest of the SC. In a similar way, the radius of the central cylinders and the cylinders surrounding the linear defects in the last 10 columns of the SC have values smoothly changing from $r_{dS} = 2\,25\,\text{mm}$ to $r_{dS} = 2\,5\,\text{mm}$. By doing this, the supermodes at the output of the system are also more concentrated in the waveguides, which allows for a better identification of the final intensity at each output. The fact that the supermodes are more concentrated when they are surrounded by rows of radius $r_{dS} = 2\,5\,\text{mm}$ has been checked by comparing

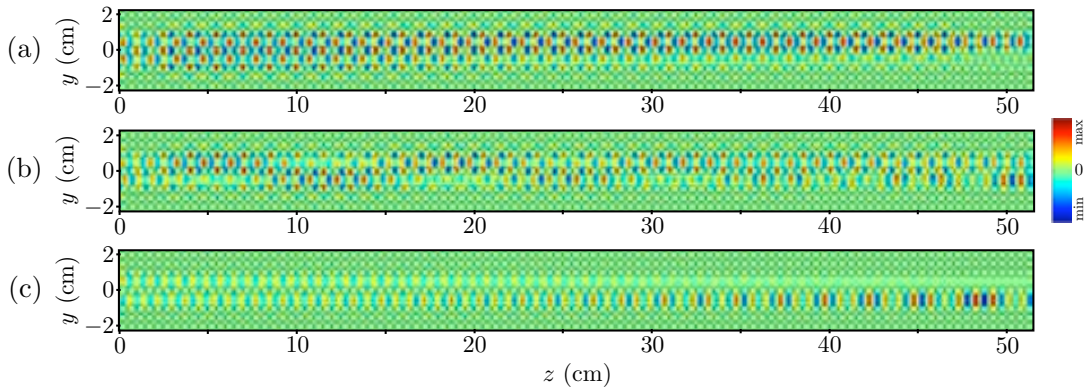

Figure 3.8: Numerical simulations of the sound pressure propagation along the SC with two linear defects acting as a phase difference analyzer structure, with a phase difference between the two input sources of (a) $= 0$, (b) $= \omega$ 2 and (c) $= \omega$ for a frequency $\nu = 1\,9 \times 10^5$ Hz. The parameter values for the SC are the same as in Fig. 3.1. The upper linear defect consists of a row empty of cylinders whereas the lower linear defect smoothly changes its radius from $r_{dL} = 0$ to $r_{dL} = 1\,2$ mm. The first 10 columns surrounding the linear defects have radii changing from $r_{dS} = 2\,5$ mm to $r_{dS} = 2\,25$ mm and vice-versa for the last 10 surrounding columns.

the band diagrams and the symmetric and the antisymmetric supermodes obtained with these extra thicker rows surrounding the linear defects in plotted Fig. 3.7 with the diagrams and supermodes shown in Fig. 3.3. These new band diagrams have been determined by considering the surrounding rows as new linear defects of radius r_{dS} and recalculating Eq. (3.5):

$$\begin{aligned}\beta_{\bar{\mathbf{G}}}^{-1} = &\left(\frac{\beta_h}{\beta_c} - 1\right)\frac{2\omega}{9a^2} \\ &\left[r_{dU}\frac{J_1(\,\bar{\mathbf{G}}\,r_{dU})}{\bar{\mathbf{G}}}e^{i\bar{G}_y a} + r_{dL}\frac{J_1(\,\bar{\mathbf{G}}\,r_{dL})}{\bar{\mathbf{G}}}e^{-i\bar{G}_y a} + \right. \\ &2r_{dS}\frac{J_1(\,\bar{\mathbf{G}}\,r_{dS})}{\bar{\mathbf{G}}}\left(1\;\;2 + \cos(2\bar{G}_y a)\right) + \\ &\left. 2r_0\frac{J_1(\,\bar{\mathbf{G}}\,r_0)}{\bar{\mathbf{G}}}\sum_{j=3}^{4}\cos(j\bar{G}_y a)\right] \\ &\text{for } \bar{\mathbf{G}} = 0\end{aligned} \tag{3.21}$$

The expressions for $b_{\bar{\mathbf{G}}}^{-1}$ can be analogously calculated.

Fig. 3.8 shows the results for the sound propagation obtained by numerical integrating Eq. (3.1) using the Finite Element method. We can observe sound pressure

waves of frequency $\nu = 1\ 9 \times 10^5$ Hz propagating along the designed structure for three different values of phase difference between the input sources: 0, ω 2 and ω. We can clearly see that the intensity at the output depends on the phase difference and that for $= 0$ ($= \omega$ 2) only the symmetric (antisymmetric) supermode is excited and followed, while for $= \omega$ 4 both supermodes are equally excited and followed. Fig. 3.9(a) shows the dependence of the final intensity in each waveguide on the phase difference, which follow the expected behavior (Eq. (3.18) and Eq. (3.19)). Thus, it is possible to calculate the measured phase difference using Eq. (3.20) as a function of the known phase difference introduced between the sources (Fig. 3.9)(b). The results from the numerical simulations are in good agreement with the analytical ones. Small discrepancies arise only close to 0 and ω phase differences. This is due to the impossibility to completely decouple the two linear defects at the input and the output of the system. Nevertheless, a proper calibration of the device would allow for the assignment of a real value of the phase difference to every measured value.

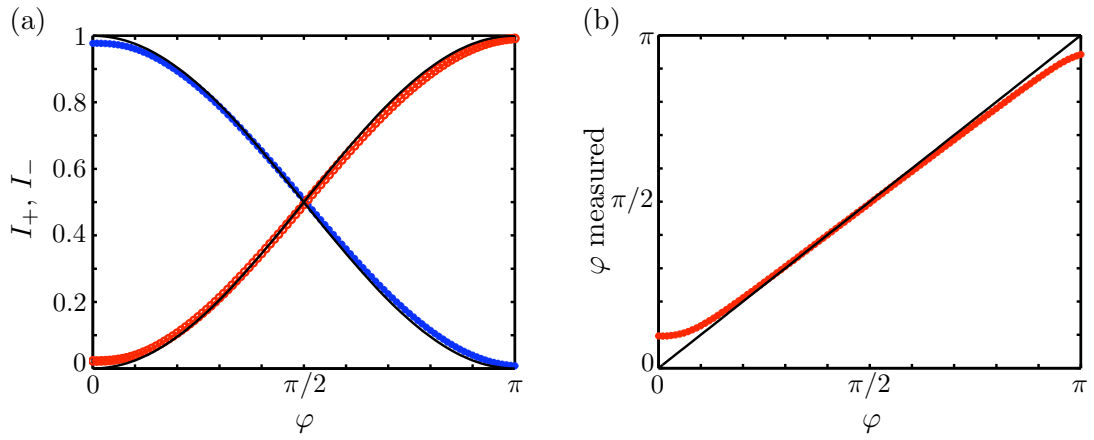

Figure 3.9: (a) Intensity in each waveguide output as a function of the phase difference between the input sources, in blue the upper output and in red the lower output. The results follow those expected from Eq. (3.18) and Eq. (3.19), represented in black. (b) In red color is represented the measured phase difference using Eq. (3.20) as a function of the known phase difference between the sources. The black line corresponds to the ideal measurement given by Eq. (3.20).

The results shown above are for a frequency $\nu = 1\ 9 \times 10^5$ Hz, which is approximately in the middle of the frequency range where both symmetric and antisymmetric supermodes coexist, see the yellow-shadowed area in Fig. 3.3. For this reason, both supermodes are excited with similar intensities. However, for other frequencies surrounding that frequency, one of the supermodes will be excited with slightly more intensity than the other one. Nevertheless, the system can still be used for the measurement of the phase difference bewteen two beams by adjusting the normalization in

Eq. (3.16) and Eq. (3.17), and also calibrating the obtained outputs.

3.4 One-supermode case

Up to now we have studied sound propagation in two parallel linear defects for frequencies in which both symmetric and antisymmetric supermodes exist. However, from Fig. 3.3(a) and (b) it is clear that there are frequencies in which only one of the supermodes can propagate. In particular, marked with a red shadow in Fig. 3.3, there is a quite broad range of frequencies where only the antisymmetric supermode exists. For these frequencies it is not possible to use the coupled-mode theory since only one supermode is available. However, it is still possible to adiabatically follow the antisymmetric supermode of the system in case of smoothly modifying the radius size of the defects along the propagation direction. In fact, the absence of the symmetric supermode allows to relax the smoothness condition for the change in radii size of the linear defects along the propagation direction. Therefore, in this range of frequencies it is possible to design much shorter SC structures for applications that only require the following of a single supermode.

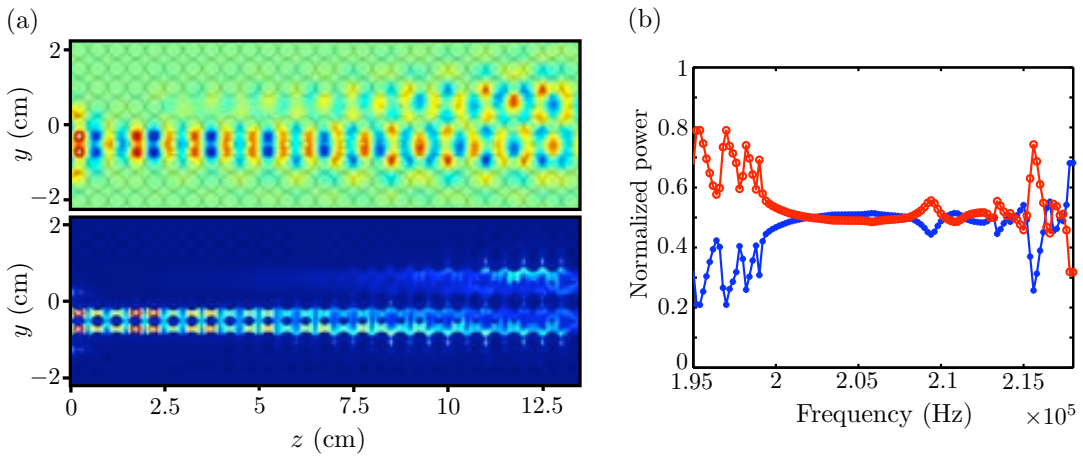

Figure 3.10: (a) Numerical simulations of the sound propagation with a frequency $\nu = 2\,08 \times 10^5$ Hz along the SC with two linear defects for the coherent beam splitter structure, for the pressure field (upper plot) and the total intensity field (lower plot). (b) Normalized power at the upper (red curve) and lower (blue curve) outputs as a function of the frequency respect to the total power at the output and integrated over the width of each defect.

This is the case of the coherent multifrequency adiabatic splitter, where by designing a structure with two linear defects starting with very different radii of the defects, $r_{dL} = 1\,5$ mm and $r_{dU} = 0$, and ending with the defects of the same size, $r_{dL} = r_{dU} = 0\,5$ mm, it is possible to modify the transverse profile antisymmetric mode

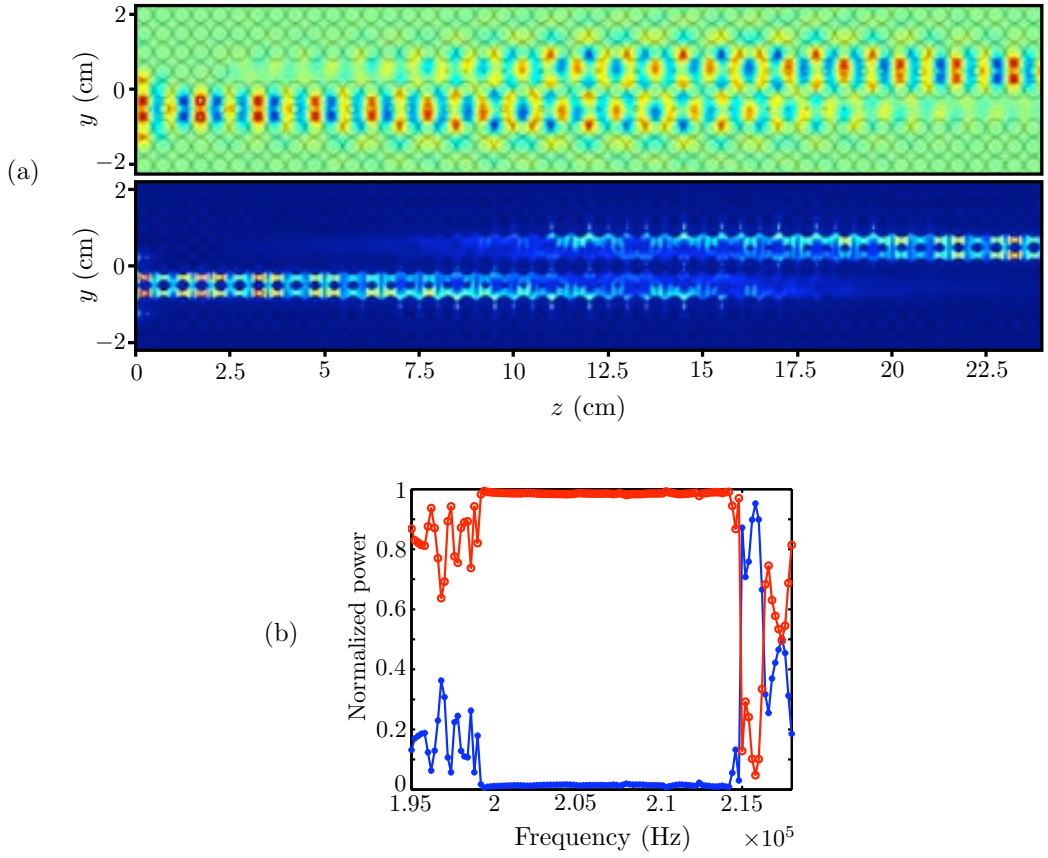

Figure 3.11: (a) Numerical simulations of the sound propagation with a frequency $\nu = 2\ 08 \times 10^5$ Hz along the SC with two linear defects for the robust complete transfer structure, for the pressure field (upper plot) and the total intensity field (lower plot). (b) Normalized power at the upper (red curve) and lower (blue curve) outputs as a function of the frequency respect to the total power at the output and integrated over the width of each defect.

from being very localized in one of the defects to equally spread in the two linear defects. In Fig. 3.10(a) we show the sound pressure propagation in a designed structure for a coherent multifrequency adiabatic splitter when only the antisymmetric mode is available. Additionally, Fig. 3.10(b) plots the normalized power at the upper and lower outputs as a function of the frequency with respect to the total power. We can see that frequencies from 2×10^5 Hz to $2\ 13 \times 10^5$ Hz there is a 50% splitting of the sound intensity, which is the range in which only the antisymmetric supermode is present. Although the results here show a narrower range of working frequencies and a bit higher

oscillations of the total power reaching the output as compared to the one presented in Section 3.3.1, the structure can be significantly shortened (approximately in 5 times respect to the one in Section 3.3.1).

Additionally, given the short length of the splitter, it is possible to design a structure made of two of them, one after the other, with the second one rotated by 180 degrees with respect to the first one. By doing this, sound waves initially in one of the linear defects are completely transferred to the other linear defect by adiabatically following the antisymmetric supermode (see Fig. 3.11(a)). Fig. 3.11(b) shows the range of frequencies in which the complete transfer works efficiently, which as expected coincides with the case of the one-supermode splitter.

3.5 Conclusions

In this chapter we have demonstrated for the first time the possibility to apply spatial adiabatic passage processes to the field of sound waves propagation. Sonic crystals with two linear defects that change their geometry along the propagation direction are designed in order that the sound waves adiabatically follow a supermode of the system. Two different frequency ranges within the band gap are studied. On the one hand, a frequency range in which both a symmetric and an antisymmetric supermode of the system coexist. For this frequency range, two structures have been designed working as a coherent multifrequency adiabatic splitter and as as a phase difference analyzer. On the other hand, a range of frequencies where only the antisymmetric supermode exists is also present. This allows for a reduction in length of the designed structures since transitions to any other supermode are strongly suppressed. A coherent multifrequency adiabatic splitter and a coupler have been designed for this range of frequencies. It is important to note that since these applications are based on spatial adiabatic passage processes, they are robust and do not depend on specific parameter values of the physical system.

4

Spatial adiabatic passage of single cold atoms in waveguide potentials

In this chapter we introduce a coherent technique to inject, extract, and velocity filter neutral atoms in a ring trap coupled via tunneling to two additional waveguides [106]. The proposed technique is based on the spatial adiabatic passage of cold atoms in waveguide potentials: by adiabatically following the transverse spatial dark state, an efficient and robust velocity dependent atomic population transfer between the ring and the input/output waveguides is achieved. We derive explicit conditions for the spatial adiabatic passage that depend on the atomic velocity along the input waveguide as well as on the initial population distribution among the transverse vibrational states. The validity of our proposal has been checked by numerical integration of the corresponding two-dimensional Schrodinger equation with state-of-the-art parameter values for ^{87}Rb atoms and an optical dipole ring trap.

4.1 Introduction

Recent advances in the preparation and manipulation of ultra-cold neutral atoms have enabled a large number of high precision applications in different disciplines such as Atom Optics, Quantum Metrology, Quantum Computation, and Quantum Simulation [131]. Neutral atoms can be trapped in a large variety of potential geometries, among which ring traps present some unique features, such as possessing periodic boundary conditions, that make them ideal candidates to investigate quantum phase transitions [132], matter wave Sagnac interferometry [133], stability of persistent currents and superconducting quantum interference devices [134, 135, 136, 137, 138, 139, 140, 141], propagation of matter wave solitons and vortices [142], cold collisions [143], or artificial electromagnetism [144, 145]. Bright optical (attractive) ring traps for neutral atoms have been experimentally reported with far-detuned optical dipole beams propagating through annular microlenses [146, 147], with a combination of TOP traps and Gaussian

beams [148], with Laguerre Gauss (LG) modes [149, 150, 141], and by means of spatial and acousto-optic modulators [151], while dark (repulsive) optical rings have been realized by an appropriate superposition of Laguerre Gauss laser modes [150] and by means of the dark Poggendorff ring of conical refraction [152].

In fact, one can foresee ring traps for cold atoms in low-energy physics to play a similar role as circular accelerators and storage rings in high-energy physics. Thus, as it was in the past for its high-energy physics counterpart, to seek for efficient methods to inject, filter, store, decelerate, accelerate, and extract cold neutral atoms into and from ring traps is a focus of present interest. In this chapter, we discuss a coherent method for injecting neutral atoms into, extracting them from, and velocity filtering them in a ring trap, which is based on the spatial adiabatic passage technique for cold atoms in dipolar waveguides [50, 51]. As it has been explained in Chapter 1, the spatial adiabatic passage technique here discussed is the matter wave analog [50, 51] of the stimulated Raman adiabatic passage (STIRAP) technique [34] and has been previously proposed for efficiently transporting single atoms [50, 51, 52, 53, 54, 55] and Bose Einstein condensates [72, 73] between the two extreme traps of a triple-well potential, as well as for quantum tomography [78]. Furthermore, as it has been presented in Chapter 2, the spatial adiabatic passage for light propagating in a system of three coupled optical waveguides [43, 82] and a spatial adiabatic passage-based spectral filtering device [83] have been recently experimentally reported.

4.2 Physical system

The physical system under consideration consists of a ring trap and two optical dipole waveguides coupled via tunneling in the three configurations shown in Fig. 4.1(a). In each case, the two waveguides coupled to the ring can be switched on or off at will by simply turning on or off the laser field that generates them. As a consequence, injection, extraction and velocity filtering of neutral atoms can be applied selectively when needed. The technique consists of adiabatically following a particular energy eigenstate of the system, the so-called transverse spatial dark state. Depending on the atomic velocity, an efficient and robust transfer of atoms between the ring and the outermost waveguide or vice versa takes place, with its performance surpassing the case of simply spatially overlapping the ring and the input/output waveguides [153].

As a first configuration, we study the injection of a single cold neutral atom of mass m with a velocity v into the ring trap by modeling the geometry of the physical system as a two-dimensional (2D) optical potential formed by three coupled dipole waveguides, see Fig. 4.1(b), with the ring and input traps being described as a segmented circular waveguide. The dynamics is governed by the 2D Schrodinger equation:

$$i \frac{\partial}{\partial t} (x\ y) = \left[-\frac{^2}{2m} \ ^2 + V(x\ y) \right] (x\ y) \tag{4.1}$$

where ^{2} is the 2D Laplace operator and $V(x\ y)$ is the waveguides trapping potential.

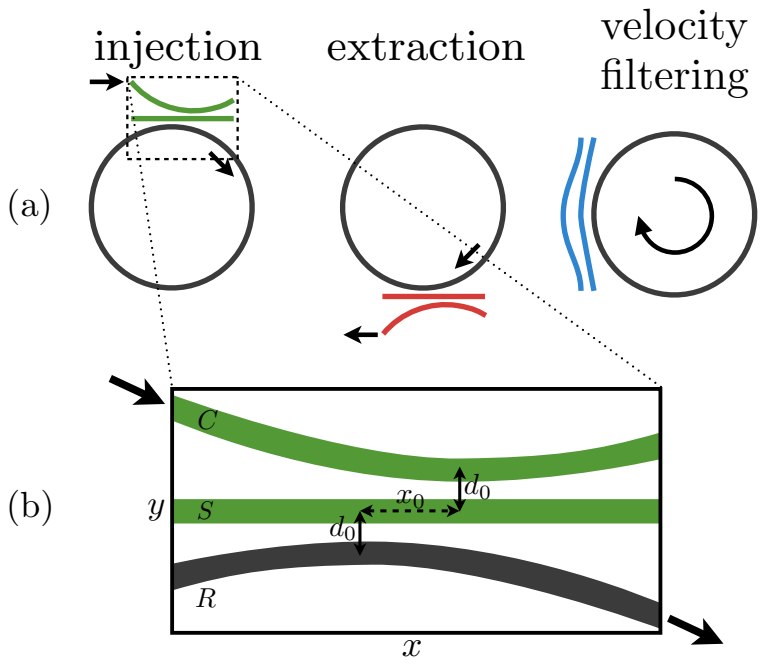

Figure 4.1: (a) Schematic representation of the physical system consisting of a ring trap and two dipole waveguides for injecting neutral atoms into, extracting them from, and velocity filtering them in the ring. (b) Potential geometry for the injection protocol where the two dipole waveguides and part of the ring are modeled as three coupled waveguides. The input (curved) waveguide and the ring waveguide are denoted by C and R, respectively, and correspond to two circularly bent waveguides, while the central straight waveguide is denoted by S. The distance d_0 accounts for the minimum y separation between adjacent waveguides while x_0 gives the x distance between the two positions of mimimum separation.

The transverse confinement for each waveguide is modeled by a harmonic potential of identical ground state width $\alpha \equiv \sqrt{\quad (m \quad)}$, with being the transverse trapping frequency. Truncated harmonic potentials are usually considered in the literature [50, 51] since they allow for the analytical derivation of the tunneling rates. Gaussian or Posch Teller potentials describe more accurately the experimental trapping potentials but they lead to qualitatively similar results [78].

The geometry of each waveguide depends parametrically on x through the variation of the corresponding waveguide center position $y_i = y_i(x)$ with $i = C\ S\ R$ labeling the curved, straight, and ring waveguides, respectively (Fig. 4.1(b)). Thus, the triple waveguide potential can be written as truncated harmonic potentials:

$$V(x\ \ y) = \min_{i=C,S,R} \left[(y - y_i(x))^2 \quad 2\alpha_i^2(x) \right] \tag{4.2}$$

where $\alpha_i^2(x)\ \ \alpha^2 \approx 1 + \quad y_i(x) \quad x\ ^2$, with α_i being the width in the transverse y direction of the vibrational ground state of the i-th waveguide. As a simplification, considering that the y-separation between the waveguides slowly varies along the x-axis, i.e., $\quad y_i(x) \quad x \approx 0$, the velocity of the atom along any of the waveguides can be approximated as $v \approx v_x$. Thus, the motion of an atom with longitudinal velocity v_x can be decoupled from the vibrational motion in the transverse direction. In this way, the system is effectively reduced in the y-direction to a one-dimensional (1D) triple well potential of identical widths with the tunneling rates depending on the separation between the waveguides that, in the atom s own reference frame, are varied in time according to $y_i(x = v_x t)$.

4.3 Velocity filtering mechanism

Assuming that the energy separation between the different vibrational states of each transverse harmonic potential is large enough to avoid crossed tunneling among different vibrational states and that there is no significant coupling between the two outermost waveguides, the transverse Hamiltonian $H \quad$ of the system can be approximated to $H \quad = H_0 \oplus H_1 \oplus \cdots \oplus H_n \oplus \qquad$ with:

$$H_n = \frac{}{2} \begin{pmatrix} 0 & -J_n^{CS}(x) & 0 \\ -J_n^{CS}(x) & 0 & -J_n^{SR}(x) \\ 0 & -J_n^{SR}(x) & 0 \end{pmatrix} \tag{4.3}$$

where J_n^{ij} is the tunneling rate between the n vibrational states of two adjacent waveguides i and j.

After diagonalizing each Hamiltonian H_n, a set of three transverse energy eigenstates for each n is obtained. One of them involves only the vibrational states of the two extreme waveguides and is known as the transverse spatial dark state [50, 51]:

$$D_n(\theta_n)\ \ = \cos\theta_n\ n\ _C - \sin\theta_n\ n\ _R \tag{4.4}$$

where θ_n is defined as $\tan\theta_n \equiv J_n^{CS}\ \ J_n^{SR}$. For a given n, a spatial adiabatic passage of a neutral atom between the two most separated waveguides is achieved by adiabatically following the spatial dark state. This transfer process implies a smooth spatial variation of the tunneling rates such that θ_n slowly changes from 0 to $\omega\ 2$. In the protocol for injecting the atom from the input waveguide C to the ring R, the appropriate tunneling rates variation can be achieved if the two initially empty waveguides, S and R, are approached and separated first along x and, with an appropriate spatial delay x_0, the C and S waveguides are approached and separated (Fig. 4.1(b)).

Considering identical transverse harmonic potentials, for a given n, the maximum tunneling rate between the C and the S, and between the S and the R waveguides will be equal, $J_n^{CS}(-x_0\ \ 2) = J_n^{SR}(x_0\ \ 2)\ (\equiv J_n^{\max})$, corresponding to a separation d_0 between the two closest waveguides. The `global adiabaticity condition to perform a

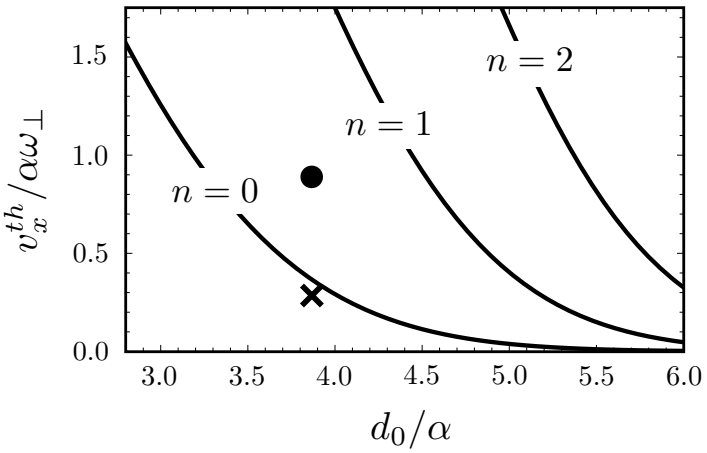

Figure 4.2: Longitudinal threshold velocity v_x^{th} given by Eq. (4.5) for the injection protocol as a function of the minimum waveguides separation d_0 for different transverse vibrational states n. In all cases $x_0 = 50\alpha$ and $A = 10$. The cross and the circle mark the parameters used in the numerical simulations of Fig. 4.3(a) and (b), respectively.

spatial adiabatic passage reads $\overline{2}J_n^{\max}T > A$, where $T = x_0\ v_x$, and A is a dimensionless constant that for optimal parameters takes a value around 10 [34]. Therefore, the spatial adiabatic passage will succeed for longitudinal atomic velocities fulfilling:

$$v_x < v_x^{th} \equiv \quad \overline{2}J_n^{\max}x_0\ A \tag{4.5}$$

Hence, by appropriately engineering the dimension x_0 of the interaction region and the tunneling rates through the minimum separation d_0, it is possible to implement a velocity filter such that atoms with a longitudinal velocity below the threshold velocity given by Eq. (4.5) will be adiabatically transferred into the ring. As the tunneling rates depend on the transverse vibrational state n, the proposed adiabatic transfer technique can also be used for filtering vibrational states [78].

We have applied the recurrence Gram Schmidt orthogonalization [78, 41] and the Holstein Herring methods [154, 155] to obtain analytical expressions for the tunneling rates $J_n^{\max}$, see Appendix A. From these tunneling rates, we have plotted in Fig. 4.2 the longitudinal threshold velocity v_x^{th} as a function of the minimum distance d_0 with $x_0 = 50\alpha$ and $A = 10$. Clearly, since the threshold velocity increases when the tunneling rate increases, higher values for the threshold velocity are achieved at short distances d_0. It is also shown in this figure how the threshold velocity increases for increasing values of n, as expected since the tunneling rate grows with n.

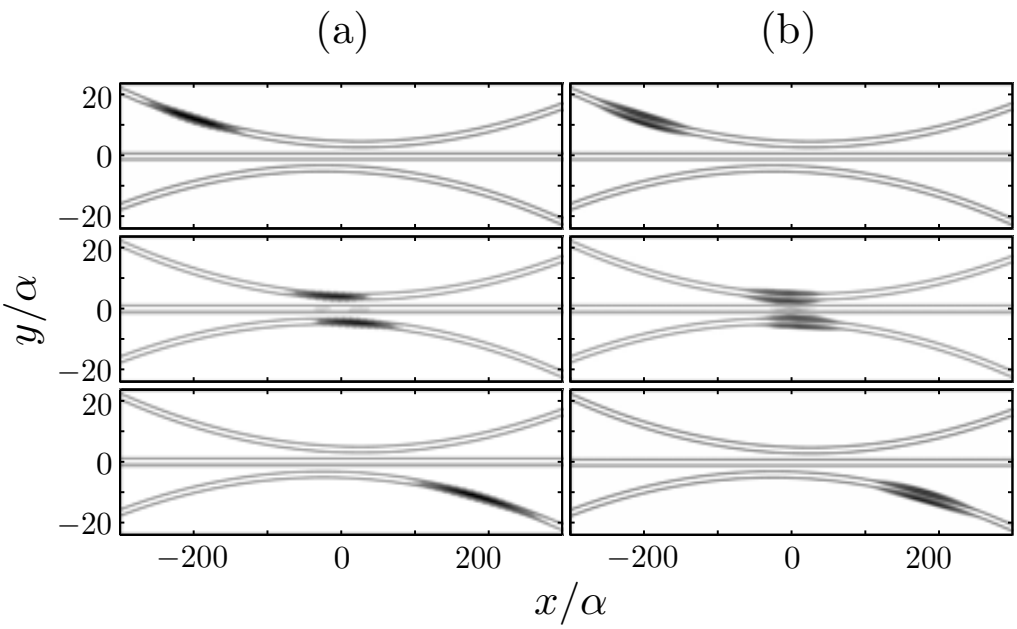

Figure 4.3: 2D numerical simulations showing the atomic probability distribution at three different consecutive times for an input matter wave packet with (a) an initial velocity $v_x = 0\,3\alpha$ at $n = 0$, and (b) an initial velocity $v_x = 0\,9\alpha$ at $n = 1$. In both cases $d_0 = 3\,9\alpha$, $x_0 = 50\alpha$, with the radius of the ring and curved waveguides being $r = 3000\alpha$.

4.4 Numerical results

4.4.1 Injection protocol

Up to here, we have described the main ideas of the proposal by simplifying the initial 2D problem as a transverse 1D triple well potential with position dependent tunneling rates and analyzing the problem in terms of the transverse Hamiltonian. In order to be more realistic, we now investigate the injection protocol by a direct numerical integration of the 2D Schrodinger Eq. (4.1) for ^{87}Rb atoms with the geometry shown in Fig. 4.1(b) and the transverse potential given in Eq. (4.2). Fig. 4.3(a) and (b) show three consecutive snapshots of the atomic probability distribution for the $n = 0$ and $n = 1$ transverse vibrational states, respectively, for the configurations marked in Fig. 4.2 by a cross (for Fig. 4.3(a)) and a dot (for Fig. 4.3(b)). They correspond to input velocities below the respective threshold velocities v_x^{th}, indicating that the global adiabaticity conditions for the spatial adiabatic passage are fulfilled. Thus, in both cases the atom is completely injected into the ring waveguide. Fig. 4.4 shows the numerically calculated region (in white) for which the transfer probability into the ring is higher than 97% for the ground, Fig. 4.4(a), and first excited, Fig. 4.4(b),

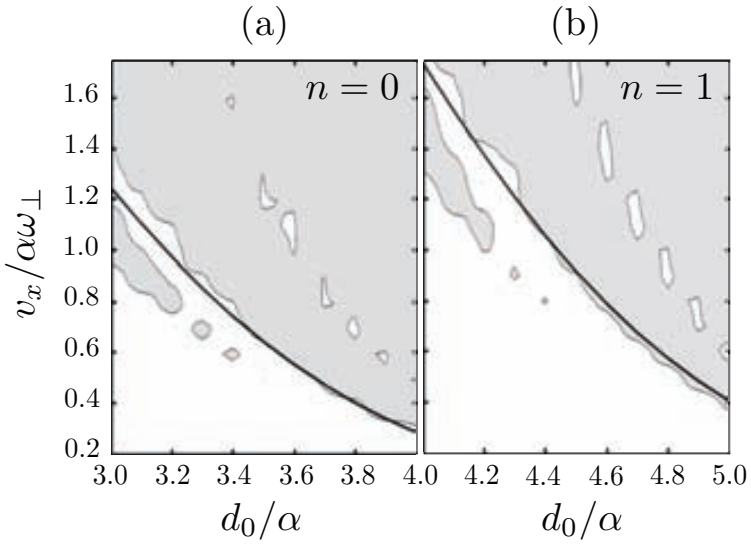

Figure 4.4: Numerically calculated probability for population injection into the ring waveguide as a function of the input velocity v_x and the minimum separation d_0 for an input wave packet at (a) $n = 0$ and (b) $n = 1$. The rest of the parameters are as in Fig. 4.3. White areas correspond to the parameter region for which the transfer probability into the ring is higher than 97%. Solid curves represent the corresponding threshold velocities shown in Fig. 4.2.

transverse vibrational states as a function of the input velocity and the minimum distance between waveguides, in good agreement with the threshold velocity expression derived in Eq. (4.5) (solid lines). In addition, we have numerically confirmed that, for appropriate parameter sets, it is possible to perform filtering of the transverse vibrational states using the fact that the tunneling rates depend on n.

4.4.2 Extraction protocol

Let us now turn to the discussion of the extraction process in the configuration depicted in Fig. 4.1(a) (center). The atoms can be extracted from the ring by applying the same protocol as for injection but simply exchanging the role of the curved and ring waveguides. In an extension, the output waveguide could be part of a secondary ring to be used as an accumulator or storage ring for cold atoms, being repeatedly supplied by the first ring. In addition, it could be possible to choose the parameters for the ring geometry and the injection/extraction protocol in such a way that for an initially broad atomic velocity distribution in the first ring, only atoms with low enough longitudinal velocity, such that they fulfill the adiabaticity condition, were transfered to the secondary ring. Rethermalization during a round trip in the first ring would deliver

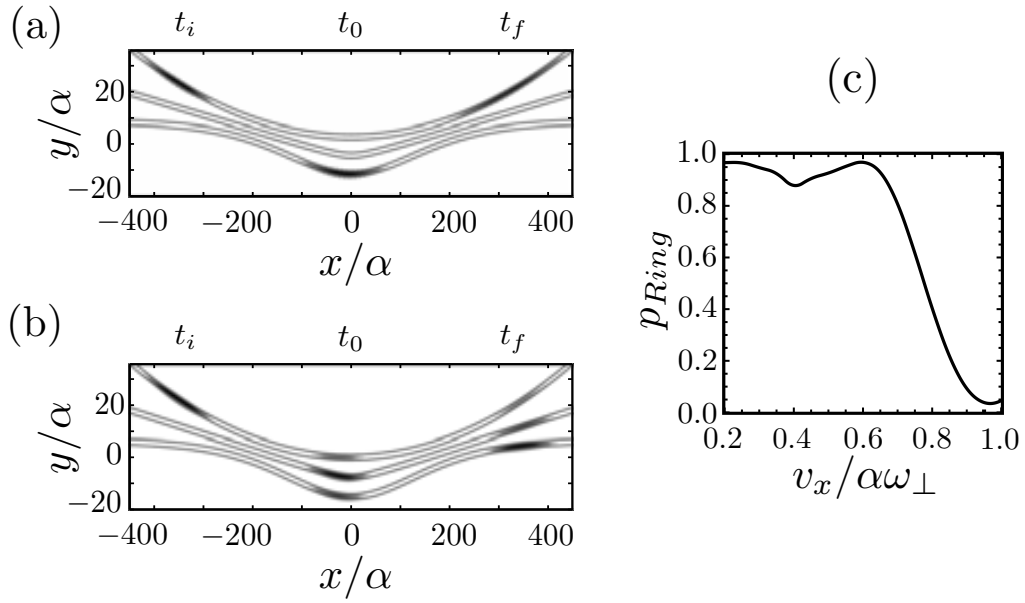

Figure 4.5: Waveguide geometry for a double spatial adiabatic passage process including the atomic probability distribution for three different consecutive times with the initial velocity being (a) $v_x = 0\ 3\alpha$ and (b) $v_x = \alpha$. (c) Final atomic population in the ring as a function of v_x. In all cases $n = 0$.

additional low-velocity atoms into the secondary ring, presenting this secondary ring an improved starting condition for further manipulation of the atoms.

4.4.3 Velocity filtering

We discuss here the velocity filtering configuration shown in Fig. 4.1(a) (right) and Fig. 4.5(a), where atoms propagating along the ring ($r = 3000\alpha$) are coupled to a particular waveguide geometry designed to perform a double spatial adiabatic passage process: the cold neutral atom is transferred from the ring to the external waveguide and comes back into the ring. This process corresponds to the adiabatic following of the transverse spatial dark state in Eq. (4.4), where in this case the θ_n angle slowly changes from 0 to ω 2 (for the first part of the double spatial adiabatic passage) and goes back to 0 (for the second part). Each individual adiabatic passage geometry is characterized by $d_0 = 3\ 9\alpha$ and $x_0 = 50\alpha$. At $x = 0$ the separation between the waveguides is 7α. Fig. 4.5(a) and (b) show the evolution of an input atomic wave packet at different times (t_i, t_0, and t_f) for $v_x = 0\ 3\alpha$ and $v_x = \alpha$, respectively, and $n = 0$ in both cases. In (a), the double spatial adiabatic passage is performed with high efficiency: the atomic wave packet follows the dark state and continues to propagate along the ring after the filtering section. On the contrary, in (b) the input velocity is too high

resulting in the excitation of other eigenstates of the system and the spreading of the atomic wave packet among the three waveguides. Fig. 4.5(c) shows the final population in the ring as a function of the initial longitudinal velocity showing that slow atoms are able to adiabatically follow the spatial dark state and return to the ring trap with high fidelity, while faster atoms that do not fulfill the adiabaticity condition spread among the three waveguides, thus reducing the final population in the ring. One can estimate the expected values of the atomic velocities that will be filtered by means of this geometry for realistic ring geometries [152]: assuming ^{87}Rb atoms in an optical ring potential with radius of ~ 1 mm and trapping frequency $\sim 2\omega \times 1\,\mathrm{kHz}$, we obtain $\alpha \sim 2\,\mathrm{mm\ s}$. Therefore, based on Fig. 4.5(b), it should be possible to selectively remove atoms with velocities higher than $v_x \sim 0\,6\alpha = 1\,2\,\mathrm{mm/s}$.

4.5 Conlusions

We have presented a coherent technique for the injection of neutral atoms into, extracting them out of, and velocity filtering them inside a ring dipole trap. The technique is based on the spatial adiabatic passage of cold atoms in waveguide potentials, which consists in adiabatically following the transverse spatial dark state of the system. Explicit conditions for the spatial adiabatic passage between the waveguides and the ring as a function of the initial longitudinal atomic velocity and on the initial population distribution among the transverse vibrational states have been discussed. In particular, a semi-analytical expression for the threshold longitudinal velocity allowing for a high efficiency of the spatial adiabatic passage has been obtained, which perfectly matches with the full 2D numerical simulations of the Schrodinger equation. Furthermore, numerical simulations demonstrate that fidelities higher than 97% are achieved for both the injection and extraction protocols within a significantly broad ranges of parameter values of the longitudinal atomic velocity and the minimum separation between the waveguides. The performance of our proposal has been checked with state-of-the-art parameter values for ^{87}Rb atoms and an optical dipole ring trap, showing the possibility to filtrate out atoms at velocities higher than $\sim 1\,2\,\mathrm{mm/s}$ from an optical ring potential with radius of ~ 1 mm and trapping frequency $\sim 2\omega \times 1\,\mathrm{kHz}$.

5

Single-atom interferometer based on two-dimensional spatial adiabatic passage

In this chapter we extend the spatial adiabatic passage technique to the two dimensional case by considering a single cold atom in a system of three two-dimensional harmonic traps of the same trapping frequency in a triangular geometry. We show that the transfer of a single atom from the ground state of a harmonic trap to the ground state of the most distant one is successfully achieved in a robust way for a broad range of parameter values. Nevertheless, we find that there is a specific geometrical configuration of the traps for which a crossing of two energy eigenvalues occurs and the transfer of the atom fails, splitting its wavefunction into a coherent superposition between two of the traps. We take advantage of this situation to propose a single-atom interferometer based on spatial adiabatic passage and discuss its performance in terms of the final population distribution among the asymptotic eigenstates of the individual traps. The results have been checked with numerical simulations of the full two-dimensional Schrodinger equation.

5.1 Introduction

Atom interferometers are focus of current research interest due to their suitability to perform high-precision measurements [156, 157, 158, 159, 160, 161, 162, 163]. This is mainly motivated by the small wavelengths associated to matter waves and by the wide range of atomic properties like mass, magnetic moment, and polarizability that makes them suitable to measure fundamental constants, internal forces, accelerations and rotations.

The implementation of an atomic interferometer requires an efficient and robust method to split and recombine the matter wavefunction, i.e., to control the external degrees of freedom of the atom. Tunneling between trapping potentials constitutes a fundamental tool for the preparation and manipulation of single quantum particles

states. However, direct tunneling between two resonant traps leads to Rabi-type oscillations of the atomic population, which are not experimentally easy to controlate since they are very sensitive to small variations of the parameter values of the system [50]. The spatial adiabatic passage technique in a system formed by three traps lying on a straight line has been proposed [50, 70, 51, 74, 54, 55, 69, 78] as the spatial analogue of the stimulated Raman adiabatic passage (STIRAP) technique [34] well known in Quantum Optics. At variance with direct tunneling, spatial adiabatic passage offers a much richer behavior and a more robust performance than direct tunneling approaches since it does not require an accurate control of the system parameters. Three-well interferometry with Bose Einstein condensates (BECs) using an analogue of fractional STIRAP has been recently reported [76]. The spatial adiabatic passage has also been extended to the transport of single atoms along dipolar waveguides [51, 106], to the transport of BECs in triple-well potentials [72, 73] and to the light transfer in coupled optical waveguides [43, 82, 83].

Here, we extend the spatial adiabatic passage technique to a scheme that breaks the effective one-dimensionality that up to know has been assumed from the direct analogy with the STIRAP processes. We consider a single atom in a system of three not aligned two dimensional harmonic traps, which has no analogue in quantum optical systems of internal states. We study the conditions to achieve a complete transfer of the atoms between the ground states of the most distant traps showing that it is possible to perform a robust spatial adiabatic passage process in the considered geometry. We also show that under conditions in which the adiabatic transfer fails, it is possible to implement a novel scheme for atom interferometry.

This chapter is organized as follows. In Section 5.2 we introduce the physical system that will be investigated for the two-dimensional spatial adiabatic passage, and present and diagonalize the Hamiltonian that governs the dynamics of a single atom in the trapping potential. The conditions required to perform two-dimensional spatial adiabatic passage are derived in Section 5.3. In Section 5.4 we discuss the implementation and performance of a matter wave interferometer using a level crossing in the eigenvalue spectrum. Finally, Section 5.5 is devoted to the conclusions.

5.2 Physical system

We consider a system that consists of three two-dimensional harmonic potentials (labeled A, B and C) with equal trapping frequencies ($_A = \ _B = \ _C = \ $). As schematically shown in Fig. 5.1, the three traps are not lying on a straight line but form a triangle, with the trap center positions being $x_A = -d_{AB}\cos\beta$, $y_A = -d_{AB}\sin\beta$, $x_B = y_B = 0$, $x_C = d_{BC}$ and $y_C = 0$ for the A, B and C traps, where d_{AB} and d_{BC} are the distances between A and B traps, and B and C traps, respectively.

In Cartesian coordinates, the A, B and C asymptotic ground states of the traps

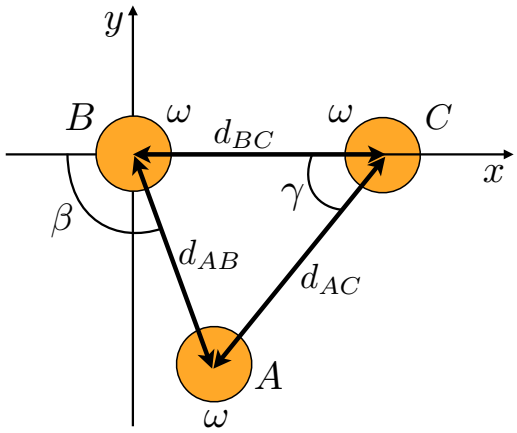

Figure 5.1: Schematic representation of the system of three harmonic traps, A, B and C with equal trapping frequencies. For the parameters definition see the text.

can be written as:

$$_A = \theta_0(x - d_{AB}\cos\beta)\theta_0(y + d_{AB}\sin\beta) \tag{5.1}$$

$$_B = \theta_0(x)\theta_0(y) \tag{5.2}$$

and

$$_C = \theta_0(x - d_{BC})\theta_0(y) \tag{5.3}$$

respectively, where θ_0 is the single-particle ground state eigenfunction of the one-dimensional quantum harmonic oscillator.

In one-dimensional spatial adiabatic passage, three in-line traps are considered such that the coupling between the outermost traps is neglected, i.e., only neighbor coupling is considered. In contrast, in the two-dimensional case we assume that all three traps are directly tunnel-coupled to each other. The tunneling rates between A and B, B and C, and A and C are denoted as J_{AB}, J_{BC} and J_{AC}, respectively. If the dynamics of the system is restricted to the space spanned by $_A(t)$ $_B(t)$ $_C(t)$, the Hamiltonian that governs its evolution reads:

$$H = \frac{}{2}\begin{pmatrix} 0 & -J_{AB} & -J_{AC} \\ -J_{AB} & 0 & -J_{BC} \\ -J_{AC} & -J_{BC} & 0 \end{pmatrix} \tag{5.4}$$

where the couplings depend on the separation between the centers of the harmonic potentials as [50] (see Appendix A):

$$\frac{J_{ij}}{} = \frac{-1 + e^{(\alpha^{-1}d_{ij}/2)^2}\left\{1 + \ \overline{\omega}\alpha^{-1}d_{ij}\left[1 - \mathrm{erf}(\alpha^{-1}d_{ij}\ 2)\right]\ 2\right\}}{\overline{\omega}(e^{(\alpha^{-1}d_{ij})^2/2} - 1)\ (\alpha^{-1}d_{ij})} \tag{5.5}$$

being $i\ j = A\ B\ C$ with $i = j$, $\alpha = \sqrt{\quad (m\ )}$, and m the mass of the single cold atom.

New and richer phenomenology compared to the one-dimensional spatial adiabatic passage case can be found by diagonalizing the Hamiltonian in Eq. (5.4). The energy eigenvalues of Eq. (5.4) are obtained from its characteristic polynomial which is a depressed cubic equation:

$$E^3 + pE + q = 0 \tag{5.6}$$

where:

$$p = -\frac{^2}{4}(J_{AB}^2 + J_{BC}^2 + J_{AC}^2) \tag{5.7}$$

$$q = \frac{^3}{4} J_{AB} J_{BC} J_{AC} \tag{5.8}$$

Since the energy eigenvalues of the Hamiltonian of Eq. (5.4) must be real, the solutions of Eq. (5.6) have to fulfill:

$$4p^2 + 27q^2 \leq 0 \tag{5.9}$$

In this case, the analytic expression of the the energy eigenvalues reads:

$$E_k = 2\sqrt{-\frac{p}{3}} \cos\left[\frac{1}{3}\arccos\left(\frac{3q}{2p}\sqrt{\frac{-3}{p}}\right) + k\frac{2\omega}{3}\right] \tag{5.10}$$

where $k = 1\ 2\ 3$. For $4p^2+27q^2 < 0$ three different energy eigenvalues exist, while $4p^2+27q^2 = 0$ implies that the E_2 and E_3 eigenvalues become degenerated. In particular, the equality $4p^2 + 27q^2 = 0$ is fulfilled if and only if

$$J_{AB} = J_{BC} = J_{AC} \tag{5.11}$$

which would lead to an energy level crossing, $E_2 = E_3$. In our configuration this level crossing occurs for the angle $\beta = 2\omega\ 3$ when all the traps are equally separated. For any other angle β the distances between the traps cannot be all equal simultaneously and therefore, as long as the traps are coupled, the system will have three different energy eigenvalues.

The eigenstates Ψ_k of Eq. (5.4) read:

$$\Psi_k = \frac{1}{N}\left(a_k\ _A + b_k\ _B - c_k\ _C\right) \tag{5.12}$$

with

$$a_k = J_{BC} - \frac{2E_k J_{AC}}{J_{AB}} \tag{5.13}$$

$$b_k = J_{AC} - \frac{2E_k J_{BC}}{J_{AB}} \tag{5.14}$$

$$c_k = J_{AB} - \frac{4E_k^2}{^2 J_{AB}} \tag{5.15}$$

and

$$N = \sqrt{a_k^2 + b_k^2 + c_k^2} \tag{5.16}$$

where $k = 1\ 2\ 3$. For $J_{AC} = 0$, which means $q = E_2 = b_2 = 0$, Eq. (5.12) yields the same expression for the energy eigenstates as in the one-dimensional spatial adiabatic passage case. In particular, one of the eigenstates becomes the so-called spatial dark state, i.e., $\Psi_2 = \cos\theta \ _A - \sin\theta \ _C$ with $\theta = \tan^{-1}(J_{AB} \ J_{BC})$. In this case, the spatial adiabatic passage consists in adiabatically following the spatial dark state from the initial state $_A$ to the final state $_C$ by smoothly varying θ from 0 to ω 2, i.e., by applying the so-called counterintuitive temporal sequence of the tunneling rates.

5.3 Two-dimensional spatial adiabatic passage

In this section we will make use of the previously derived eigenvalues and eigenstates of Hamiltonian (5.4) to investigate up to which extend spatial adiabatic passage works for the two-dimensional case where the coupling between the outermost traps J_{AC} is also present.

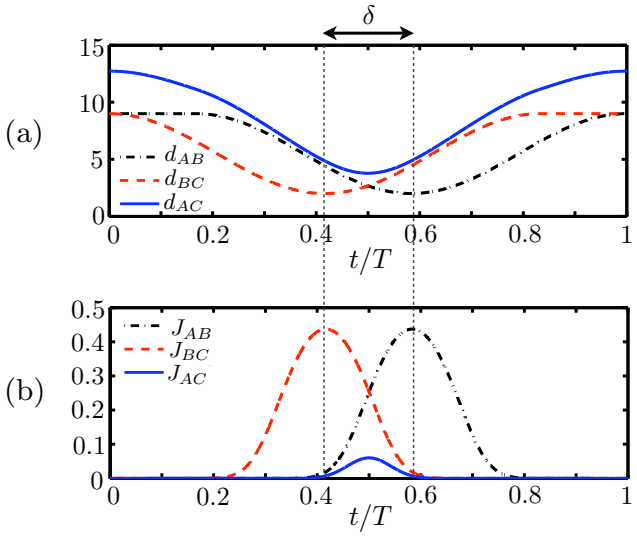

Figure 5.2: Temporal evolution of (a) the distances between traps d_{AB}, d_{BC} and d_{AC}, and (b) the couplings J_{AB}, J_{BC} and J_{AC} during the spatial adiabatic passage process. The parameter values are: $\beta = 0\ 5\omega$ and $\delta = 0\ 2T$, where T is the total time of the process. Coupling rates are given in units of and distances in units of α.

In the two-dimensional case, the counterintuitive temporal sequence of the couplings is applied with the single cold atom initially located in the vibrational ground state of trap A. In our case, with the B trap fixed in the position (0 0), the sequence consists in approaching and separating first C and B traps, and later on and with a certain

temporal delay, approaching and separating A and B traps, keeping the β angle fixed. Note that the distance d_{AC} will depend on the two control distances, d_{AB} and d_{BC} and the angle β, so d_{AC} will not be a free parameter. The couplings as a function of time can be easily calculated through their dependence on the separation between traps, see Eq. (5.5).

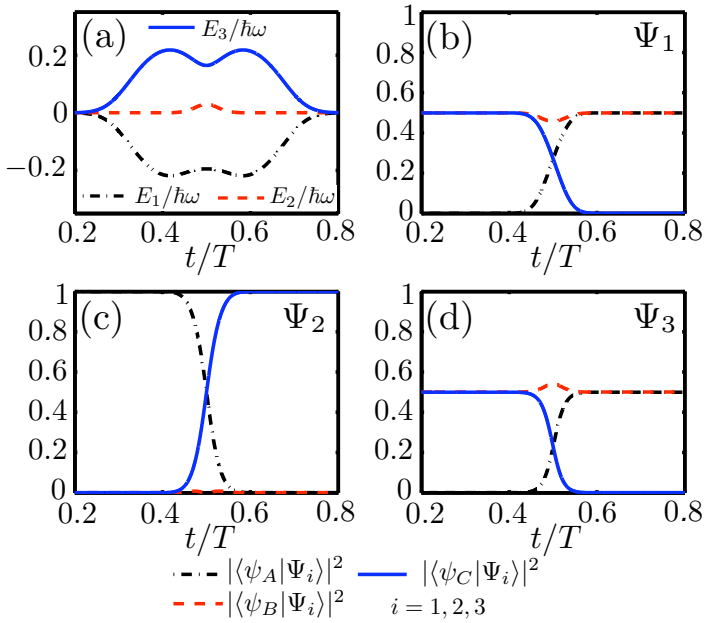

Figure 5.3: Energy eigenvalues as a function of time (a) and temporal evolution of the population of the asymptotic states of the traps $_A$, $_B$, and $_C$ for the three eigenstates of the system Ψ_1 (b), Ψ_2 (c), and Ψ_3 (d). Parameter values as in Fig. 5.2 and energy given in units of .

Fig. 5.2 shows an example of the temporal evolution of the distances between traps and the corresponding coupling rates for the counterintuitive sequence of spatial adiabatic passage. For this temporal evolution of the couplings, Fig. 5.3 shows the corresponding energy eigenvalues as well as the population of each asymptotic level of the individual traps for the three eigenstates of the system. From Eq. (5.12) and the example in Fig. 5.3 it is possible to observe that, when the spatial adiabatic passage sequence is applied, the eigenstate Ψ_2 involves initially only the trap A. Thus, since the atom is initially located in the A trap, the system is in the state $(t = 0) = \Psi_2(t = 0) = {}_A$. If the sequence of approaching and separating the traps is performed adiabatically [34], the system will be able to follow the eigenstate Ψ_2 during the whole process. At the end of the sequence (at a total time T), $(t = T) = \Psi_2(t = T) = {}_C$. Therefore, by applying a counterintuitive coupling sequence the single atom is completely transferred from A to C traps. This is true for a range of angles from $\beta = 0$ (the one-dimensional

spatial adiabatic case) to $\beta < \beta_{th} = 2\omega\ 3$. However, for $\beta = \beta_{th}$ there is a level crossing between Ψ_2 and Ψ_3 and it is no longer possible to adiabatically follow the energy eigenstate Ψ_2. For very large angles, $\beta > \beta_{th}$, the coupling J_{AC} becomes much more intense than the other two couplings and any eigenstate of the system allows for the complete transfer from A to C.

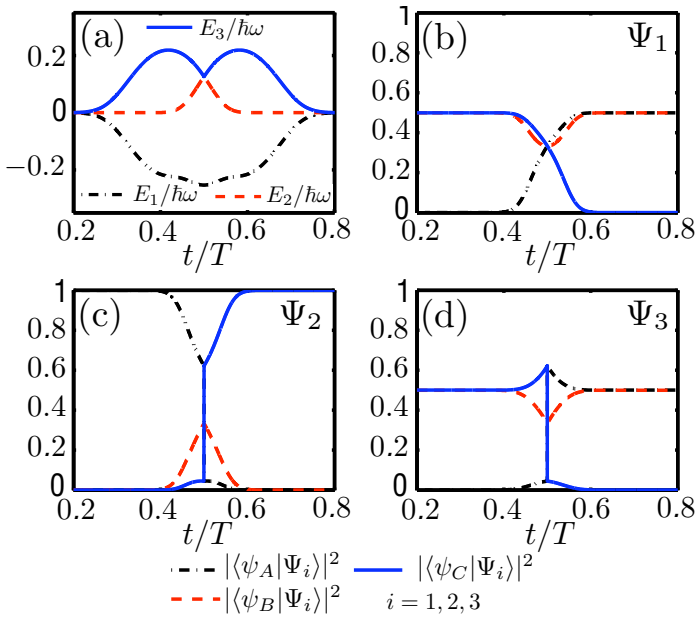

Figure 5.4: Energy eigenvalues as a function of time (a), and temporal evolution of the population of each asymptotic states of the traps $_A$, $_B$, and $_C$ for the three eigenstates of the system Ψ_1 (b), Ψ_2 (c), and Ψ_3 (d) for d_{AB} and d_{BC} as in Fig. 5.2 but with $\beta = 2\omega\ 3$. Energy given in units of .

Let us now investigate in detail the particular case for which there is an energy level crossing. Fig. 5.4 shows the evolution of the energy eigenvalues for the same temporal variation of the distances d_{AB} and d_{BC} as in Fig. 5.2 but with $\beta = \beta_{th}$, as well as the population of each asymptotic level for the three eigenstates of the system. It is clearly shown in Fig. 5.4(a) that the two energy eigenstates Ψ_2 and Ψ_3 cross at a certain time during the dynamics eliminating the possibility to adiabatically follow state Ψ_2. Instead, the system would be transferred from state Ψ_2 to Ψ_3 which at the end of the process will be a superposition of the atom being in trap A and trap B with equal probability, as it can be seen in Fig. 5.4(d).

Up to know, we have discussed two-dimensional spatial adiabatic passage restricting the dynamics to the space spanned by the three asymptotic states of the individual traps. In the following we will check the validity of this simplified model by numerically

integrating the 2D Schrodinger equation, which reads:

$$i \ \frac{}{t} \ (x \ y) = \left[-\frac{^2}{2m} \ ^2 + V \ (x \ y) \right] \ (x \ y) \tag{5.17}$$

where ^{2} is the 2D Laplace operator and $V(x \ y)$ is the trapping potential, which we assume to be constructed from truncated harmonic oscillator potentials

$$V(x \ y) = \min_{i=A,B,C} \left\{ \frac{1}{2} m \ _i^2 \left[(x - x_i)^2 + (y - y_i)^2 \right] \right\} \tag{5.18}$$

Here $(x_i \ y_i)$ with $i = A \ B \ C$ are the positions of the individual trap centers, and $_A = \ _B = \ _C = \ .$

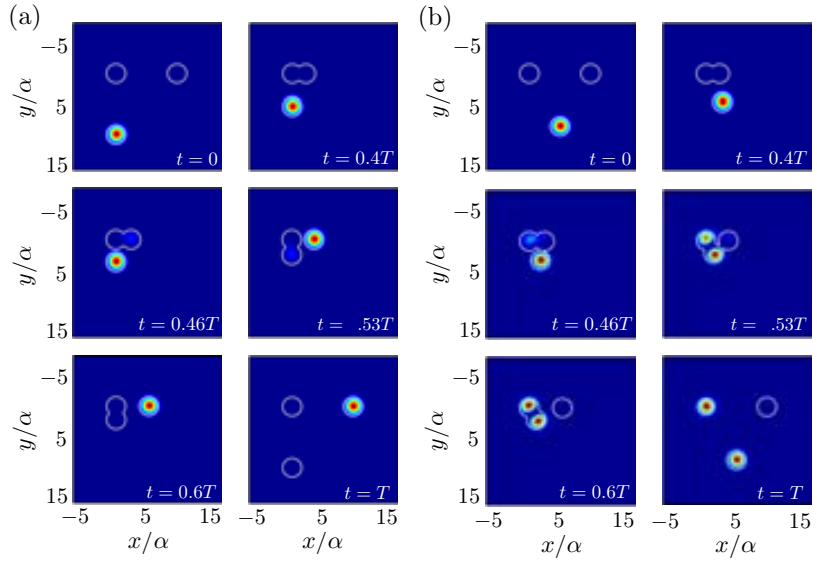

Figure 5.5: Temporal evolution of the population distribution of the single particle in the system of three traps with broken spatial symmetry for $T = 5000 \ ^{-1}$ and the parameter values as in Fig. 5.2 but with $\beta = \omega \ 2$ (a) and $\beta = 2\omega \ 3$ (b).

Fig. 5.5 shows the population distribution at different times for a process of total time $T = 5000 \ ^{-1}$ with (a) $\beta = \omega \ 2$ and (b) $\beta = 2\omega \ 3$. One can see in Fig. 5.5(a) that a single particle is completely transferred from the A trap to the C trap, which corresponds to the adiabatic following of the eigenstate Ψ_2. Contrarily, in Fig. 5.5(b) we can see that the atom ends up in a superposition of traps A and B. This is due to the energy level crossing that occurs at $t = 0 \ 5T$ when the three traps are equidistant, which implies that the system is transferred from Ψ_2 to Ψ_3, following Ψ_3 until the end of the process.

5.4 Single atom interferometry

In the previous section we have seen that for $\beta = \beta_{th}$ the transfer of population between A and C traps fails, and the atomic wavefunction ends up in Ψ_3, which is a coherent antisymmetric superposition of A and B traps with equal probabilities. This coherent splitting of the atomic wavefunction and its eventual recombination can be used to implement a robust atomic interferometer as it will be discussed in the following lines.

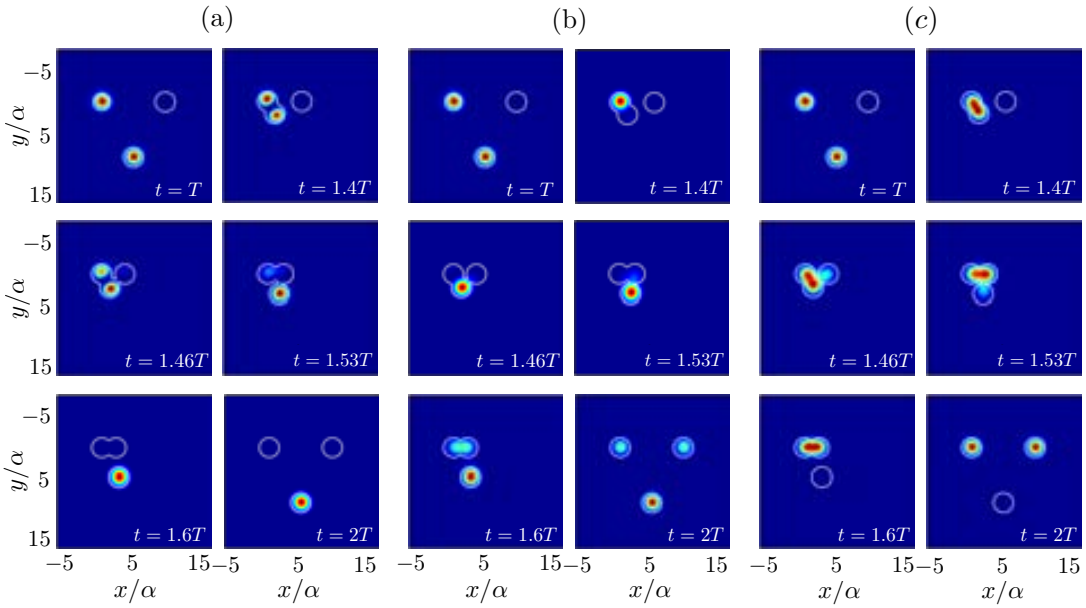

Figure 5.6: Temporal evolution of the population distribution of the single particle in the system during the recombination process for (a) = 0, (b) = ω 2 and (c) = ω.

The first step of the interferometer corresponds to the splitting process due to the level crossing already depicted in Fig. 5.5(b). At the end of the splitting, at time T, we perform the second step by imprinting a relative phase, , between the A and B traps. The last step is the recombination process that consists of reversing in time the evolution of the couplings performed during the splitting process, i.e., keeping β fixed, we approach and separate first A and B traps, and with a certain time delay we approach and separate C and B traps. At the final time, $2T$, the population distribution of the output atomic state among the asymptotic states of the traps will allow for a direct measurement of the imprinted phase.

To check the performance of the interferometer, Fig. 5.6 shows the population distribution at different times during the recombination process for (a) = 0, (b) = ω 2, and (c) = ω. It is clearly shown in Fig. 5.6(a) that for = 0, at the end of the process ($t = 2T$), the atom returns to trap A. This is due to the complete reversibility of the splitting process that leads to the transfer back of the system from

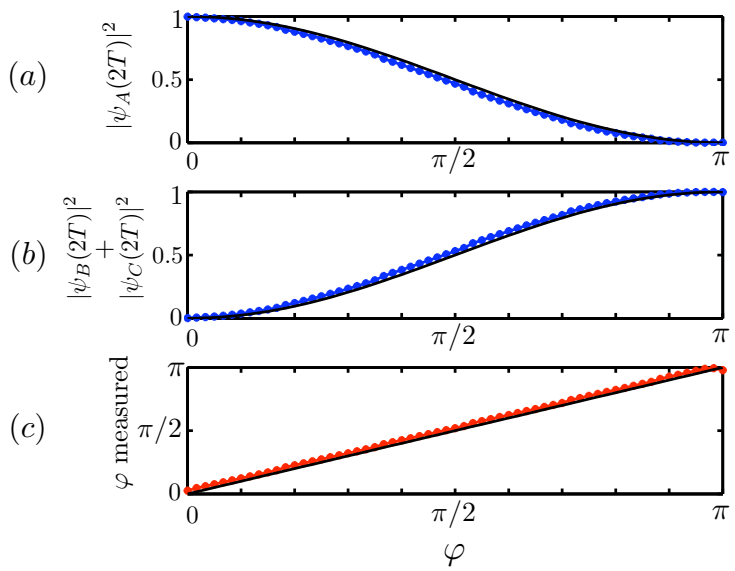

Figure 5.7: Population at the end of the process ($t = 2T$) of trap A (a), sum of the populations of traps B and C (b) and measured phase difference between A and B traps as a function of the imprinted phase difference at $t = T$. These results correspond to a total time $t = 2T = 8000\ \ ^{-1}$.

state Ψ_3 to Ψ_2 at the particular time for which the crossing of energy levels occurs. After the crossing, the system follows Ψ_2, which at the end of the process has only contribution of $\ _A$.

When a phase difference, $\ $, between the A and B traps is imprinted after the splitting process, the state of the system becomes $\Psi_\varphi(T) = \frac{1}{\sqrt{2}}(\ _A - e^{i\varphi}\ _B)$ which can be decomposed at this particular time in a superposition of $\Psi_3(T) = \frac{1}{\sqrt{2}}(\ _A - \ _B)$ and $\Psi_1(T) = \frac{1}{\sqrt{2}}(\ _A + \ _B)$. By reversing the sequence of couplings, the Ψ_3 contribution will be transfered to Ψ_2 at the level crossing and it will end up in trap A while the Ψ_1 contribution will evolve backwards according to Fig. 5.4(b) and at the end of the process will be in a superposition of traps B and C. Thus, by measuring the population of the three traps at the end of the process one can infer the phase difference between A and B traps just before the recombination process. The populations of traps B and C at the output of the interferometer read:

$$\ _B(2T)\ ^2 + \ \ _C(2T)\ ^2 = \ \ \Psi_1 \ \ _\varphi\ \ ^2 = \frac{1}{2}(1 - \cos\ \ ) \tag{5.19}$$

while the population of trap A is given by:

$$\ _A(2T)\ ^2 = \ \ \Psi_3 \ \ _\varphi\ \ ^2 = \frac{1}{2}(1 + \cos\ \ ) \tag{5.20}$$

Thus, the phase difference between A and B traps can be written as

$$= \pm \arccos \left[\frac{{}_A(2T)^{\,2} - (\quad {}_B(2T)^{\,2} + \quad {}_C(2T)^{\,2})}{{}_A(2T)^{\,2} + \quad {}_B(2T)^{\,2} + \quad {}_C(2T)^{\,2}} \right] \tag{5.21}$$

In Fig. 5.7, we plot the analytic prediction and the numerically obtained population at the end of the process ($t = 2T$) of trap A (a), the sum of the populations of traps B and C (b) and the measured phase difference between A and B traps as a function of the imprinted phase difference at $t = T$. We clearly see a full agreement between the results from Eq. (5.19), Eq. (5.20) and Eq. (5.21) and the corresponding numerical integration of the 2D Schrodinger equation. The nearly linear behavior between the measured phase difference with the imprinted one evidences the excellent performance of the described system as a matter wave interferometer.

5.5 Conclusions

We have discussed two-dimensional spatial adiabatic passage for a single cold atom in a trapping potential consisting of three two-dimensional harmonic wells forming a triangular configuration. It has been shown analytically and numerically the successful performance of spatial adiabatic passage for a broad range of parameters. However, there is a critical configuration for which the three tunneling rates become equal at a particular time during the dynamics which, implies a level crossing in the system s eigenvalue spectrum. This level crossing produces a coherent splitting of the matter wave that we have used as the first step to build up a matter wave interferometer. Once the matter wave is split between two of the traps we have imprinted a relative phase between these two traps showing that the recombination process results in a distribution of the matter wave among the asymptotic states of the traps that depends on the imprinted phase. Finally, we have numerically checked the excellent performance of the interferometer to measure the imprinted phase.

6

Tunneling induced angular momentum for single cold atoms via spatial adiabatic passage

In this chapter we demonstrate the possibility to generate states carrying angular momentum for a single cold atom by breaking the symmetry of a spatial adiabatic passage process in a two-dimensional system of three harmonic potential wells [107]. The spatial symmetry is broken by rotating the position of the initial trap with respect to the middle trap. With this new configuration, by performing a spatial adiabatic passage sequence, a superposition of two eigenstates of the system are adiabatically followed and the single cold atom is completely transferred to the first excited states of the final trap, which are resonantly coupled via tunneling to the ground states of the initial and middle traps. Depending on the total time of the process, angular momentum is generated in the final trap, with values that oscillate between $\pm$. It is also shown that both a complete transfer and generation of angular momentum can be obtained for broad range of parameter values. We discuss the process in terms of the asymptotic states of the individual wells and the results are checked by numerical simulation of the full two-dimensional Schrodinger equation.

6.1 Introduction

Controlling the states of quantum particles is a challenging task and a topic of significant present activity in the fields of Atom Optics, Quantum Computation, Quantum Metrology, and Quantum Simulation of condensed matter systems [164, 156, 165, 131, 166]. In particular, the generation of angular momentum for matter waves is attracting a lot of attention as, for instance, in studying superfluid properties of Bose-Einstein condensates (BECs) [167]. These condensates can sustain vortices, which have been envisioned to be used in applications for interferometry, as for example gyroscopy with counter-rotating vortex superpositions [168], Quantum Information, such as coherent superpositions of arbitrary winding numbers [169, 170] or entangled vortex states [171],

and as a way to study the behavior of random polynomial roots [172]. Different techniques have been proposed and experimentally reported to generate angular momentum with single atoms and BECs, such as stirring with a laser beam [173], phase imprinting [174, 175], transfer of orbital angular momentum from optical states [176, 177, 178], rotating traps [179, 180, 167, 181], turbulence [182], dynamical instabilities [183] or merging multiple trapped BECs [184].

At the same time, adiabatic techniques to control the external degrees of freedom of massive particles have been developed [50], based on the spatial analogue of the Stimulated Raman Adiabatic Passage technique [34]. For the centre-of-mass degree of freedom, this is usually realized by considering a triple well configuration and assuming that only a single state in each trap contributes to the dynamics. Up to now, all proposals in which the spatial adiabatic passage technique has been discussed have been effectively one-dimensional (1D): the traps are arranged in a linear geometry and a single particle in one of the outer traps is coherently transferred to the other outermost trap with very high fidelity. Significant work has been done for this process by discussing efficiency and robustness for single atoms [50, 51, 54, 69, 78, 79], electrons [70], atomic vortices [71], holes [55] and BECs [72, 73, 74, 75]. Recently, spatial adiabatic passage for light propagating in a system of three coupled optical waveguides [43, 82, 83] has been experimentally reported.

In this chapter, we go beyond those well understood 1D systems and focus onto the possibilities offered by two-dimensional (2D) setups. Higher dimensional systems often allow for new processes arising from the additional degrees of freedom and here we will address the generation of angular momentum for a single particle, e.g., a single cold atom, by means of 2D tunnel-coupling between traps. Angular momentum is an inherent two-dimensional (2D) quantity, which can only be created in systems in which rotational symmetry is broken. We demonstrate that, by applying a spatial adiabatic passage sequence in a system of three traps with broken spatial symmetry, a single particle can be completely transferred from the ground vibrational state of the initial trap to the two degenerate first excited states of the final trap. Depending on the total time of the process, this can generate angular momentum with values oscillating between $\pm$. Note that such a two-dimensional process has no analogue in quantum optical systems involving internal states. Furthermore, the process is robust since both, the complete transfer and the generation of angular momentum, occur within a broad range of parameter values.

In the following we first introduce the physical system consisting of three potential harmonic wells and we show the necessity of breaking the spatial symmetry of the system in order to generate angular momentum with a single cold atom by means of a spatial adiabatic passage sequence of couplings. Afterwards, using the asymptotic states of the individual traps and the couplings between them, both the complete transfer of population to the final trap and the process of generation of angular momentum are described by finding the energy eigenvalues and eigenstates of the system. Finally, numerical integrations of the full 2D Schrodinger equation, which confirm the predicted

results, are presented.

6.2 Physical system

We consider a system consisting of three two-dimensional harmonic potentials (labeled A, B and C), in which initially a single particle is located in the vibrational ground state of trap A. The trapping frequencies of A and B are equal ($_A = _B =$) and the one for C is chosen as half that value ($_C =$ 2). Such an arrangement means that the ground energy levels in traps A and B are in resonance with the first excited level in trap C allowing for effective tunnel-coupling.

Due to the symmetry in each of the individual potentials, the eigenstates can either be described in cartesian coordinates, leading to the standard quantum numbers n_x and n_y, or in polar coordinates using the quantum numbers n and l, where n is the principal quantum number and l corresponds to the topological charge. In our situation the resonant first excited energy level in trap C is degenerate as $E^C_{n_x,n_y} = E^C_{1,0} = E^C_{0,1}$ or as $E^C_{n,l} = E^C_{1,1} = E^C_{1,-1}$. Angular momentum can only be present when both states with energies $E^C_{n_x,n_y} = E^C_{1,0}$ and $E^C_{n_x,n_y} = E^C_{0,1}$ have finite occupancy and there is a certain phase difference between them. For example, direct tunneling between the ground state of a trap of trapping frequency and the first excited states of a trap with trapping frequency 2, without any initial angular momentum present, can only lead to occupation of either the state with energy $E^C_{1,0}$ or the one with $E^C_{0,1}$, or a combination of both with zero phase difference, not allowing for angular momentum generation. In particular, maximum angular momentum, $L_z = \pm$, occurs when the two degenerate states in cartesian coordinates are (i) equally populated and (ii) have a phase difference of ω 2, i.e.:

$$ _{1,\pm1}^{C}(r\ \theta) = \frac{1}{\overline{2}}\left[\ _{1,0}^{C}(x\ y) \pm i\ _{0,1}^{C}(x\ y)\right] \tag{6.1}$$

where $_{n,l}^{C}(r\ \theta) = _{1,\pm1}^{C}(r\ \theta)$, in polar coordinates, and $_{n_x,n_y}^{C}(x\ y) = _{1,0}^{C}(x\ y)$ and $_{n_x,n_y}^{C}(x\ y) = _{0,1}^{C}(x\ y)$, in cartesian coordinates and in a $x-y$ reference frame, are the eigenfunctions of the first excited states of the C trap.

6.3 Effective one-dimensional case

We will start studying the case of spatial adiabatic passage with the three 2D traps lying and moving on a straight line. During the process, the positions of the trap centers are $x_A = -d_{AB}$, $y_A = 0$, $x_B = y_B = 0$, $x_C = d_{BC}$ and $y_C = 0$, where d_{AB} and d_{BC} are the distances between the traps A and B and B and C, respectively (see Fig. 6.1). We consider four different states which are in resonance, the ground states of A and B traps and the two first excited states of the C trap. In the chosen reference frame $x-y$ and cartesian coordinates, the A and B trap ground states can be expressed

as:

$$\overset{A}{}_{0,0}(x\ \ y) = \theta_0^{\omega}(x + d_{AB})\theta_0^{\omega}(y) \tag{6.2}$$

and

$$\overset{B}{}_{0,0}(x\ \ y) = \theta_0^{\omega}(x)\theta_0^{\omega}(y) \tag{6.3}$$

respectively. Here θ_0^{ω} is the single-particle ground state eigenfunction of the one-dimensional quantum harmonic oscillator with trapping frequency :

$$\theta_0^{\omega}(x) = \left(\frac{m}{\omega}\right)^{1/4} \exp\left(-\frac{m\ \ x^2}{2}\right) \tag{6.4}$$

where m is the mass of the particle.

For the C trap with 2 we consider the eigenfunctions

$$\overset{C}{}_{1,0}(x\ \ y) = \theta_1^{\omega/2}(x - d_{BC})\theta_0^{\omega/2}(y) \tag{6.5}$$

and

$$\overset{C}{}_{0,1}(x\ \ y) = \theta_0^{\omega/2}(x - d_{BC})\theta_1^{\omega/2}(y) \tag{6.6}$$

where $\theta_0^{\omega/2}$ and $\theta_1^{\omega/2}$ are the single-particle ground and first excited state eigenfunction of the one-dimensional quantum harmonic oscillator with trapping frequency 2, respectively:

$$\theta_0^{\omega/2}(x) = \left(\frac{m\ \ 2}{\omega}\right)^{1/4} \exp\left(-\frac{m(\ \ 2)x^2}{2}\right) \tag{6.7}$$

$$\theta_1^{\omega/2}(x) = \ \ \overline{2}\left(\frac{m\ \ 2}{\sqrt[3]{\ }\overline{\omega}}\right)^{3/4} x \exp\left(-\frac{m(\ \ 2)x^2}{2}\right) \tag{6.8}$$

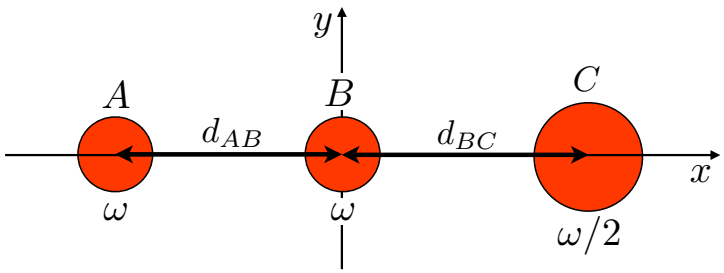

Figure 6.1: Schematic representation of the system of three 2D harmonic traps for the linear configuration. The A and B traps have a trapping frequency and C trap a trapping frequency 2.

The tunneling rates coupling the different traps of the system depend on the trap separation and can be calculated analytically considering harmonic truncated potentials

[50], see Appendix A. In this linear configuration, A and B traps, and B and C traps are coupled with rates J^{AB} and J^{BC}, respectively, whereas A and C traps are assumed to be separated enough to neglect direct coupling between them. In particular, because of the symmetry of the system, J^{BC} only couples the state $\overset{B}{}_{0,0}(x\ y)$ of the B trap with the $\overset{C}{}_{1,0}(x\ y)$ state of the C trap. In this way, the other excited state, $\overset{C}{}_{0,1}(x\ y)$, does not play any role in the dynamics and the problem can be modeled with a 3×3 Hamiltonian using the base $\overset{A}{}_{0,0}\ \overset{B}{}_{0,0}\ \overset{C}{}_{1,0}$:

$$H = \frac{}{2} \begin{pmatrix} 0 & -J^{AB} & 0 \\ -J^{AB} & 0 & -J^{BC} \\ 0 & -J^{BC} & 0 \end{pmatrix} \tag{6.9}$$

As we saw in Chapter 1, by diagonalizing this Hamiltonian, it is possible to find an energy eigenstate, the so-called spatial dark state, that only involves the asymptotic states of the outermost traps:

$$\Psi_D(\Theta) = \cos\Theta\ \overset{A}{}_{0,0} - \sin\Theta\ \overset{C}{}_{1,0} \tag{6.10}$$

where the mixing angle Θ is given by $\tan\Theta = J^{AB}\ J^{BC}$ [34, 51, 54, 69, 78, 79]. With a single cold atom initially located in the ground state of the A trap, $\overset{A}{}_{0,0}(x\ y)$, a spatial adiabatic passage sequence [51, 54, 69, 78, 79] can be applied by moving the traps along the x axis: keeping the B trap in a fixed position, the C trap is approached and separated to the B trap, and later on with a certain temporal overlap the A trap is approached and separated to the B trap. By doing this, Θ changes from 0 to ω 2 and, therefore, the dark state evolves from $\overset{A}{}_{0,0}(x\ y)$ to $\overset{C}{}_{1,0}(x\ y)$. Therefore, if the sequence is adiabatically performed, the dark state is followed, being the cold atom completely transferred to the first excited state $\overset{C}{}_{1,0}(x\ y)$ of the C trap. However, although the single atom can be completely transferred to the C trap, with this geometry it is not possible to generate angular momentum because there is no transfer of population to the $\overset{C}{}_{0,1}(x\ y)$ state. Numerical simulations of the 2D Schrodinger equation supporting this will be shown in Section 6.6.

6.4 Two-dimensional case

In order to populate both of the degenerate states of the first excited level of C traps towards the generation of angular momentum, it is necessary to break the spatial symmetry of the linear configuration. With this aim, we will consider a geometry in which the A trap is rotated around the B trap and forms an angle β with respect to the x axis, as can be seen in Fig. 6.2. The positions of the trap centers are $x_A = -d_{AB}\cos\beta$, $y_A = -d_{AB}\sin\beta$, $x_B = y_B = 0$, $x_C = d_{BC}$ and $y_C = 0$. Since we have rotated the position of the A trap, its new eigenfunction for the ground vibrational state has to be rewritten, in cartesian coordinates, as:

$$\overset{A}{}_{0,0}(x\ y) = \theta_0^{\omega}(x - d_{AB}\cos\beta)\theta_0^{\omega}(y + d_{AB}\sin\beta) \tag{6.11}$$

The other eigenfuctions for B and C traps have the same expressions as for the linear case (Eqs. (6.3), (6.5) and (6.6)).

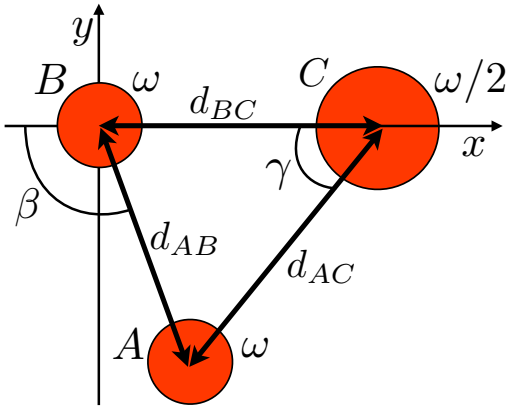

Figure 6.2: Schematic representation of the system of three harmonic 2D traps with broken spatial symmetry. As for the linear case, the traps A and B have a trapping frequency and trap C has a trapping frequency 2.

The breaking of symmetry introduces two new effects with respect to effective 1D configurations: (i) traps A and C can get close enough to allow direct tunnel coupling and (ii) there is no longer a preferred direction along which one of the states in C can line up. Thus, since the position of the A trap with respect to the C trap forms an angle γ with the x axis, there is a population transfer between the state $^{A}_{0,0}(x\ y)$ and $^{C}_{1,0}(x\ y)$ with coupling rate $J^{AC}_{1,0}$, but also between $^{A}_{0,0}(x\ y)$ and $^{C}_{0,1}(x\ y)$ with coupling rate $J^{AC}_{0,1}$. Therefore, both first excited states of the C trap become involved in the dynamics of the system, which in the basis $^{A}_{0,0}$ $^{B}_{0,0}$ $^{C}_{1,0}$ $^{C}_{0,1}$ can be described by the 4×4 Hamiltonian:

$$H = \frac{}{2} \begin{pmatrix} 0 & -J^{AB} & -J^{AC}_{1,0} & -J^{AC}_{0,1} \\ -J^{AB} & 0 & -J^{BC} & 0 \\ -J^{AC}_{1,0} & -J^{BC} & 0 & 0 \\ -J^{AC}_{0,1} & 0 & 0 & 0 \end{pmatrix} \tag{6.12}$$

It is straightforward to check that Hamiltonian (6.12) possesses four non-degenerate eigenvalues, except for J^{BC} $\overline{2} = J^{AB} = J^{AC}_{1,0} = J^{AC}_{0,1}$ when two of them become degenerate. As previously, the coupling rates depend on the trap separation and can be calculated analytically considering harmonic truncated potentials [50], see Appendix A. Additionally, since in the chosen $x-y$ reference frame the ground state of A trap is coupled to both degenerate first excited states in C, the two coupling rates depend on the angle γ as $J^{AC}_{1,0} = J_{\omega,\omega/2}\cos\gamma$ and $J^{AC}_{0,1} = J_{\omega,\omega/2}\sin\gamma$, where $J_{\omega,\omega/2}$ is the coupling rate between the ground state of a trap with trapping frequency and a resonant first excited state of a trap with trapping frequency 2.

6.5 Generation of angular momentum carrying states

The generation of angular momentum occurs along with the transfer of the particle from the A to the C trap through a spatial adiabatic passage process [50, 51, 54, 69, 78, 79]. As for the linear case, this corresponds to a counterintuitive temporal sequence of the couplings, i.e. with the particle initially located in A and the position of B being fixed, the C trap is first moved towards and away from the B trap along the x axis, and with a certain temporal delay, δ, the A trap approaches and moves away from the B trap, keeping the angle β constant. In the following, we will analyze this process in terms of the overall energy eigenvalues and eigenstates of the system by diagonalizing the Hamiltonian in Eq. (6.12), which is the only way to obtain a deeper understanding of the process due to the complex interplay of the three traps affecting each other. To approach and separate the traps, the evolution of the distances d_{BC} and d_{AB} follows a cosine function evaluated between 0 and 2ω, see Fig. 6.3(a) left. The right hand side panel of Fig. 6.3(a) shows the corresponding tunneling rates, and Fig. 6.3(b) displays the temporal evolution of all four energy eigenvalues of the Hamiltonian. Note that for the chosen parameters no level crossing occurs.

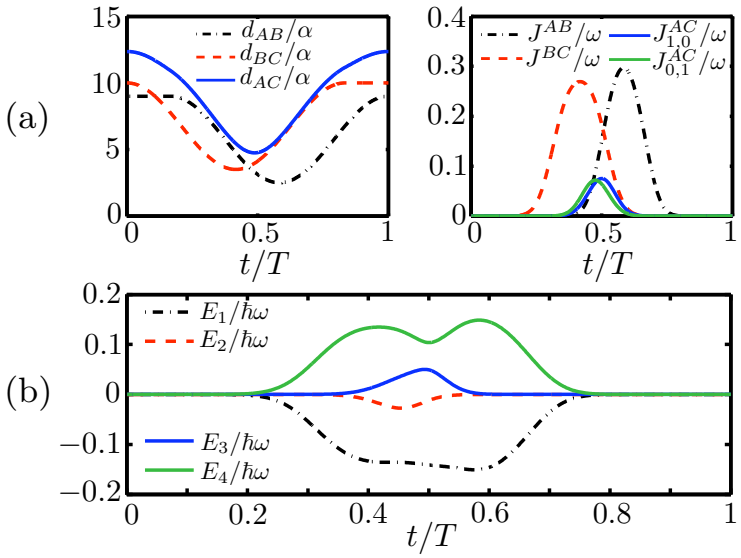

Figure 6.3: (a) Temporal evolution of the distances between traps d_{AB}, d_{BC} and d_{AC} (left panel), and the couplings J^{AB}, J^{BC}, $J^{AC}_{1,0}$ and $J^{AC}_{0,1}$ (right panel), during the spatial adiabatic passage process. (b) Energy eigenvalues as a function of time. The parameter values are: $\beta = 0\ 55\omega$, $\delta = 0\ 2T$, and d_{BC} and d_{AB} with values between 10α and $3\ 5\alpha$, and 9α and $2\ 5\alpha$, respectively, where $\alpha = \sqrt{\quad(m\quad)}$, and T is the total time of the process.

The population of each asymptotic level of the traps for the four energy eigenstates

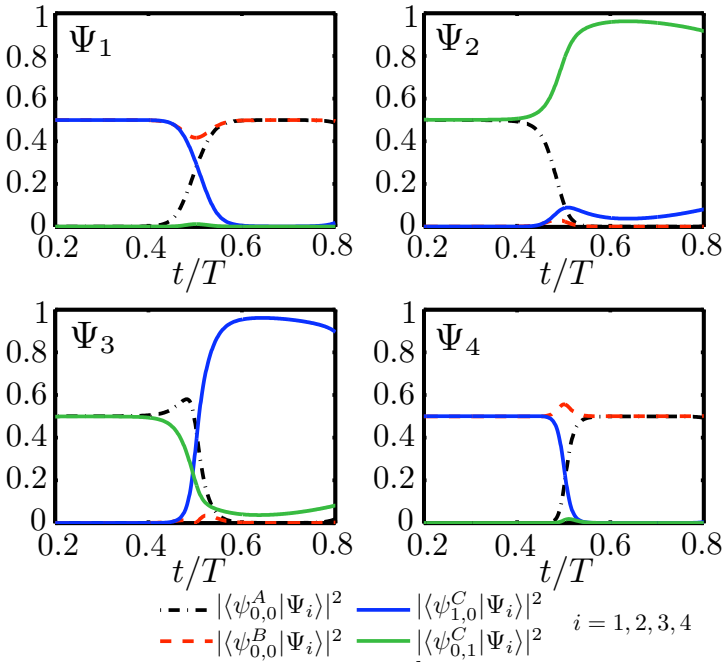

Figure 6.4: Temporal evolution of the population of each asymptotic level of the traps ($^A_{0,0}$, $^B_{0,0}$, $^C_{1,0}$ and $^C_{0,1}$) for the four eigenstates of the system (Ψ_1, Ψ_2, Ψ_3 and Ψ_4). The parameter values are as in Fig. 6.3.

of the system is shown in Fig. 6.4. Since initially the particle is in the A trap, the eigenfunction of the system at $t = 0$ can be written as a superposition of the eigenstates Ψ_2 and Ψ_3 as

$$(t = 0) = \frac{1}{\overline{2}} [\Psi_2(t = 0) + \Psi_3(t = 0)] = \ ^A_{0,0} \tag{6.13}$$

where $\Psi_2(t = 0) = (\ ^A_{0,0} + \ ^C_{0,1}) \quad \overline{2}$ and $\Psi_3(t = 0) = (\ ^A_{0,0} - \ ^C_{0,1}) \quad \overline{2}$. If the process is adiabatic and level crossings are absent, this superposition of eigenstates is followed all through the process, leading to a final state of the form

$$(t = T) = \frac{1}{\overline{2}} \left[\Psi_2(t = T) \exp\left(-\frac{i}{-} \int_0^T E_2 dt \right) + \right.$$
$$\left. \Psi_3(t = T) \exp\left(-\frac{i}{-} \int_0^T E_3 dt \right) \right] \tag{6.14}$$

In particular, as it can be seen from Fig. 6.4 that, at the final time T, Ψ_2 and Ψ_3 only involve the asymptotic states of the C trap, $^C_{1,0}(x\ y)$ and $^C_{0,1}(x\ y)$:

$$\Psi_2(t = T) = a\ ^C_{0,1} - b\ ^C_{1,0} \tag{6.15}$$

$$\Psi_3(t=T) = b\ {}^{C}_{0,1} + a\ {}^{C}_{1,0} \tag{6.16}$$

where $a^{\,2} + b^{\,2} = 1$. This means that by following the two eigenstates Ψ_2 and Ψ_3, a complete transfer of population from the initial trap A to the final trap C is achieved. Moreover, superpositions $(a\ {}^{C}_{0,1} - b\ {}^{C}_{1,0})$ and $(b\ {}^{C}_{0,1} + a\ {}^{C}_{1,0})$ are also two asymptotic eigenstates of the C trap, just in a $x\ -y$ rotated reference frame respect to the original ones, ${}^{C}_{1,0}(x\ y)$ and ${}^{C}_{0,1}(x\ y)$. We can call them

$${}^{C}_{0,1}(x\ \ y\ ) = \Psi_2(t=T) \tag{6.17}$$

$${}^{C}_{1,0}(x\ \ y\ ) = \Psi_3(t=T) \tag{6.18}$$

It is then easy to see from Eq. (6.14) that ${}^{C}_{0,1}(x\ \ y\ )$ and ${}^{C}_{1,0}(x\ \ y\ )$ are equally populated and that the phase difference between them is given by

$$(t=T) = \frac{1}{-}\int_0^T (E_3(t) - E_2(t))dt \tag{6.19}$$

From Fig. 6.3(b) it can be seen that the phase difference will be directly proportional to T, since the energy difference between the energy eigenvalues E_3 and E_2 follows the same pattern, independent of the total time of the process. Rewriting Eq. (6.14) in polar coordinates it is possible to show that the expected value of the angular momentum is a function of the phase difference

$$L_z(T)\ \ = \sin[\ \ (T)] \tag{6.20}$$

Therefore, the generated angular momentum L_z will follow a sinusoidal curve as a function of the total time of the process T, with a maximum at $\quad = (n + 1\ \ 2)\omega$ for $n\quad \mathbb{N}$.

Figs. 6.3 and 6.4 correspond to a particular value of the angle $\beta = 0\ 55\omega$. However, we have checked that the above process works for all angles $0 < \beta < \beta_t$, which is the parameter range in which the energy eigenspectrum and eigenfunctions are similar to the ones shown in Fig. 6.3 and 6.4. The only significative variation is that the energy difference between E_2 and E_3 is smaller for smaller angles, leading to longer oscillation periods of the angular momentum as a function of the total time of the process T. Around $\beta_t \approx 0\ 625\omega$, for a broad range of values of the distances d_{AB} and d_{BC}, the energy eigenstates Ψ_3 and Ψ_4 become almost degenerate at one point during the evolution, which limits the possibility to follow the superposition of the states Ψ_2 and Ψ_3 adiabatically. As discussed earlier, this particular time corresponds to the instant at which $J^{BC}\quad \overline{2} \approx J^{AB} \approx J^{AC}_{1,0} \approx J^{AC}_{0,1}$ and β_t therefore represents the angle up to which both, a complete transfer and the generation of angular momentum, work efficiently.

6.6 Numerical results

Although in the previous section we have used the asymptotic states of the individual traps to describe the dynamics of the system, the full dynamics is governed by the 2D Schrodinger equation:

$$i \ \frac{}{t} \ (x \ y) = \left[-\frac{^2}{2m} \ \ ^2 + V\,(x \ y) \right] \ \ (x \ y) \tag{6.21}$$

where ^{2} is the 2D Laplace operator. Here $V(x \ y)$ is the trapping potential, which we assume to be constructed from truncated harmonic oscillator potentials

$$V\,(x \ y) = \min_{i=A,B,C} \left\{ \frac{1}{2} m \ \ _i^2 \left[(x - x_i)^2 + (y - y_i)^2 \right] \right\} \tag{6.22}$$

where $(x_i \ y_i)$ with $i = A \ B \ C$ are the positions of each trap center, $_A = \ _B =$ and $_C = \ 2$. Thus, to establish the validity of our model above, we present in the following the numerical solution of Eq. (6.21), with the trapping potential Eq. (6.22) in the regime where $\beta < \beta_t$.

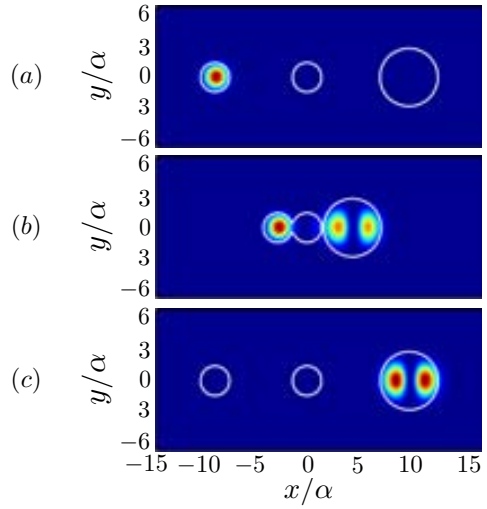

Figure 6.5: Temporal evolution of the population distribution of the single particle in the system of three traps with linear geometry. Three different times are shown: (a) the initial time, (b) the intermediate time $T \ 2 = 1500 \ ^{-1}$ and (c) the final total time $T = 3000 \ ^{-1}$.

First, the linear case configuration has been numerically simulated, with the results shown in Fig. 6.5. As it was expected, a complete transfer of the atom from the $^A_{0,0}$ state of the A trap to the $^C_{1,0}$ state of the C trap is obtained, with no final angular momentum.

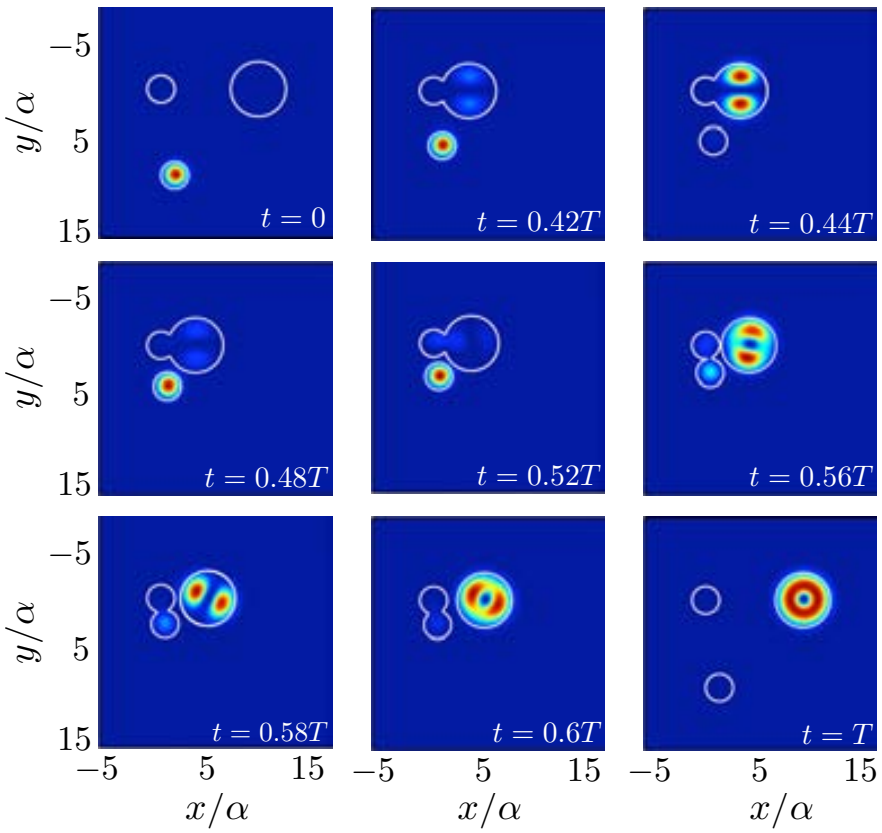

Figure 6.6: Temporal evolution of the population distribution of the single particle in the system of three traps with broken spatial symmetry for $T = 5183\ ^{-1}$ and the parameter values as in Fig. 6.3. The adiabatic following of the superposition of $\Psi_2(t)$ and $\Psi_3(t)$ can be observed by comparing with Fig. 6.4: from $t = 0\,42T$ to $t = 0\,48T$ oscillations corresponding to the phase difference between $\Psi_2(t < 0\,5T) = (\ ^{A}_{0,0} + \ ^{C}_{0,1})\ \ \overline{2}$ and $\Psi_3(t < 0\,5T) = (\ ^{A}_{0,0} - \ ^{C}_{0,1})\ \ \overline{2}$ are shown; for $t = 0\,58T$ and $t = 0\,6T$ oscillations due to the phase difference between $\Psi_2(t > 0\,5T) = \ ^{C}_{0,1}$ and $\Psi_3(t > 0\,5T) = \ ^{C}_{1,0}$ are also observed.

Secondly, numerical simulations of the triple-well potential system with broken spatial symmetry have been performed. The population distribution at different times is shown in Fig. 6.6 for a process of total time $T = 5183\ ^{-1}$. One can see that a single particle is completely transferred from the A trap to the C trap, where a state with maximum angular momentum, $L_z = -$, is created, which corresponds to the adiabatic following of the eigenstates Ψ_2 and Ψ_3 (see also point c in Fig. 6.7).

Calculations have also been performed in order to scan the values of the angular momentum as a function of the total time of the process T, as it is shown in Fig. 6.7. In

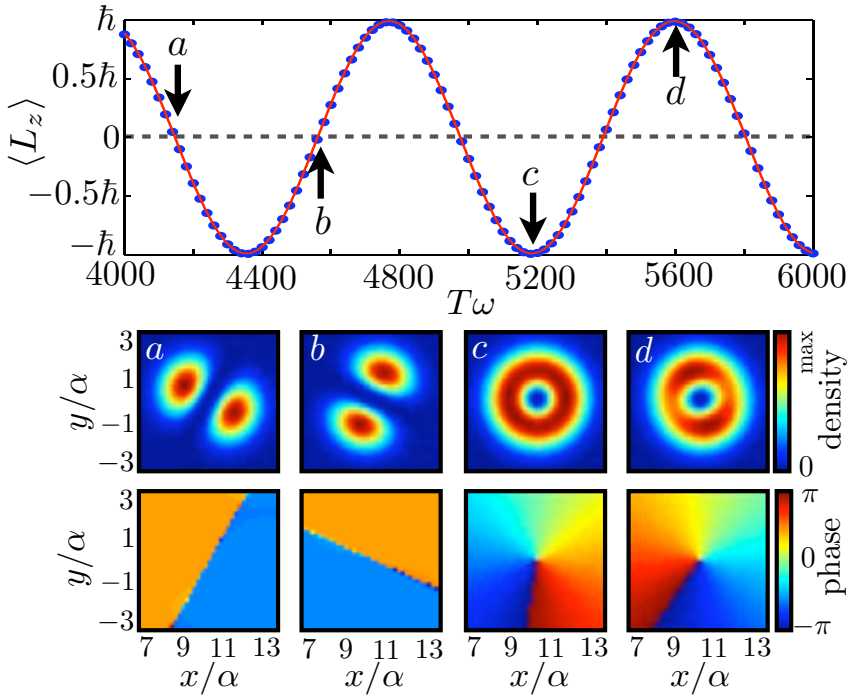

Figure 6.7: Generated angular momentum as a function of the total time of the process T (upper plot). Final states in the C trap and their phases for four different final total times a, b, c and d (lower plots). Parameter values as in Fig. 6.3.

agreement with Eq. (6.20), numerical results show a sinusoidal behavior of the angular momentum generated in the C trap as a function of the total time of the process T, with maximum values reaching $\pm\hbar$.

Fig. 6.8 shows the 2D numerical simulations for the angular momentum and the transfer of population to the C trap as a function of the β angle for a total time $T = 6000\omega^{-1}$. As predicted for the 4×4 formulation, both a complete transfer and values of the angular momentum close to $\pm\hbar$ are obtained from very small angles up to values close to $\beta_t = 0.625\pi$, proving the robustness of the process. It has also been numerically checked that if other parameter values (as the distances between the traps and the delay δ) are slightly changed, as long as the process is adiabatically performed, values of angular momentum close to $\pm\hbar$ can still be reached with a modification of the oscillation frequency of $\langle L_z \rangle$ as a function of the total time T. Thus, the process of complete transfer to the C trap and generation of angular momentum is very robust and highly versatile.

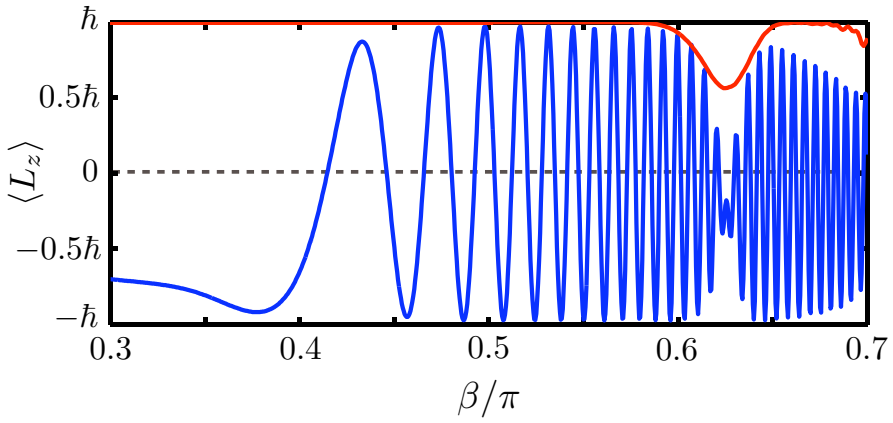

Figure 6.8: Generated angular momentum (blue line) and final transferred population in the C trap (red line) as a function of the β angle for a total time $T = 6000\omega^{-1}$. Parameter values are the same as in Fig. 6.3.

6.7 Conclusions

In this chapter we have demonstrated that angular momentum for a single cold atom can be successfully generated by breaking the symmetry of a spatial adiabatic passage sequence in a system of three 2D harmonic traps of different trapping frequency. A single cold atom initially in the ground state of a harmonic trap of frequency ω, can be fully transferred to the first excited states of a final harmonic trap of frequency $\omega/2$ by adiabatically following a superposition of two energy eigenstates of the system. The energy difference between these two eigenstates results in a phase difference between the equally populated excited states of the final harmonic trap, which leads to the generation of angular momentum. The obtained values oscillate between $\pm\hbar$ and depend on the total time of the process. We have modeled this process by using the asymptotic levels of the three harmonic traps and the couplings between them in a 4×4 Hamiltonian. Results have been checked against the numerical solution of the full 2D Schrödinger equation, proving the robustness of this spatial adiabatic passage process since both a complete transfer and values of the angular momentum up to $\pm\hbar$ can be found within a broad range of parameter values. Our work demonstrates that adiabatic techniques for centre-of-mass states hold significant potential for new processes, which have no direct equivalent in, for example, the control of internal degrees of freedom.

7

Conclusions and outlook

In this last chapter we will briefly summarize the main results that we have presented in this PhD thesis, remarking possible future perspectives.

Spatial adiabatic passage processes have been studied all along this thesis for the coherent control of light propagation in systems of coupled waveguides, sound propagation in systems of coupled linear defects in sonic crystals, and also for matter waves transport in systems of coupled waveguides and potential wells. Some of the main characteristics of the spatial adiabatic passage are its robustness and high efficiency to control the transfer of an oscillating quantity, such as light, sound or matter waves. Thus, in this thesis we have made use of these characteristics and the dependence of the adiabaticity condition on the parameters of the system to propose new devices and discuss new implementations in these various fields.

Before going to the details of each of the spatial adiabatic passage processes studied in this thesis, and in order to make clear how the spatial adiabatic passage can be addressed in such different physical systems as optical waveguides, linear defects in sonic crystals or dipolar traps or waveguides, in Chapter 1 we have set the common elements necessary to perform the adiabatic passage in different physical systems and we have also briefly reviewed some examples of the main adiabatic passage processes.

In Chapter 2 we have studied the spatial adiabatic passage of light in systems of three coupled waveguides. We have designed and fabricated systems of three evanescently coupled TIR silicon-oxide waveguides in which we have experimentally checked that it is possible to achieve a robust and highly efficient transfer of light between the outermost waveguides of the system. The robustness of the spatial adiabatic passage of light has been also experimentally checked by obtaining efficient transfer processes when measuring devices with differences in the geometry parameter values. In particular, for variations of the geometry parameter values between 20% and 35%, the relative fraction of intensity that has been transferred ranges from 0 87 to values above 0 99 for different measured systems of waveguides. Thus, the spatial adiabatic passage of light represents a powerful alternative in front of directional couplers, in which the transfer

of light between waveguides depends on precise geometry parameter values. Although the work presented in Chapter 2 is not the first implementation of spatial adiabatic passage of light [43, 44], it represents the first one using a CMOS-compatible technology, which could allow for the integration of the devices together with other photonic or electronic elements for a low-cost and allowing massive production. Furthermore, in Chapter 2 we have also theoretically proposed and experimentally demonstrated that a system of three TIR silicon oxide waveguides can be used as a high- and low-pass spectral filter. In this case, using the fact that the coupling strength depends on the wavelength, we have shown that, if light is injected into the right waveguide of the system, after propagating along the system, long wavelengths propagate to the left output, whereas short wavelengths are transferred into the central and right outputs. The filtering mechanism is based on the adiabaticity of the spatial adiabatic passage process and, therefore, we have referred to the fabricated devices as spatial adiabatic passage filters. We have also demonstrated that, depending on the geometry parameter values, the filtering characteristics can be tuned on wavelength but keeping the same filtering behavior. Additionally, the fabricated spatial adiabatic passage filters are also CMOS-compatible. Hence, due to their properties, spatial adiabatic passage filters can constitute a feasible alternative to other integrated filtering devices such as interference-based filters or absorbance based filters. Although we have focused this work within the visible range, an extension to other wavelength ranges is straightforward since, as we have discussed in Chapter 1, the conditions to perform spatial adiabatic passage processes can be fulfilled in systems of three coupled waveguides no matter of the specific value of the wavelength if the couplings between the waveguides are modified appropriately. Thus, for example, both the spatial adiabatic passage and the SAP filter could be implemented into the standard frequency range of telecommunications.

Spatial adiabatic passage processes for waves propagating in systems of three waveguides resemble the quantum optical stimulated Raman adiabatic passage technique [34] used to efficiently transfer the atomic population between the ground states of a Λ-type system of internal atomic levels in interaction with two laser pulses. A similar analogy can arise between the rapid adiabatic passage technique [35], used to coherently transfer the population between the ground and the excited levels of a system of two internal atomic levels that interact with a laser pulse of variable frequency, and systems of two coupled waveguides. This analogy gave rise to the proposals discussed in Chapter 3, where the propagation of sound waves in a sonic crystal is controlled in systems of two coupled linear defects by adiabatically following the available supermodes of the system. In Chapter 3 we have firstly calculated the band diagrams of the system of two linear defects. From them, we have extracted the information on how the geometry of the defects can be modified along the propagation direction in order to change the transverse profile of the supermodes. Additionally, two frequency regions have been identified, one where both the symmetric and antisymmetric supermodes of the system are present and another where only the antisymmetric supermode exists. For the first one, the coupled-mode theory can be used, giving an understandable insight into

the problem and allowing for the analogy with the rapid adiabatic passage technique [35]. Two applications based on spatial adiabatic passage have been proposed for (i) coherent multifrequency adiabatic splitting and (ii) phase difference analyzing. On the other hand, for the second range of frequencies, since only the antisymmetric supermode exists and transitions to other supermodes are strongly supressed, it is possible to design structures of much shorter length. In this case, a coherent multifrequency adiabatic splitter and a coupler have been designed. As for the structures implemented in Chapter 2, the robustness is also a quality present in the devices proposed in Chapter 3 and the obtained results are still valid if some fluctuations on the parameter values are present. It is important to note that the equations for sound propagation in sonic crystals can be directly related to the TE or TM modes for light propagation in two-dimensional systems. Therefore, the applications here discussed could be easily extended to the field of light propagation in photonic crystals with linear defects. Furthermore, the applications described through the coupled-mode equations could also be extended to other kind of optical waveguides such as the standard TIR waveguides.

Dipolar waveguides for the propagation of matter waves can also be used to perform spatial adiabatic passage processes, as we have discussed in Chapter 4. In this chapter, we have introduced a novel coherent mechanism for the injection, extraction, and velocity filtering of neutral atoms in a ring dipole trap. Control in the storage of matter waves in ring traps is a topic of present interest, since the characteristics of ring traps make them perfect candidates to investigate quantum phase transitions [132], matter wave Sagnac interferometry [133], stability of persistent currents and superconducting quantum interference devices [138], propagation of matter wave solitons and vortices [142], cold collisions [143], or artificial electromagnetism [144]. The proposed mechanisms for injection, extraction and velocity filtering make use of two additional curved dipole waveguides and are based on spatial adiabatic passage processes. These processes can be modeled in analogy to the well-known spatial adiabatic passage of single particles in coupled one-dimensional potential traps [50], showing that a transverse spatial dark state of the system is followed along the propagation of a single neutral atom. In Chapter 4 we have obtained a semi-analytical expression for the threshold longitudinal velocity of the atom allowing an efficient spatial adiabatic passage process, which is in good agreement with the results obtained by the two-dimensional numerical simulations of the Schrodinger equation. Furthermore, the robustness of the spatial adiabatic passage has been numerically demonstrated since high fidelities, above 97%, have been obtained for a significantly broad range of parameter values of the initial longitudinal velocity of the atoms and the minimum distance between the centers of the dipolar waveguides. In particular, it has been numerically checked that the injection, extraction and velocity filtering protocols are feasible for realistic experiments with state-of-the-art parameter values. Thus, a future experimental realization of the protocols could lead to a new way to control the storage of neutral atoms in ring dipole traps. Additionally, it could be also interesting to propose similar mechanisms for injecting, extracting and velocity filtering Bose Einstein condensates or solitons in a ring

trap to explore the role of the nonlinearity in these systems.

To the best of our knowledge, up to now all the spatial adiabatic passage proposals so far discussed in the literature can be considered as effectively one-dimensional as only one dimension is involved in the transfer process. In Chapter 5 and 6 we go beyond the well-known one-dimensional systems and we have studied the possibilities that spatial adiabatic processes offer in fully two-dimensional systems. In particular, in Chapter 5 we consider two-dimensional spatial adiabatic passage for a single cold atom in a system of three identical two-dimensional harmonic wells in a triangular configuration. We have shown both analytically and numerically that, by moving the traps following a counterintuitive coupling sequence, the transfer from the initial trap to the final trap is complete for a broad range of parameter values. Nevertheless, we have seen that if the traps are arranged in a particular configuration such that the three coupling rates are equal at a particular time during the process, two of the energy eigenvalues become degenerated. Thus, this configuration implies a level crossing, which produces an equal splitting of the matter wave between two of the traps of the system. This splitting offers the possibility to implement a matter wave interferometer. We have shown that after imprinting a relative phase between the two traps in which the matter wave is equally split, an inverse coupling sequence results in a distribution of the matter wave among the asymptotic states of the individual traps that depends on the imprinted phase. The proposal has been numerically checked with the integration of the full two-dimensional Schrodinger equation.

On the other hand, in Chapter 6 we have addressed the generation of angular momentum for a single cold atom in a system of three two-dimensional harmonic traps of different trapping frequencies in a triangular geometry. We have seen that by applying a spatial adiabatic sequence of couplings, a single cold atom located in the ground state of the initial trap of trapping frequency is completely transferred to the first excited states of a final harmonic trap of frequency 2, equally populating both of them. By modeling the process using the asymptotic states of the traps and the couplings between them with a 4×4 Hamiltonian, we have shown that the system adiabatically follows a superposition of two energy eigenstates of the system. Thus, the accumulated energy difference between these two eigenstates during the process results in a phase difference between the equally populated excited states of the final harmonic trap, which leads to the generation of angular momentum, with values that oscillate between $\pm$ depending on the total time of the process. Numerical integrations of the full two-dimensional Schrodinger equation have been performed in order to check the results. Moreover, we have numerically investigated the robustness of this spatial adiabatic passage and have found that both a complete transfer and values of the angular momentum up to $\pm$ can be found within a broad range of parameter values. Note that in a similar way as for BECs [168, 169, 170, 171], angular momentum with single cold atoms in potential traps could lead to applications in the fields of Interferometry and Quantum Information. As a whole, in Chapters 5 and 6 we have seen that a fully two-dimensional system allows for new processes that have no analogue in effective one-dimensional systems.

In conclusion, in this thesis we have demonstrated that spatial adiabatic passage is a highly versatile and general physical process, which can lead to very different applications in various fields of physics, and in which the robustness in the performance is the key element that makes it a unique process.

A

Appendix: coupling coefficients calculation

Coupling rates between two harmonic wells of trapping frequency separated a distance d can be calculated using both the Gram-Schmidt (GS) orthogonalization procedure or the Holstein Herring method.

A.1 Gram–Schmidt orthogonalization

We consider the single-particle ground state eigenfunctions of the 1D quantum harmonic oscillator for two traps separated a distance d, $\theta_0^\omega(x + d\ 2)$ and $\theta_0^\omega(x - d\ 2)$. With these two functions and finding a proper normalization we construct a symmetric eigenfunction:

$$\Phi_{+,0}^{\omega,\omega}(x) = \frac{1}{N_{+,0}^{\omega,\omega}} \left[\theta_0^\omega(x + d\ 2) + \theta_0^\omega(x - d\ 2)\right] \tag{A.1}$$

and an antisymmetric eigenfunction:

$$\Phi_{-,0}^{\omega,\omega}(x) = \frac{1}{N_{-,0}^{\omega,\omega}} \left[\theta_0^\omega(x + d\ 2) - \theta_0^\omega(x - d\ 2)\right] \tag{A.2}$$

The normalizations $N_s^{\omega,\omega}$ and $N_a^{\omega,\omega}$ are given by:

$$N_{+,0}^{\omega,\omega} = \int_{-} \left[\theta_0^\omega(x + d\ 2) + \theta_0^\omega(x - d\ 2)\right]^* \left[\theta_0^\omega(x + d\ 2) + \theta_0^\omega(x - d\ 2)\right] dx \tag{A.3}$$

$$N_{-,0}^{\omega,\omega} = \int_{-} \left[\theta_0^\omega(x + d\ 2) - \theta_0^\omega(x - d\ 2)\right]^* \left[\theta_0^\omega(x + d\ 2) - \theta_0^\omega(x - d\ 2)\right] dx \tag{A.4}$$

The energies of the symmetric, $E_{+,0}^{\omega,\omega}$, and the antisymmetric, $E_{-,0}^{\omega,\omega}$, eigenfunctions correspond to the expected values of the Hamiltonian with the truncated double well harmonic potential with both wells having a trapping frequency , $H^{\omega,\omega}$:

$$E_{+,0}^{\omega,\omega} = \int_{-} \Phi_{+,0}^{\omega,\omega}(x)^* H^{\omega,\omega} \Phi_{+,0}^{\omega,\omega}(x) dx \tag{A.5}$$

$$E_{-,0}^{\omega,\omega} = \int_{-} \quad \Phi_{-,0}^{\omega,\omega}(x)^* H^{\omega,\omega} \Phi_{-,0}^{\omega,\omega}(x) dx \tag{A.6}$$

The coupling rate between the two harmonic traps of frequency separated a distance d (if it appears as $-($ $2)J$ in the Hamiltonian) is given by

$$J_{0,0}^{\omega,\omega} = \frac{E_{-,0}^{\omega,\omega} - E_{+,0}^{\omega,\omega}}{} \tag{A.7}$$

With the already found eigenfunctions of the two-traps system, new eigenfunctions corresponding to higher excited vibrational states of the two coupled traps can be found by applying the recurrence relation of the Gram Schmidt (GS) [185] orthogonalization:

$$\begin{aligned} \Phi_{\pm,i+1}^{\omega,\omega} &= a_{\pm,i+1}\Phi_{\pm,i}^{\omega,\omega} + GS\left[x\right]\Phi_{\mp,i}^{\omega,\omega} + c_{\pm,i+1}\Phi_{\pm,i-1}^{\omega,\omega} \\ a_{\pm,i+1} &= -\left\langle \Phi_{\pm,i}^{\omega,\omega}\ GS\left[x\right]\ \Phi_{\mp,i}^{\omega,\omega} \right\rangle \ \left\langle \Phi_{\pm,i}^{\omega,\omega}\ \Phi_{\pm,i}^{\omega,\omega} \right\rangle \\ c_{\pm,i+1} &= -\left\langle \Phi_{\pm,i}^{\omega,\omega}\ \Phi_{\pm,i}^{\omega,\omega} \right\rangle \ \left\langle \Phi_{\pm,i-1}^{\omega,\omega}\ \Phi_{\pm,i-1}^{\omega,\omega} \right\rangle \end{aligned} \tag{A.8}$$

For harmonic potentials whose eigenfunctions are Hermite polynomials we have that $GS\left[x\right] = x$. For example, to find the first excited states of the two coupled traps, $\Phi_{\pm,1}^{\omega,\omega}$, we should take the previously found eigenstates $\Phi_{\pm,0}^{\omega,\omega}$ and choose $\Phi_{\pm,-1}^{\omega,\omega} = 0$ in the recurrence relation. The resulting orthogonal states have to be normalized after the GS procedure. Once the eigenfunctions for higher energy eigenstates are known, the coupling rates can be found similarly as in Eq. (A.5), Eq. (A.6) and Eq. (A.7).

A.2 Holstein–Herring method

In the main order approximation, which gives exact solution for the ground level $n = 0$, symmetric and antisymmetric states can be approximated by respective superposition of the asymptotic eigenfunctions of each potential $\Phi_{\pm,n}^{\omega,\omega} = \left(\theta_{n,L}^{\omega} \pm \theta_{n,R}^{\omega}\right) \quad \overline{2}$, where L and R correspond to the left and right trap, respectively. In this case, the Holstein Herring method [154, 155] can be applied, which provides and expression for the tunneling rate at an excited level n for identical potentials:

$$J_{n,n}^{\omega,\omega} = E_{-,n}^{\omega,\omega} - E_{+,n}^{\omega,\omega} = \left. \frac{- \quad \left(\theta_{n,L}^{\omega}\left(x\right)\right)^2}{1 - 2\int_x \ \left(\theta_{n,L}^{\omega}\left(z\right)\right)^2 dz} \right|_{x=x_Z} \tag{A.9}$$

where x_Z denotes the symmetry point at which the antisymmetric solution vanishes, i.e., $\Phi_{-,n}^{\omega,\omega}\left(x = x_Z\right) = 0$.

A.3 Coupling between resonant traps of different trapping frequencies

The coupling rate $J_{\omega,\omega/2}$ between the ground state of a trap with trapping frequency and a resonant first excited state of a trap with trapping frequency 2 can be found analogously to the method discussed in section A.1. In this case, the symmetric and antisymmetric states have to be constructed with the single-particle ground state eigenfunction of the one-dimensional quantum harmonic oscillator for one trap, for example $\theta_0^{\omega}(x + d\ 2)$, and the resonant single-particle first excited state eigenfunction of the one-dimensional quantum harmonic oscillator for the other trap, for example $\theta_1^{\omega/2}(x - d\ 2)$. The symmetric state can be written as

$$\Phi_{+,0}^{\omega,\omega/2}(x) = \frac{1}{N_{+,0}^{\omega,\omega/2}} \left[\theta_0^{\omega}(x + d\ 2) + \theta_1^{\omega/2}(x - d\ 2)\right] \tag{A.10}$$

while the antisymmetric eigenfunction reads

$$\theta_{-,0}^{\omega,\omega/2} = \frac{1}{N_{-,0}^{\omega,\omega/2}} \left[\theta_0^{\omega}(x + d\ 2) - \theta_1^{\omega/2}(x - d\ 2)\right] \tag{A.11}$$

The normalizations $N_{+,0}^{\omega,\omega/2}$ and $N_{-,0}^{\omega,\omega/2}$ are given by

$$N_{+,0}^{\omega,\omega/2} = \int_{-} \left[\theta_0^{\omega}(x + d\ 2) + \theta_1^{\omega/2}(x - d\ 2)\right]^* \left[\theta_0^{\omega}(x + d\ 2) + \theta_1^{\omega/2}(x - d\ 2)\right] dx \tag{A.12}$$

$$N_{-,0}^{\omega,\omega/2} = \int_{-} \left[\theta_0^{\omega}(x + d\ 2) - \theta_1^{\omega/2}(x - d\ 2)\right]^* \left[\theta_0^{\omega}(x + d\ 2) - \theta_1^{\omega/2}(x - d\ 2)\right] dx \tag{A.13}$$

The rest of the calculation is analogous to Eq. (A.5), Eq. (A.6) and Eq. (A.7).

Bibliography

[1] G. Kirchhoff. *Über das Verhältniss zwischen dem Emissionsvermögen und dem Absorptionsvermögen der Körper für Wärme und Licht.* Annalen der Physik **109**, 275 (1860).

[2] W. Hallwachs. *Ueber die Electrisirung von Metallplatten durch Bestrahlung mit electrischem Licht.* Annalen der Physik **270**, 731 (1888).

[3] P. Lenard. *Ueber die lichtelektrische Wirkung.* Annalen der Physik **313**, 149 (1902).

[4] E. C. Watson. *The first reported observations on emission spectra.* American Journal of Physics **20**, 569 (1952).

[5] N. Lockyer. *The story of helium.* Nature **53**, 319 (1896).

[6] A. J. Ångstrom. *Recherches sur le spectre solaire* (W. Schultz, Uppsala, 1868).

[7] M. Planck. *Über das Gesetz der Energieverteilung im Normalspektrum.* Annalen der Physik **4**, 553 (1901).

[8] A. Einstein. *Über die von der molekularkinetischen Theorie der Wärme geforderte Bewegung von in ruhenden Flüssigkeiten suspendierten Teilchen.* Annalen der Physik **322**, 549 (1905).

[9] H. Geiger and E. Marsden. *On a diffuse reflection of the α-particles.* Proceedings of the Royal Society A **82**, 495 (1909).

[10] E. Rutherford. *The scattering of α and β particles by matter and the structure of the atom.* Philosophical Magazine Series 6 **21**, 669 (1911).

[11] N. Bohr. *On the constitution of atoms and molecules I.* Philosophical Magazine Series 6 **26**, 1 (1913).

[12] N. Bohr. *On the constitution of atoms and molecules III.* Philosophical Magazine Series 6 **26**, 857 (1913).

[13] N. Bohr. *On the constitution of atoms and molecules II.* Philosophical Magazine Series 6 **26**, 476 (1913).

[14] A. Sommerfeld. *Zur Quantentheorie der Spektrallinien.* Annalen der Physik **356**, 1 (1916).

[15] P. Zeeman. *The effect of magnetisation on the nature of light emitted by a substance.* Nature **55**, 347 (1897).

[16] W. Pauli. *Über den Zusammenhang des Abschlusses der Elektronengruppen im Atom mit der Komplexstruktur der Spektren.* Zeitschrift fur Physik **31**, 765 (1925).

[17] L. de Broglie. *Recherches sur la théorie des quanta.* Annales de Physique **3**, 22 (1925).

[18] B. L. van der Waerden. *From matrix mechanics and wave mechanics to unified quantum mechanics.* Notices of the American Mathematical Society **44**, 323 (1997).

[19] M. Born and P. Jordan. *Zur Quantenmechanik.* Zeitschrift fur Physik **34**, 858 (1925).

[20] M. Born. *Quantenmechanik der stoßvorgänge.* Zeitschrift fur Physik **38**, 803 (1926).

[21] E. Schrodinger. *Quantisierung als Eigenwertproblem.* Annalen der Physik **386**, 109 (1926).

[22] W. Heisenberg. *Über den anschaulichen Inhalt der quantentheoretischen Kinematik und Mechanik.* Zeitschrift fur Physik **43**, 172 (1927).

[23] G. P. Thomson and A. Reid. *Diffraction of cathode rays by a thin film.* Nature **119**, 890 (1927).

[24] A. Szabo and N. S. Ostlund. *Modern quantum chemistry: Introduction to advanced electronic structure theory* (Dover Publications, New York, 1996).

[25] M. O. Scully and M. S. Zubairy. *Quantum optics* (Cambridge University Press, Cambridge, 1997).

[26] M. A. Nielsen and I. L. Chuang. *Quantum computation and quantum information* (Cambridge University Press, Cambridge, 2010).

[27] P. Alden and R. H. Sands. *The Ann Arbor conference on optical pumping: the University of Michigan, June 15 through June 18, 1959* (1959).

[28] A. L. Schawlow and C. H. Townes. *Infrared and optical masers.* Physical Review **112**, 1940 (1958).

[29] T. H. Maiman. *Stimulated optical radiation in ruby.* Nature **187**, 493 (1960).

[30] W. Demtroder. *Laser Spectroscopy: Basic Concepts and Instrumentation* (Springer, Berlin, 2003).

[31] R. W. Boyd. *Nonlinear optics* (Academic Press, San Diego, 2008).

[32] H. J. Metcalf and P. van der Straten. *Laser cooling and trapping* (Springer, Berlin, 1999).

[33] E. Arimondo, W. Phillips, F. Strumia, and S. I. di Fisica. *Laser manipluation of atoms and ions* (North-Holland, Amsterdam, 1992).

[34] K. Bergmann, H. Theuer, and B. W. Shore. *Coherent population transfer among quantum states of atoms and molecules.* Reviews of Modern Physics **70**, 1003 (1998).

[35] L. Allen and J. H. Eberly. *Optical resonance and two-level atoms* (Dover Publications, New York, 1987).

[36] A. Messiah. *Quantum mechanics*, volume 2 (North-Holland, Amsterdam, 1976).

[37] J. Benhelm, G. Kirchmair, C. F. Roos, and R. Blatt. *Towards fault-tolerant quantum computing with trapped ions.* Nature Physics **4**, 463 (2008).

[38] L.-M. Duan, J. I. Cirac, and P. Zoller. *Geometric manipulation of trapped ions for quantum computation.* Science **292**, 1695 (2001).

[39] A. Recati, T. Calarco, P. Zanardi, J. I. Cirac, and P. Zoller. *Holonomic quantum computation with neutral atoms.* Physical Review A **66**, 032309 (2002).

[40] D. Mfffller, L. B. Madsen, and K. Mfffmer. *Geometric phase gates based on stimulated Raman adiabatic passage in tripod systems.* Physical Review A **75**, 062302 (2007).

[41] K. Eckert, J. Mompart, X. X. Yi, J. Schliemann, D. Bruß, G. Birkl, and M. Lewenstein. *Quantum computing in optical microtraps based on the motional states of neutral atoms.* Physical Review A **66**, 042317 (2002).

[42] P. Zhang, Z. D. Wang, J. D. Sun, and C. P. Sun. *Holonomic quantum computation using rf superconducting quantum interference devices coupled through a microwave cavity.* Physical Review A **71**, 042301 (2005).

[43] S. Longhi, G. Della Valle, M. Ornigotti, and P. Laporta. *Coherent tunneling by adiabatic passage in an optical waveguide system.* Physical Review B **76**, 201101 (2007).

[44] Y. Lahini, F. Pozzi, M. Sorel, R. Morandotti, D. N. Christodoulides, and Y. Silberberg. *Effect of nonlinearity on adiabatic evolution of light.* Physical Review Letters **101**, 193901 (2008).

[45] R. Martínez-Sala, J. Sancho, J. V. Sánchez, V. Gómez, J. Llinares, and F. Meseguer. *Sound attenuation by sculpture.* Nature **378**, 241 (1995).

[46] J. V. Sánchez-Pérez, D. Caballero, R. Mártinez-Sala, C. Rubio, J. Sánchez-Dehesa, F. Meseguer, J. Llinares, and F. Gálvez. *Sound attenuation by a two-dimensional array of rigid cylinders.* Physical Review Letters **80**, 5325 (1998).

[47] E. Yablonovitch. *Inhibited spontaneous emission in solid-state physics and electronics.* Physical Review Letters **58**, 2059 (1987).

[48] T. F. Krauss, R. M. D. L. Rue, and S. Brand. *Two-dimensional photonic-bandgap structures operating at near-infrared wavelengths.* Nature **383**, 699 (1996).

[49] J. D. Joannopoulos. *Photonic crystals: Molding the flow of light* (Princeton University Press, Princeton, NJ, 2008).

[50] K. Eckert, M. Lewenstein, R. Corbalán, G. Birkl, W. Ertmer, and J. Mompart. *Three-level atom optics via the tunneling interaction.* Physical Review A **70**, 023606 (2004).

[51] K. Eckert, J. Mompart, R. Corbalán, M. Lewenstein, and G. Birkl. *Three level atom optics in dipole traps and waveguides.* Optics Communications **264**, 264 (2006).

[52] T. Busch, K. Deasy, and S. N. Chormaic. *Quantum state preparation using multi-level-atom optics.* Journal of Physics: Conference Series **84**, 012002 (2007).

[53] V. O. Nesterenko, A. N. Novikov, F. F. d. Cruz, and E. L. Lapolli. *STIRAP transport of Bose-Einstein condensate in triple-well trap.* Laser Physics **19**, 616 (2009).

[54] T. Opatrný and K. K. Das. *Conditions for vanishing central-well population in triple-well adiabatic transport.* Physical Review A **79**, 012113 (2009).

[55] A. Benseny, S. Fernández-Vidal, J. Bagudà, R. Corbalán, A. Picón, L. Roso, G. Birkl, and J. Mompart. *Atomtronics with holes: Coherent transport of an empty site in a triple-well potential.* Physical Review A **82**, 013604 (2010).

[56] M. Born and V. Fock. *Beweis des adiabatensatzes.* Zeitschrift fur Physik **51**, 165 (1928).

[57] B. W. Shore, M. V. Gromovyy, L. P. Yatsenko, and V. I. Romanenko. *Simple mechanical analogs of rapid adiabatic passage in atomic physics.* American Journal of Physics **77**, 1183 (2009).

[58] M. P. Fewell, B. W. Shore, and K. Bergmann. *Coherent population transfer among three states: Full algebraic solutions and the relevance of non adiabatic processes to transfer by delayed pulses.* Australian Journal of Physics **50**, 281 (1997).

[59] N. V. Vitanov, T. Halfmann, B. W. Shore, and K. Bergmann. *Laser-induced population transfer by adiabatic passage techniques.* Annual Review of Physical Chemistry **52**, 763 (2001).

[60] P. Dittmann, F. P. Pesl, J. Martin, G. W. Coulston, G. Z. He, and K. Bergmann. *The effect of vibrational excitation (3≤ v"≤ 19) on the reaction Na2 (v')+Cl NaCl+Na*.* The Journal of Chemical Physics **97**, 9472 (1992).

[61] H. Theuer and K. Bergmann. *Atomic beam deflection by coherent momentum transfer and the dependence on weak magnetic fields.* The European Physical Journal D - Atomic, Molecular and Optical Physics **2**, 279 (1998).

[62] S. Kulin, B. Saubamea, E. Peik, J. Lawall, T. W. Hijmans, M. Leduc, and C. Cohen-Tannoudji. *Coherent manipulation of atomic wave packets by adiabatic transfer.* Physical Review Letters **78**, 4185 (1997).

[63] A. S. Parkins and H. J. Kimble. *Quantum state transfer between motion and light.* Journal of Optics B: Quantum and Semiclassical Optics **1**, 496 (1999).

[64] J. Mompart, V. Ahufinger, and G. Birkl. *Coherent patterning of matter waves with subwavelength localization.* Physical Review A **79**, 053638 (2009).

[65] D. Viscor, J. L. Rubio, G. Birkl, J. Mompart, and V. Ahufinger. *Single-site addressing of ultracold atoms beyond the diffraction limit via position-dependent adiabatic passage.* Physical Review A **86**, 063409 (2012).

[66] J. L. Rubio, D. Viscor, V. Ahufinger, and J. Mompart. *Nanoscale resolution for fluorescence microscopy via adiabatic passage.* Optics Express **21**, 22139 (2013).

[67] R. Inoue, N. Kanai, T. Yonehara, Y. Miyamoto, M. Koashi, and M. Kozuma. *Entanglement of orbital angular momentum states between an ensemble of cold atoms and a photon.* Physical Review A **74**, 053809 (2006).

[68] I. I. Rabi, N. F. Ramsey, and J. Schwinger. *Use of rotating coordinates in magnetic resonance problems.* Reviews of Modern Physics **26**, 167 (1954).

[69] T. Morgan, B. O Sullivan, and T. Busch. *Coherent adiabatic transport of atoms in radio-frequency traps.* Physical Review A **83**, 053620 (2011).

[70] A. D. Greentree, J. H. Cole, A. R. Hamilton, and L. C. L. Hollenberg. *Coherent electronic transfer in quantum dot systems using adiabatic passage.* Physical Review B **70**, 235317 (2004).

[71] S. McEndoo, S. Croke, J. Brophy, and T. Busch. *Phase evolution in spatial dark states.* Physical Review A **81**, 043640 (2010).

[72] E. M. Graefe, H. J. Korsch, and D. Witthaut. *Mean-field dynamics of a Bose-Einstein condensate in a time-dependent triple-well trap: Nonlinear eigenstates, Landau-Zener models, and stimulated raman adiabatic passage.* Physical Review A **73**, 013617 (2006).

[73] M. Rab, J. H. Cole, N. G. Parker, A. D. Greentree, L. C. L. Hollenberg, and A. M. Martin. *Spatial coherent transport of interacting dilute Bose gases.* Physical Review A **77**, 061602 (2008).

[74] J. H. Cole, A. D. Greentree, L. C. L. Hollenberg, and S. Das Sarma. *Spatial adiabatic passage in a realistic triple well structure.* Physical Review B **77**, 235418 (2008).

[75] C. Ottaviani, V. Ahufinger, R. Corbalán, and J. Mompart. *Adiabatic splitting, transport, and self-trapping of a Bose–Einstein condensate in a double-well potential.* Physical Review A **81**, 043621 (2010).

[76] M. Rab, A. L. C. Hayward, J. H. Cole, A. D. Greentree, and A. M. Martin. *Interferometry using adiabatic passage in dilute-gas Bose-Einstein condensates.* Physical Review A **86**, 063605 (2012).

[77] L. P. Pitaevskii and S. Stringari. *Bose-Einstein Condensation* (Oxford University Press, Oxford, 2003).

[78] Y. Loiko, V. Ahufinger, R. Corbalán, G. Birkl, and J. Mompart. *Filtering of matter-wave vibrational states via spatial adiabatic passage.* Physical Review A **83**, 033629 (2011).

[79] A. Benseny, J. Bagudà, X. Oriols, and J. Mompart. *Need for relativistic corrections in the analysis of spatial adiabatic passage of matter waves.* Physical Review A **85**, 053619 (2012).

[80] B. O Sullivan, P. Morrissey, T. Morgan, and T. Busch. *Using adiabatic coupling techniques in atom-chip waveguide structures.* Physica Scripta **2010**, 014029 (2010).

[81] C.-L. Chen. *Foundations for guided-wave optics* (Wiley Interscience, Hoboken, 2007).

[82] R. Menchon-Enrich, A. Llobera, V. Cadarso, J. Mompart, and V. Ahufinger. *Adiabatic passage of light in CMOS-compatible silicon oxide integrated rib waveguides.* IEEE Photonics Technology Letters **24**, 536 (2012).

[83] R. Menchon-Enrich, A. Llobera, J. Vila-Planas, V. J. Cadarso, J. Mompart, and V. Ahufinger. *Light spectral filtering based on spatial adiabatic passage.* Light: Science & Applications **2**, e90 (2013).

[84] M. Thompson, A. Politi, J. Matthews, and J. O Brien. *Integrated waveguide circuits for optical quantum computing.* IET Circuits, Devices & Systems **5**, 94 (2011).

[85] R. Baets, P. Dumon, W. Bogaerts, G. Roelkens, J. Van Campenhout, D. Taillaert, J. Brouckaert, K. De Vos, J. Roels, S. K. Selvaraja, F. Van Laere, P. Bienstman, and D. Van Thourhout. *Silicon photonics.* International Symposium on VLSI Technology, Systems and Applications, 23 April-25 April 1 3 (2007).

[86] W. Bogaerts, R. Baets, P. Dumon, V. Wiaux, S. Beckx, D. Taillaert, B. Luyssaert, J. Van Campenhout, P. Bienstman, and D. Van Thourhout. *Nanophotonic waveguides in silicon-on-insulator fabricated with CMOS technology.* Journal of Lightwave Technology **23**, 401 (2005).

[87] A. Llobera, I. Salinas, I. Garcés, A. Merlos, and C. Domínguez. *Effect of wall tilt on the optical properties of integrated directional couplers.* Optics Letters **27**, 601 (2002).

[88] C. A. Barrios, B. Sánchez, K. B. Gylfason, A. Griol, H. Sohlstrom, M. Holgado, and R. Casquel. *Demonstration of slot-waveguide structures on silicon nitride / silicon oxide platform.* Optics Express **15**, 6846 (2007).

[89] P. Sahu. *A tapered structure for compact multimode interference coupler.* IEEE Photonics Technology Letters **20**, 638 (2008).

[90] D. Miller. *Device requirements for optical interconnects to silicon chips.* Proceedings of the IEEE **97**, 1166 (2009).

[91] W. Yang, D. B. Conkey, B. Wu, D. Yin, A. R. Hawkins, and H. Schmidt. *Atomic spectroscopy on a chip.* Nature Photonics **1**, 331 (2007).

[92] K. De Vos, I. Bartolozzi, E. Schacht, P. Bienstman, and R. Baets. *Silicon-on-insulator microring resonator forsensitive and label-free biosensing.* Optics Express **15**, 7610 (2007).

[93] F. Prieto, B. Sepúlveda, A. Calle, A. Llobera, C. Domínguez, A. Abad, A. Montoya, and L. M. Lechuga. *An integrated optical interferometric nanodevice based on silicon technology for biosensor applications.* Nanotechnology **14**, 907 (2003).

[94] W. Bogaerts, P. Dumon, D. Van Thourhout, D. Taillaert, P. Jaenen, J. Wouters, S. Beckx, V. Wiaux, and R. Baets. *Compact wavelength-selective functions in silicon-on-insulator photonic wires.* IEEE Journal of Selected Topics in Quantum Electronics **12**, 1394 (2006).

[95] J. Brouckaert, W. Bogaerts, P. Dumon, D. Van Thourhout, and R. Baets. *Planar concave grating demultiplexer fabricated on a nanophotonic silicon-on-insulator platform.* Journal of Lightwave Technology **25**, 1269 (2007).

[96] W. Bogaerts, S. Selvaraja, P. Dumon, J. Brouckaert, K. De Vos, D. Van Thourhout, and R. Baets. *Silicon-on-insulator spectral filters fabricated with CMOS technology.* IEEE Journal of Selected Topics in Quantum Electronics **16**, 33 (2010).

[97] A. Llobera, S. Demming, H. N. Joensson, J. Vila-Planas, H. Andersson-Svahn, and S. Buttgenbach. *Monolithic PDMS passband filters for fluorescence detection.* Lab on a Chip **10**, 1987 (2010).

[98] M. L. Chabinyc, D. T. Chiu, J. C. McDonald, A. D. Stroock, J. F. Christian, A. M. Karger, and G. M. Whitesides. *An integrated fluorescence detection system in poly(dimethylsiloxane) for microfluidic applications.* Analytical Chemistry **73**, 4491 (2001).

[99] A. H. Mahan, R. Biswas, L. M. Gedvilas, D. L. Williamson, and B. C. Pan. *On the influence of short and medium range order on the material band gap in hydrogenated amorphous silicon.* Journal of Applied Physics **96**, 3818 (2004).

[100] K. Okamoto. *Fundamentals of Optical Waveguides* (Elsevier, Burlingtong, 2006), 2nd edition.

[101] X. Sun, H.-C. Liu, and A. Yariv. *Adiabaticity criterion and the shortest adiabatic mode transformer in a coupled-waveguide system.* Optics Letters **34**, 280 (2009).

[102] M. Galarza, D. Van Thourhout, R. Baets, and M. Lopez-Amo. *Compact and highly-efficient polarization independent vertical resonant couplers for active-passive monolithic integration.* Optics Express **16**, 8350 (2008).

[103] C. Domínguez, J. A. Rodríguez, M. Riera, A. Llobera, and B. Díaz. *Effect of hydrogen-related impurities on the thermal behavior of mechanical stress in silicon oxides suitable for integrated optics.* Journal of Applied Physics **93**, 5125 (2003).

[104] L. Allen and J. H. Eberly. *Optical Resonance and Two-level Atoms* (Dover Publications, New York, 1987).

[105] B. W. Shore. *The theory of coherent atomic excitation, vol. 2* (Wiley Interscience, New York, 1990).

[106] Y. Loiko, V. Ahufinger, R. Menchon-Enrich, G. Birkl, and J. Mompart. *Coherent injection, extraction, and velocity filtration of neutral atoms in a ring trap via spatial adiabatic passage.* Submitted to Physical Review A .

[107] R. Menchon-Enrich, S. McEndoo, J. Mompart, V. Ahufinger, and T. Busch. *Tunneling induced angular momentum for single cold atoms.* Submitted to Physical Review A .

[108] F. Dreisow, M. Ornigotti, A. Szameit, M. Heinrich, R. Keil, S. Nolte, A. Tunnermann, and S. Longhi. *Polychromatic beam splitting by fractional stimulated Raman adiabatic passage.* Applied Physics Letters **95**, 261102 (2009).

[109] R. D. Meade, K. D. Brommer, A. M. Rappe, and J. D. Joannopoulos. *Photonic bound states in periodic dielectric materials.* Physical Review B **44**, 13772 (1991).

[110] R. D. Meade, A. Devenyi, J. D. Joannopoulos, O. L. Alerhand, D. A. Smith, and K. Kash. *Novel applications of photonic band gap materials: Low-loss bends and high Q cavities.* Journal of Applied Physics **75**, 4753 (1994).

[111] A. Mekis, J. C. Chen, I. Kurland, S. Fan, P. R. Villeneuve, and J. D. Joannopoulos. *High transmission through sharp bends in photonic crystal waveguides.* Physical Review Letters **77**, 3787 (1996).

[112] J. D. Joannopoulos, P. R. Villeneuve, and S. Fan. *Photonic crystals: Putting a new twist on light.* Nature **386**, 143 (1997).

[113] M. Sigalas and E. Economou. *Band structure of elastic waves in two dimensional systems.* Solid State Communications **86**, 141 (1993).

[114] M. S. Kushwaha, P. Halevi, L. Dobrzynski, and B. Djafari-Rouhani. *Acoustic band structure of periodic elastic composites.* Physical Review Letters **71**, 2022 (1993).

[115] M. S. Kushwaha, P. Halevi, G. Martínez, L. Dobrzynski, and B. Djafari-Rouhani. *Theory of acoustic band structure of periodic elastic composites.* Physical Review B **49**, 2313 (1994).

[116] F. R. Montero de Espinosa, E. Jiménez, and M. Torres. *Ultrasonic band gap in a periodic two-dimensional composite.* Physical Review Letters **80**, 1208 (1998).

[117] J. O. Vasseur, P. A. Deymier, B. Chenni, B. Djafari-Rouhani, L. Dobrzynski, and D. Prevost. *Experimental and theoretical evidence for the existence of absolute acoustic band gaps in two-dimensional solid phononic crystals.* Physical Review Letters **86**, 3012 (2001).

[118] X. Zhang and Z. Liu. *Negative refraction of acoustic waves in two-dimensional phononic crystals.* Applied Physics Letters **85**, 341 (2004).

[119] S. Yang, J. H. Page, Z. Liu, M. L. Cowan, C. T. Chan, and P. Sheng. *Focusing of sound in a 3D phononic crystal.* Physical Review Letters **93**, 024301 (2004).

[120] I. Pérez-Arjona, V. J. Sánchez-Morcillo, J. Redondo, V. Espinosa, and K. Staliunas. *Theoretical prediction of the nondiffractive propagation of sonic waves through periodic acoustic media.* Physical Review B **75**, 014304 (2007).

[121] V. Romero-García, R. Picó, A. Cebrecos, K. Staliunas, and V. J. Sánchez-Morcillo. *Angular band gaps in sonic crystals: Evanescent waves and spatial complex dispersion relation.* Journal of Vibration and Acoustics **135**, 041012 (2013).

[122] M. Kafesaki, M. M. Sigalas, and N. García. *Frequency modulation in the transmittivity of wave guides in elastic-wave band-gap materials.* Physical Review Letters **85**, 4044 (2000).

[123] A. Khelif, B. Djafari-Rouhani, J. O. Vasseur, P. A. Deymier, P. Lambin, and L. Dobrzynski. *Transmittivity through straight and stublike waveguides in a two-dimensional phononic crystal.* Physical Review B **65**, 174308 (2002).

[124] A. Khelif, B. Djafari-Rouhani, J. O. Vasseur, and P. A. Deymier. *Transmission and dispersion relations of perfect and defect-containing waveguide structures in phononic band gap materials.* Physical Review B **68**, 024302 (2003).

[125] T. Miyashita. *Full band gaps of sonic crystals made of acrylic cylinders in air —Numerical and experimental investigations—.* Japanese Journal of Applied Physics **41**, 3170 (2002).

[126] A. Khelif, A. Choujaa, B. Djafari-Rouhani, M. Wilm, S. Ballandras, and V. Laude. *Trapping and guiding of acoustic waves by defect modes in a full-band-gap ultrasonic crystal.* Physical Review B **68**, 214301 (2003).

[127] A. Khelif, A. Choujaa, S. Benchabane, B. Djafari-Rouhani, and V. Laude. *Guiding and bending of acoustic waves in highly confined phononic crystal waveguides.* Applied Physics Letters **84**, 4400 (2004).

[128] J. O. Vasseur, P. A. Deymier, B. Djafari-Rouhani, Y. Pennec, and A.-C. Hladky-Hennion. *Absolute forbidden bands and waveguiding in two-dimensional phononic crystal plates.* Physical Review B **77**, 085415 (2008).

[129] J.-H. Sun and T.-T. Wu. *Analyses of mode coupling in joined parallel phononic crystal waveguides.* Physical Review B **71**, 174303 (2005).

[130] F. S.-S. Chien, J. B. Tu, W.-F. Hsieh, and S.-C. Cheng. *Tight-binding theory for coupled photonic crystal waveguides.* Physical Review B **75**, 125113 (2007).

[131] M. Lewenstein, A. Sanpera, V. Ahufinger, B. Damski, A. Sen De, and U. Sen. *Ultracold atomic gases in optical lattices: Mimicking condensed matter physics and beyond.* Advances in Physics **56**, 243 (2007).

[132] J. Sabbatini, W. H. Zurek, and M. J. Davis. *Phase separation and pattern formation in a binary Bose-Einstein condensate.* Physical Review Letters **107**, 230402 (2011).

[133] Y. Japha, O. Arzouan, Y. Avishai, and R. Folman. *Using time-reversal symmetry for sensitive incoherent matter-wave Sagnac interferometry.* Physical Review Letters **99**, 060402 (2007).

[134] L. Plaja and J. San Román. *Dynamics of the formation of bright solitary waves of Bose-Einstein condensates in optical lattices.* Physical Review A **69**, 063612 (2004).

[135] L. Amico, A. Osterloh, and F. Cataliotti. *Quantum many particle systems in ring-shaped optical lattices.* Physical Review Letters **95**, 063201 (2005).

[136] A. M. Rey, K. Burnett, I. I. Satija, and C. W. Clark. *Entanglement and the Mott transition in a rotating bosonic ring lattice.* Physical Review A **75**, 063616 (2007).

[137] T. Wang, J. Javanainen, and S. F. Yelin. *Supercurrents in an atom-molecule gas in an optical ring lattice.* Physical Review A **76**, 011601 (2007).

[138] J. Javanainen, S. M. Paik, and S. M. Yoo. *Persistent currents in a toroidal trap.* Physical Review A **58**, 580 (1998).

[139] L. Salasnich, A. Parola, and L. Reatto. *Bosons in a toroidal trap: Ground state and vortices.* Physical Review A **59**, 2990 (1999).

[140] M. F. Andersen, C. Ryu, P. Cladé, V. Natarajan, A. Vaziri, K. Helmerson, and W. D. Phillips. *Quantized rotation of atoms from photons with orbital angular momentum.* Physical Review Letters **97**, 170406 (2006).

[141] A. Ramanathan, K. C. Wright, S. R. Muniz, M. Zelan, W. T. Hill, C. J. Lobb, K. Helmerson, W. D. Phillips, and G. K. Campbell. *Superflow in a toroidal Bose-Einstein condensate: An atom circuit with a tunable weak link.* Physical Review Letters **106**, 130401 (2011).

[142] M. Cozzini, B. Jackson, and S. Stringari. *Vortex signatures in annular Bose-Einstein condensates.* Physical Review A **73**, 013603 (2006).

[143] L. G. Marcassa, A. R. L. Caires, V. A. Nascimento, O. Dulieu, J. Weiner, and V. S. Bagnato. *Storage ring to investigate cold unidimensional atomic collisions.* Physical Review A **72**, 060701 (2005).

[144] A. Klein and D. Jaksch. *Phonon-induced artificial magnetic fields in optical lattices.* Europhysics Letters **85**, 13001 (2009).

[145] P. Ohberg. *The atomic quantum ring.* Journal of Optics **13**, 064024 (2011).

[146] G. Birkl, F. Buchkremer, R. Dumke, and W. Ertmer. *Atom optics with micro-fabricated optical elements.* Optics Communications **191**, 67 (2001).

[147] T. Muther, J. Nes, A.-L. Gehrmann, M. Volk, W. Ertmer, G. Birkl, M. Gruber, and J. Jahns. *Atomic quantum systems in optical micro-structures.* Journal of Physics: Conference Series **19**, 97 (2005).

[148] C. Ryu, M. F. Andersen, P. Cladé, V. Natarajan, K. Helmerson, and W. D. Phillips. *Observation of persistent flow of a Bose-Einstein condensate in a toroidal trap.* Physical Review Letters **99**, 260401 (2007).

[149] E. M. Wright, J. Arlt, and K. Dholakia. *Toroidal optical dipole traps for atomic Bose-Einstein condensates using Laguerre-Gaussian beams.* Physical Review A **63**, 013608 (2000).

[150] S. Franke-Arnold, J. Leach, M. J. Padgett, V. E. Lembessis, D. Ellinas, A. J. Wright, J. M. Girkin, P. Ohberg, and A. S. Arnold. *Optical ferris wheel for ultracold atoms.* Optics Express **15**, 8619 (2007).

[151] S. K. Schnelle, E. D. van Ooijen, M. J. Davis, N. R. Heckenberg, and H. Rubinsztein-Dunlop. *Versatile two-dimensional potentials for ultra-cold atoms.* Optics Express **16**, 1405 (2008).

[152] T. Lauber, J. Kuber, F. Schmaltz, J. Mompart, and G. Birkl. Submitted for publication .

[153] H. Kreutzmann, U. V. Poulsen, M. Lewenstein, R. Dumke, W. Ertmer, G. Birkl, and A. Sanpera. *Coherence properties of guided-atom interferometers.* Physical Review Letters **92**, 163201 (2004).

[154] T. Holstein. *Mobilities of positive ions in their parent gases.* The Journal of Physical Chemistry **56**, 832 (1952).

[155] C. Herring. *Critique of the Heitler-London method of calculating spin couplings at large distances.* Reviews of Modern Physics **34**, 631 (1962).

[156] A. D. Cronin, J. Schmiedmayer, and D. E. Pritchard. *Optics and interferometry with atoms and molecules.* Reviews of Modern Physics **81**, 1051 (2009).

[157] R. Bouchendira, P. Cladé, S. Guellati-Khélifa, F. Nez, and F. Biraben. *New determination of the fine structure constant and test of the quantum electrodynamics.* Physical Review Letters **106**, 080801 (2011).

[158] R. Geiger, V. Ménoret, G. Stern, N. Zahzam, P. Cheinet, B. Battelier, A. Villing, F. Moron, M. Lours, Y. Bidel, A. Bresson, A. Landragin, and P. Bouyer. *Detecting inertial effects with airborne matter-wave interferometry.* Nature Communications **2**, 474 (2011).

[159] J. K. Stockton, K. Takase, and M. A. Kasevich. *Absolute geodetic rotation measurement using atom interferometry.* Physical Review Letters **107**, 133001 (2011).

[160] S. Dimopoulos, P. W. Graham, J. M. Hogan, and M. A. Kasevich. *Testing general relativity with atom interferometry.* Physical Review Letters **98**, 111102 (2007).

[161] M. A. Hohensee, S. Chu, A. Peters, and H. Muller. *Equivalence principle and gravitational redshift.* Physical Review Letters **106**, 151102 (2011).

[162] S. Dimopoulos, P. W. Graham, J. M. Hogan, M. A. Kasevich, and S. Rajendran. *Atomic gravitational wave interferometric sensor.* Physical Review D **78**, 122002 (2008).

[163] P. W. Graham, J. M. Hogan, M. A. Kasevich, and S. Rajendran. *New method for gravitational wave detection with atomic sensors.* Physical Review Letters **110**, 171102 (2013).

[164] C. E. Wieman, D. E. Pritchard, and D. J. Wineland. *Atom cooling, trapping, and quantum manipulation.* Reviews of Modern Physics **71**, S253 (1999).

[165] F. Schmidt-Kaler, T. Pfau, P. Schmelcher, and W. Schleich. *Focus on atom optics and its applications.* New Journal of Physics **12**, 065014 (2010).

[166] M. Lewenstein, A. Sanpera, and V. Ahufinger. *Ultracold atoms in optical lattices: Simulating quantum many-body systems* (Oxford University Press, Oxford, 2012).

[167] J. R. Abo-Shaeer, C. Raman, J. M. Vogels, and W. Ketterle. *Observation of vortex lattices in Bose-Einstein condensates.* Science **292**, 476 (2001).

[168] S. Thanvanthri, K. T. Kapale, and J. P. Dowling. *Ultra-stable matter–wave gyroscopy with counter-rotating vortex superpositions in Bose–Einstein condensates.* Journal of Modern Optics **59**, 1180 (2012).

[169] K. T. Kapale and J. P. Dowling. *Vortex phase qubit: Generating arbitrary, counterrotating, coherent superpositions in Bose-Einstein condensates via optical angular momentum beams.* Physical Review Letters **95**, 173601 (2005).

[170] S. Thanvanthri, K. T. Kapale, and J. P. Dowling. *Arbitrary coherent superpositions of quantized vortices in Bose-Einstein condensates via orbital angular momentum of light.* Physical Review A **77**, 053825 (2008).

[171] N. Lo Gullo, S. McEndoo, T. Busch, and M. Paternostro. *Vortex entanglement in Bose-Einstein condensates coupled to Laguerre-Gauss beams.* Physical Review A **81**, 053625 (2010).

[172] Y. Castin, Z. Hadzibabic, S. Stock, J. Dalibard, and S. Stringari. *Quantized vortices in the ideal bose gas: A physical realization of random polynomials.* Physical Review Letters **96**, 040405 (2006).

[173] B. Jackson, J. F. McCann, and C. S. Adams. *Vortex formation in dilute inhomogeneous Bose-Einstein condensates.* Physical Review Letters **80**, 3903 (1998).

[174] A. E. Leanhardt, A. Gorlitz, A. P. Chikkatur, D. Kielpinski, Y. Shin, D. E. Pritchard, and W. Ketterle. *Imprinting vortices in a Bose-Einstein condensate using topological phases.* Physical Review Letters **89**, 190403 (2002).

[175] L. Dobrek, M. Gajda, M. Lewenstein, K. Sengstock, G. Birkl, and W. Ertmer. *Optical generation of vortices in trapped Bose-Einstein condensates.* Physical Review A **60**, R3381 (1999).

[176] K.-P. Marzlin, W. Zhang, and E. M. Wright. *Vortex coupler for atomic Bose-Einstein condensates.* Physical Review Letters **79**, 4728 (1997).

[177] G. Nandi, R. Walser, and W. P. Schleich. *Vortex creation in a trapped Bose-Einstein condensate by stimulated Raman adiabatic passage.* Physical Review A **69**, 063606 (2004).

[178] A. Muthukrishnan and C. R. Stroud Jr. *Entanglement of internal and external angular momenta of a single atom.* Journal of Optics B: Quantum and Semiclassical Optics **4**, S73 (2002).

[179] J. E. Williams and M. J. Holland. *Preparing topological states of a Bose–Einstein condensate.* Nature **401**, 568 (1999).

[180] K. W. Madison, F. Chevy, W. Wohlleben, and J. Dalibard. *Vortex formation in a stirred Bose-Einstein condensate.* Physical Review Letters **84**, 806 (2000).

[181] P. C. Haljan, I. Coddington, P. Engels, and E. A. Cornell. *Driving Bose-Einstein-condensate vorticity with a rotating normal cloud.* Physical Review Letters **87**, 210403 (2001).

[182] S. Inouye, S. Gupta, T. Rosenband, A. P. Chikkatur, A. Gorlitz, T. L. Gustavson, A. E. Leanhardt, D. E. Pritchard, and W. Ketterle. *Observation of vortex phase singularities in Bose-Einstein condensates.* Physical Review Letters **87**, 080402 (2001).

[183] B. P. Anderson, P. C. Haljan, C. A. Regal, D. L. Feder, L. A. Collins, C. W. Clark, and E. A. Cornell. *Watching dark solitons decay into vortex rings in a Bose-Einstein condensate.* Physical Review Letters **86**, 2926 (2001).

[184] D. R. Scherer, C. N. Weiler, T. W. Neely, and B. P. Anderson. *Vortex formation by merging of multiple trapped Bose-Einstein condensates.* Physical Review Letters **98**, 110402 (2007).

[185] L. N. Trefethen and D. Bau. *Numerical linear algebra* (Society for Industrial and Applied Mathematics, Philadelphia, 1997).